SIMULATION STUDY OF INVISIBLE DECAYS OF THE HIGGS BOSON WITH THE CIRCULAR ELECTRON POSITRON COLLIDER

by

Susmita Jyotishmati

APPROVED BY SUPERVISORY COMMITTEE:

XinChou Lou, Chair

Robert Glosser

Mustapha Ishak-Boushaki

Lindsay J. King

Kendall Reeves

To my

husband and sons

SIMULATION STUDY OF INVISIBLE DECAYS OF THE HIGGS BOSON WITH THE CIRCULAR ELECTRON POSITRON COLLIDER

by

SUSMITA JYOTISHMATI, MS

DISSERTATION

Presented to the Faculty of

The University of Texas at Dallas

in Partial Fulfillment

of the Requirements

for the Degree of

DOCTOR OF PHILOSOPHY IN

PHYSICS

THE UNIVERSITY OF TEXAS AT DALLAS

May 2017

ACKNOWLEDGMENTS

The journey towards the completion of this dissertation has been an intense learning period. I extend my sincerest thanks to my advisor Dr. XinChou Lou for his guidance, support, patience and trust. I thank him for having confidence in my ability even when I may have doubted it.

I thank Dr. Xin Mo for being the constant pillar of support for my research and travelling to UTD to solidify my dissertation.

I extend my gratitude to my committee members for their kind words of advise, time and warmth. I am lucky to have them as my committee.

A special thanks is extended to Dr. Gang Li for his suggestions and Matthew Kurth for discussions on the CEPC detector.

I express my gratitude to Dr. Joseph Izen, his research group (at UTD and CERN) and IHEP (at Beijing) research group for their time and grilling questions that helped me grow my knowledge.

I thank Dr. Vindhyawasini Prasad for his help during my early years of research.

I am indebted to my parents for instilling in me a love of learning.

Finally, I thank my husband, Himanshu Dutta and my sons, Mayank Dutta and Vedant Dutta for their encouragement and understanding.

March 2017

SIMULATION STUDY OF INVISIBLE DECAYS OF THE HIGGS BOSON WITH THE CIRCULAR ELECTRON POSITRON COLLIDER

Susmita Jyotishmati, PhD
The University of Texas at Dallas, 2017

Supervising Professor: XinChou Lou, Chair

A Higgs-like boson has been discovered by the experiments ATLAS and CMS at the LHC. We need to verify that it is the Standard Model (SM) Higgs and understand its nature. A Circular Electron Positron Collider (CEPC), has been proposed as a Higgs factory for detailed study of the Higgs boson. In this dissertation we study the feasibility of measuring the $H \to Invisible$ decays at the CEPC. Dark Matter (DM) interacts with matter by gravity, thus appears to be invisible in the CEPC experiment. If Higgs boson couples to DM it could be an important "portal" to New Physics. A Monte Carlo analysis of $H \to Invisible$ optimized to achieve high signal significance, and low backgrounds in the $e^+e^- \to ZH$, $Z \to \mu^+\mu^-$ channel based on an integrated luminosity of 5 ab^{-1} expected for ten years run of the CEPC, is performed. Precision on the Higgs to invisible branching ratio at the input values of 0.1%(SM) and Beyond Standard Model (BSM) cases 0%, 1%, 5% and 10% is determined. Two approaches have been employed. They are the cut-based analysis and the multivariate analysis. Based on this dissertation study a baseline analysis approach is recommended for future CEPC design and studies.

TABLE OF CONTENTS

LIST OF FIGURES

LIST OF TABLES

CHAPTER 1

INTRODUCTION

1.1 INTRODUCTION

In this opening chapter, a brief description of elementary particle physics is followed by the theoretical framework for Higgs mechanism. The properties of the Higgs boson is described. A small section is dedicated to BSM at the end.

1.2 STANDARD MODEL OF ELEMENTARY PARTICLE PHYSICS

In today's Standard Model (SM), the elementary quantum mechanical (QM) fields and their quanta (discreet indivisible units of energy that QM implies for waves and fields), which are the elementary particles, the relationships between them and their properties like having energy, momentum, spin (fermion or boson) etc., are described to a remarkably good extent. Fermions are associated with matter particles; they obey Paulis exclusion principle as a consequence of which, no more than one fermion can be in the same quantum mechanical state [1]. Bosons are force carriers, they follow Bose-Einstein statistics, which does not restrict them from being in the same quantum mechanical state [1]. The gauge structure of SM arises from the symmetry group,

$$SU(3)_c \times SU(2)_L \times U(1)_Y \tag{1.1}$$

where, $U(1)_Y$ is the unitary group of electromagnetic theory (photons and leptons), subscript Y stands for hypercharge operator. $SU(3)_c$ is the special unitary groups of quantum chromodynamics (QCD), c stands for the color charge. $SU(2)_L$ is the special unitary group of electro-weak (EW) interactions, L stands for the left handed fermion the weak gauge bosons couple to. The symmetry of equations of motion can be generated from a Lagrangian. The Lagrangian is a tool for encoding the interaction between the particles. The various terms in the Lagrangian, for example products of fields, represent properties, here the vertices of process, where particles come in and other particles go out. Forces arise due to exchange of elementary particles. Any particle can be exchanged in some context or the other, and it produces force. In molecular physics, it is the exchange of protons and electrons. In electrodynamics, it is the exchange of photons and so on. Elementary particles, their field and the forces which are associated due to exchange processes with that particular kind of particles it can jump back and forth, have one to one correspondence. We have a triangle as shown in the Figure 1.1.

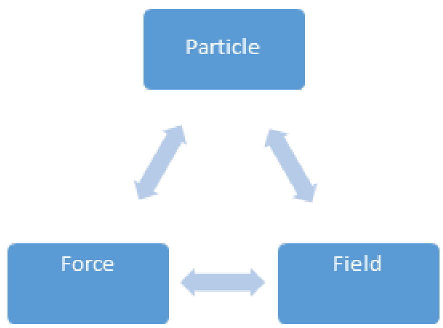

Figure 1.1. One to one correspondence between field, particle and force.

SM divides the particles, the players in the drama, into groups and they have name and personality. The list of elementary particles is summarized in Table 1.1. We however, don't understand why some particles exist and others don't. We only understand some relationships between particles. It is hypothesized that there is a possibility that if certain particles exist, there must be other particles as well, so as to maintain the symmetry of the physical world.

1.3 THE GAUGE THEORY AND SPONTANEOUS SYMMETRY BREAKING

According to quantum field theory, reality is a series of fields. The gauge theories describe all elementary particle interactions. There are three kinds of fields-scalar for spin 0, spinor

Table 1.1. Elementary particles of Standard Model.

Name	Symbol	Spin ($\hbar$)	Charge (e)	Baryon	Mass
		Boson			
Photon	γ	1	0	0	0
Gluon	g	1	0	0	0
Weak Gauge Bosons					
W^+	W^+	1	+1	0	80.4 GeV
W^-	W^-	1	-1	0	80.4 GeV
Z^0	Z^0	1	0	0	91.2 GeV
Higgs Boson	H	0	0	0	125.6 GeV
		Fermion			
		Lepton			
Electron	e^+	1/2	-1	0	0.511 MeV
Electron Neutrino	ν_e	1/2	0	0	0?
Muon	μ^-	1/2	-1	0	105.7 MeV
Muon Neutrino	ν_μ	1/2	0	0	0?
Tau	τ^-	1/2	-1	0	1.777 GeV
Tau Neutrino	ν_τ	1/2	0	0	0?
		Quark			
Down	d	1/2	-1/3	1/3	4.8 MeV
Up	u	1/2	2/3	1/3	2.4 MeV
Strange	s	1/2	-1/3	1/3	104 MeV
Charm	c	1/2	2/3	1/3	1.27 GeV
Bottom	b	1/2	-1/3	1/3	4.2 GeV
Top	t	1/2	2/3	1/3	171.2 GeV

for spin 1/2, and vector for spin 1 particles. The dynamics of the field is controlled by the Lagrangian [1]. In quantum field theory the Lagrangian is axiomatic and concocted in a way so as to arrive at the desired field equation through Euler- Lagrangian equations [1].

Symmetry operations are operations that we do that do not change the Lagrangian of the system, or the Lagrangian remains invariant.

Requiring the Dirac Lagrangian to be locally phase invariant or gauge invariant leads to the introduction of a vector field and it has to be massless [1]. This leads to the Lagrangian for the quantum electrodynamics, viz. the Dirac fields (leptons and quarks) interacting with Maxwell field (photon). This is the invariance of the U(1) group. The symmetry involved is called the U(1) gauge invariance. The strong interaction is described by the SU(3) group, and are mediated by gluons, there are eight of them and have color charge and interact with particles that carry color charge.

The coupling strength of the EM and weak forces both increase with energy. The Glashow-Salam-Weinberg model showed that at high enough energies, the EM and weak forces combine to yield the electroweak interactions described by the $SU(2) \times U(1)$ group. The requirement of guage invariance to this group yields four bosons called gauge Bosons. W^+, W^- and Z^0 arise from SU(2) group and they can interact with each other since SU(2) is non-abelian. The remaining gauge boson is the photon. With their respective forces combined, the discrepancy between the masses of the weak bosons and that of the photon remains and must be explained. Higgs et al. proposed a massive scalar boson identified with the field, which we call the Higgs boson, and hence the Higgs field. The Higgs mechanism allows for the symmetry of the massless bosons to be broken spontaneously through interaction with a complex scalar field [1, 2].

The Lagrangian with spontaneously broken continuous symmetry is constructed as,

$$L = \frac{1}{2}\partial^\mu \varphi_1 \partial_\mu \varphi_1 + \frac{1}{2}\partial^\mu \varphi_2 \partial_\mu \varphi_2 + \frac{1}{2}\mu^2[\varphi_1^2 + \varphi_2^2] - \frac{1}{4}\lambda^2[\varphi_1^2 + \varphi_2^2]^2 \tag{1.2}$$

φ_1 and φ_2 are the two fields and the Lagrangian is invariant under rotations in φ_1 , φ_2 space [1]. The potential energy is given by

$$U = -\frac{1}{2}\mu^2[\varphi_1^2 + \varphi_2^2] + \frac{1}{4}\lambda^2[\varphi_1^2 + \varphi_2^2]^2 \tag{1.3}$$

The minimum lies at the circle of radius $\frac{\mu}{\lambda}$. Figure 1.2 shows the Higgs potential as a function of field.

$$\varphi_{1min}^2 + \varphi_{2min}^2 = \frac{\mu^2}{\lambda^2} \tag{1.4}$$

We now choose a particular value of φ_{1min} and φ_{2min}.

$$\varphi_{1min} = \mu/\lambda, \varphi_{2min} = 0 \tag{1.5}$$

On introducing two new fields ζ and ρ , such that they represent fluctuations about the vacuum state.

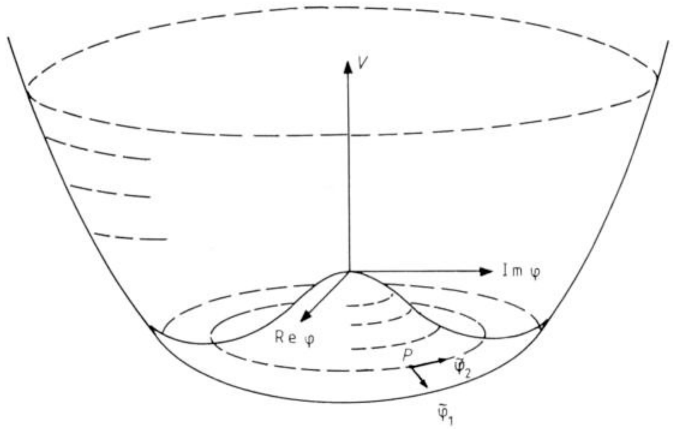

Figure 1.2. Higgs Potential.

$$\zeta = \varphi_1 - \frac{\mu}{\lambda}; \rho = \varphi_2 \tag{1.6}$$

The Lagrangian in terms of these two fields read,

$$[\frac{1}{2}\partial^\mu \zeta \partial_\mu \zeta - \mu^2 \zeta^2] + [\frac{1}{2}\partial^\mu \rho \partial_\mu \rho] - [\mu\lambda(\zeta^3 + \zeta\rho^2) + \frac{\lambda^2}{4}(\zeta^4 + \rho^4 + 2\zeta^2\rho^2)] + \frac{\mu^4}{4\lambda^2} \tag{1.7}$$

It is seen that ζ and ρ in fact are two real Klein-Gordon fields. Fields whose quanta are spin zero particles. By quantising these fields the Lagrangian describes two different spin 0 particle fields. The ζ bosons will have mass,

$$m_\zeta = \sqrt{2}\mu\hbar/c \tag{1.8}$$

which arises from the ζ^2 term while the ρ bosons will be massless.

$$m_\rho = 0 \tag{1.9}$$

The masslessness of the ρ bosons are a direct consequence of the minimum being degenerate. These are called the Goldstone Bosons and show up when the continuous global symmetry is spontaneously broken [1]. The remaining terms are the interactions among the ζ and ρ particles through perturbation theory also called the couplings [1]. It can be seen that the spontaneous symmetry breaking of the U(1) symmetry due to the degenerate energy minimum of the Lagrangian, gives rise to a pertubative theory with a massive scalar boson.

1.4 THE HIGGS BOSON

Higgs is a spin 0 scalar boson, a quanta of the Higgs field. The Higgs field is responsible for giving mass to the fundamental particles. In 1964, a mechanism for this process was proposed by three groups of researchers: Brout and Englert, Guralnik, Hagen and Kibble and Higgs [3, 4, 5, 6]. To create massive vector bosons in a gauge invariant theory, the spontaneous symmetry breaking is extended and is called the Higgs mechanism [1, 2]. Writing the Lagrangian in terms of a single complex scalar field,

$$\varphi = \varphi_1 + i\varphi_2 \text{ such that } \varphi^*\varphi = \varphi_1^2 + \varphi_2^2 \tag{1.10}$$

The Lagrangian reads,

$$L = \frac{1}{2}(\partial_\mu\varphi)^*(\partial^\mu\varphi) + \frac{1}{2}\mu^2\varphi^*\varphi - \frac{1}{4}\lambda^2(\varphi^*\varphi)^2 \tag{1.11}$$

When we apply local guage invariance and spontaneous symmetry breaking, namely by introducing covariant derivative

$$D_\mu = \partial_\mu + i\frac{q}{\hbar c}A_\mu \tag{1.12}$$

and the new fields,

$$\zeta = \varphi_1 - \frac{\mu}{\lambda}; \rho = \varphi_2 \tag{1.13}$$

we also select a convenient guage to obtain the Lagrangian which is,

$$\begin{aligned} L = {} & [\frac{1}{2}\partial^\mu\zeta\partial_\mu\zeta - \mu^2\zeta^2] + [-\frac{1}{16}F_{\mu\nu}F^{\mu\nu} + \frac{1}{2}(\frac{q}{\hbar c}\frac{\mu}{\lambda})^2\ A_\mu A^\mu] \\ & + \{\frac{\mu}{\lambda}(\frac{q}{\hbar c})^2\zeta A_\mu A^\mu + \frac{1}{2}(\frac{q}{\hbar c})^2\zeta^2 A_\mu A^\mu - \lambda\mu\zeta^3 - \frac{\lambda^2\eta^4}{4}\} + (\frac{\mu^2}{2\lambda})^2 \end{aligned} \tag{1.14}$$

By making a clever choice of gauge, the Goldstone Boson is eliminated and what is left is the massive scalar ζ, the Higgs particle and a massive gauge field A_μ .

A massless spin zero particle has two transverse polarized states while a massive spin zero particle has an additional longitudinal polarized state.

When the spontaneous symmetry breaking of the U(1) symmetry occurs, the complex scalar field (two degrees of freedom) and a massless vector field (two degrees of freedom), transform into one real scalar field (one degree of freedom) and a massive vector boson field (3 degrees of freedom) [1, 2]. Total degrees of freedom is four and is conserved during symmetry breaking.

When the spontaneous symmetry breaking of $SU(2) \times U(1)$ symmetry occurs a complex scalar doublet (four degrees of freedom) and four massless vector bosons (eight degrees of freedom) transform into one real scalar (one degree of freedom) , three massive vector (nine degrees of freedom) and one massless vector boson (two degrees of freedom). Total degrees of freedom is twelve and is conserved during symmetry breaking.

1.5 THE PRODUCTION AND DECAY OF THE HIGGS BOSON

In the search for the Standard Model (SM) Higgs boson at the Large Hadron Collider (LHC), the discovery of a narrow resonance, with a mass near 125.7 GeV, was announced at CERN by both the ATLAS and CMS experiments on July 4, 2012 [2]. "For the theoretical discovery of a mechanism that contributes to our understanding of the origin of mass of subatomic particles, and which recently was confirmed through the discovery of the predicted fundamental particle, by the ATLAS and CMS experiments at CERN's Large Hadron Collider, on 8th October, 2013 the Nobel Prize in Physics was awarded jointly to François Englert and Peter Higgs [6]." The most important processes for Higgs production at hadron colliders are the gluon fusion, vector boson fusion, associative production with the W, and an associative production with a top pair, as shown in the Figure 1.3 a, b, c and d, respectively [7].

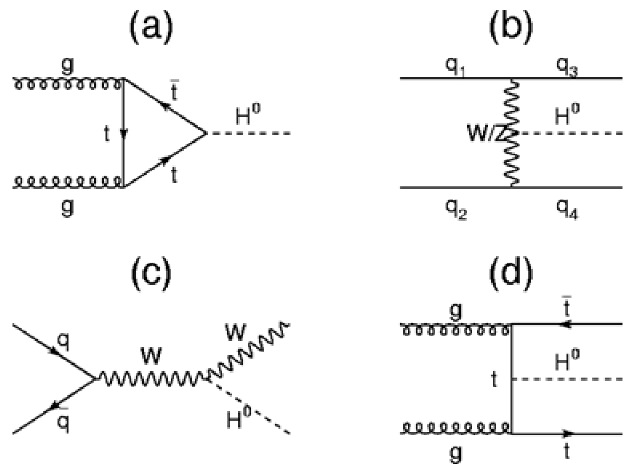

Figure 1.3. Feynman diagrams for the Higgs production mechanism [8].

Table 1.2 tabulates the production cross-section in pb (pico barn) for gluon fusion, vector boson fusion, associated production with a W or a Z boson and top pair in pp collision at 4.8 fb^{-1} with the ATLAS detector at $\sqrt{s}$= 7, 8 and 14 TeV. The dominating Higgs production mechanism is the gluon-gluon fusion process for all possible Higgs masses. However, at low energies (~250 GeV) electron positron collider associative production with Z is the most dominant Higgs production mechanism [7].

Table 1.2. Production cross-section in pb for gluon fusion, vector boson fusion, associated production with a W or a Z boson and top pair in pp collision at 4.8 fb^{-1} with the ATLAS detector at $\sqrt{s}$= 7, 8 and 14 TeV [8].

$\sqrt{s}$ (TeV)	ggF (pb)	VBF (pb)	VH (pb)	$t\bar{t}H$ (pb)
7	15.1	1.221	0.914	0.086
8	19.5	1.58	0.09	0.13
14	49.9	4.18	2.38	0.611

In the Figure 1.4 cross section is shown as a function of the Higgs mass. The Higgs boson couples to fermions and gauge bosons, or more precisely particle-antiparticle pair and also to massless gluons and photons. The branching ratio of the Higgs is shown in Figure 1.5. Table 1.3 shows the branching ratios for the Standard Model Higgs Boson decay modes for m_h=125 GeV at $\sqrt{s}$ =14 TeV at the ATLAS Detector. When Higgs decays to fermions, its

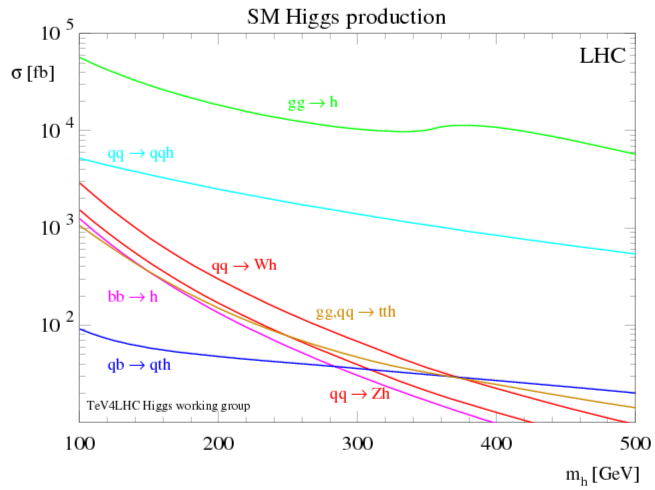

Figure 1.4. Total cross sections for Higgs production at the LHC [8].

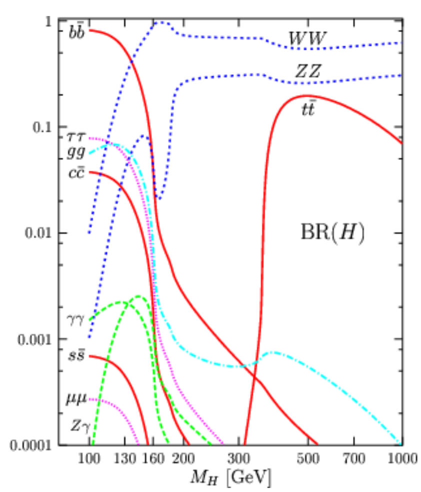

Figure 1.5. Branching ratio BR(H) of the Standard model Higgs Boson to different decay channels for different mass ranges [8].

Table 1.3. The branching ratios for the Standard Model Higgs Boson decay modes for m_h=125 GeV at $\sqrt{s}$ =14 TeV at the ATLAS Detector [8].

Process	Branching ratio	Uncertainty
$H \rightarrow b\bar{b}$	5.77 x 10^{-1}	+3.2% -3.3%
$H \rightarrow \tau\bar{\tau}$	6.32 x 10^{-2}	+5.7% -5.7%
$H \rightarrow \mu\bar{\mu}$	2.20 x 10^{-4}	+6.0% -5.9%
$H \rightarrow c\bar{c}$	2.91 x 10^{-2}	+12.2% -12.2%
$H \rightarrow gg$	8.57 x 10^{-2}	+10.2% -10.0%
$H \rightarrow \gamma\gamma$	2.28 x 10^{-3}	+5.0% -4.9%
$H \rightarrow Z\gamma$	1.54 x 10^{-3}	+9.0% -8.8%
$H \rightarrow WW$	2.15 x 10^{-1}	+4.3% -4.2%
$H \rightarrow ZZ$	2.64 x 10^{-2}	+4.3% -4.2%
$\Gamma H[GeV]$	4.07 x10^{-3}	+4.0% -3.9%

decay into heavier particles is more likely than decaying into lightweight particles. Higgs can have vector boson decay, fermionic decay, two photon decay, two gluon decay among others.

1.6 BEYOND THE STANDARD MODEL

There are new physics models that try to eliminate the deficiencies of SM, and they have new particles in them, the consequence of which is the deviation of the Higgs coupling from SM prediction. Some examples of the models are One Parameter Model, Two Higgs Doublet Model, Minimal Supersymmetric Model (MSSM), phenomenological version of MSSM called pMSSM, Composite Higgs Model and New Couplings arising from loops [9, 10, 11].

The unified description of interaction in nature is noted for being innovative and beautiful, but it also leads to concrete quantitative description of the relative strengths of these interaction [12]. In the traditional realm of HEP, the strong, weak and electromagnetic interactions are mediated by spin one gauge bosons. Georgi and Glashow have shown that the simplest of gauge group for grand unification is the SU(5) symmetry group, such that transformation between SU(3) and SU(2) is possible. The existence of gauge bosons corresponding to all possible changes and responses among all five dimensions are predicted, such that processes like, particle carrying color charge can couple to particle with weak isospin [12]. In such processes baryon number is not conserved. Process like the decay of the proton to pion and antilepton is possible by coupling through these supersymmetric particles. Minimal supersymmetry also predicts value for the coupling constants that unifies at energy of 10^{16} GeV. We know that the coupling constant is not a constant but varies with energy, this is called running of coupling constant. This is due to asymptotic freedom. Quarks hit at high energy behaves like point particle and emit fewer gluons while when hit softly behaves like a thick ball of virtual gluons, quark and anti-quark [12, 14]. So we see that as energy increases the coupling decreases. This is called the asymptotic freedom. It is the opposite of electromagnetic screening effect. In the SU(3) the coupling is more affected by asymptotic freedom as there are more gauge bosons than colors, (8 gluons compared to 3 colors) in SU(2) it is not so much as there a not as many gauge bosons [1], (3 weak gauge bosons compared to 2 weak isospin) while in U(1) the ordinary screening effect prevails. Figure 1.6 shows the running of the inverse coupling constant for strong, weak and electromagnetic interactions (red, green and blue lines) in minimal supersymmetric model and their unification at 10^{16} GeV. The SU(5) is a symmetry whose operation transforms particles with a spin to a particle of other spin which differs by $\hbar/2$. So it changes fermions to bosons and vice versa. This entails inclusion of a whole set of new particles called superpartners, which raises the scale of unification by partially cancelling the asymptotic freedom [12]. The minimal supersymmetric model predicts unification scale of the coupling strength at 10^{16} GeV and proton lifetime of about (10^{33}) years . Local guage invariance applied to supersymmetry leads to Einteins general relativity thus clarifying the hierarchy problem, that is, the vast difference between Plank mass scale 10^{19} GeV and electroweak mass scale (246 GeV) [12]. Another hierarchy problem is the mass of the superpartners of scalar field, that is, the Higgs field.

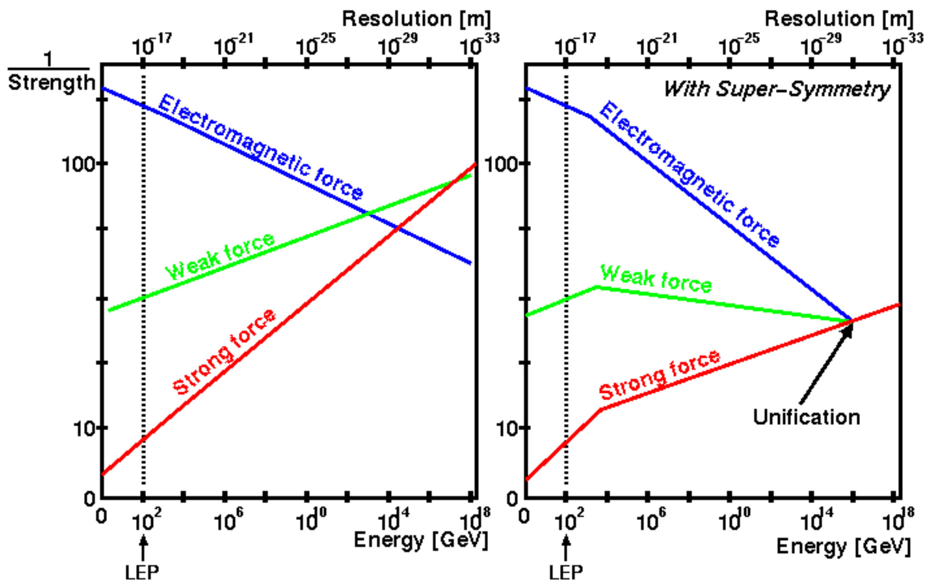

Figure 1.6. Running of the inverse coupling constant for strong, weak and electromagnetic interactions (red, green and blue lines) in minimal supersymmetric model and their unification at 10^{16} GeV [13].

The proton decay rate is inversely proportional to the product of the Higgs mass and its superpartner mass according to some BSM models. The mass of the Higgs field responsible for electroweak symmetry breaking is small, while if that of superpartner, the strong color Higgs [12, 14] is small as well, it would mean that the proton decay rate will increase catastrophically, so the superpartner of Higgs has to be massive. This means that the complete symmetry does not exist.

CHAPTER 2

RESEARCH TOPIC AND MOTIVATION

2.1 INTRODUCTION

This chapter states the topic and discusses the motivation for my research.

2.2 TOPIC OF RESEARCH

We set out to do a full Monte Carlo analysis to reconstruct and measure the SM Higgs to invisible decays, in the Higgs-strahlung process, $e^+e^- \to ZH$, with the CEPC detector in the $Z \to \mu^+\mu^-$ channel with an the integrated luminosity of 5 ab^{-1}. Figure 2.1 shows the event display for this process at the CEPC. The newly discovered Higgs boson is light and

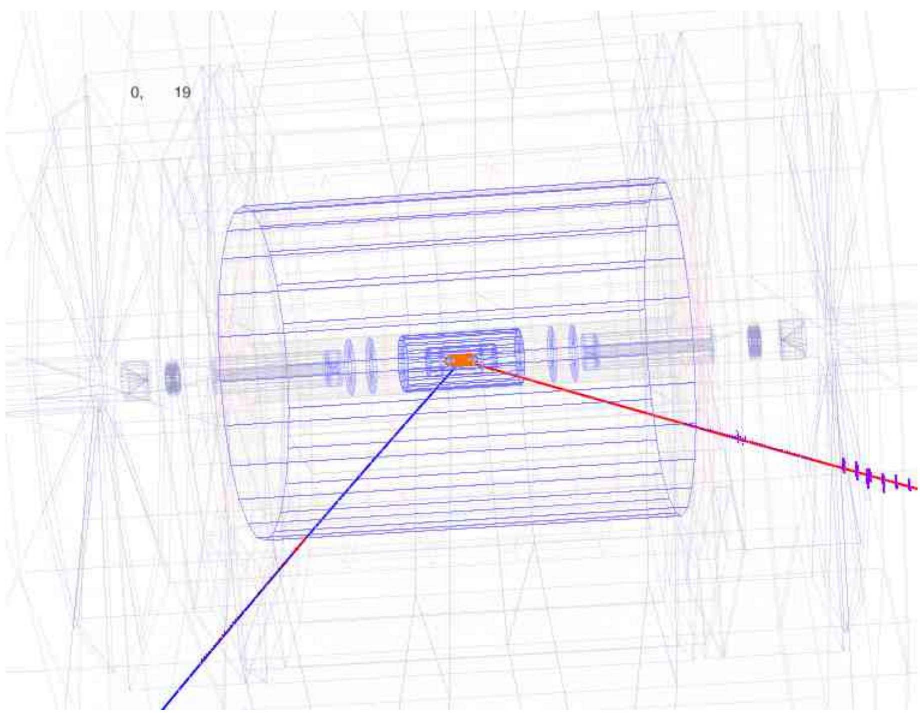

Figure 2.1. Event Display.

expected to have a narrow width of approximately 4 MeV. This implies that its branching fractions are highly receptive to any new particles, to which it has unsuppressed coupling.

Higgs mass is taken to be 125 GeV. Studies at LHC [15] have been performed, however with a very limited precision. Our aim is to update these studies and estimate the sensitivity of 250 GeV electron-positron collider experiment, CEPC, to an invisibly decaying Higgs.

My research is divided into two parts:

Part 1: To find out ways to increase efficiency and significance for the signal, Higgs to invisible with the CEPC in the SM and BSM cases. Which means, when its branching ratio is 0.1% (SM) or 0%, 1%, 5%, 10% (BSM).

Two approaches wil be adopted: (1) Cut based analysis where effective cuts on the kinematic variables for better background rejection, while retaining the efficiency for the signal. (2) Multivariate analysis: BDT.

Part 2: To measure the erros on the Higgs to invisible branching ratio. Determine the upper limit on the branching ratio for the SM case.

2.3 MOTIVATION

An electron-positron collider operating in the center-of-mass energy of 250 GeV is a very suitable experiment for the precision study of the Higgs boson. Higgs boson will be copiously produced by this collider in the process called Higgs-strahlung, $e^+e^- \to ZH$. Figure 2.2 shows the Feynman diagram of the Higgs-strahlung process.

Compared to LHC that has much more QCD background, CEPC will provide a much cleaner environment for analysis.

Invisible particles such as dark matter that may be invisible Higgs decay modes are predicted by physics models that rectify the inabilities of the SM to explain the electroweak symmetry breaking. There is strong motivation to study full models which demonstrate a corresponding coupling pattern if notable deviations in any Higgs coupling scale factors is detected.

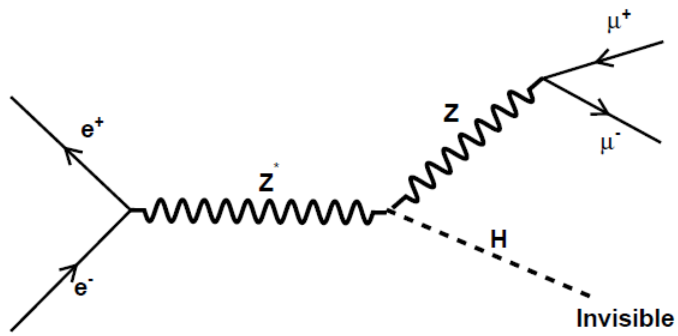

Figure 2.2. Feynman diagram contributing to the Higgs-strahlung process.

In their work, “Motivation and detectability of an invisibly-decaying Higgs boson at the Fermilab Tevatron”, Stephen P. Martinand and James D. Wells have itemized various scenarios in which Higgs will have invisible decays [16]. They are for example, the lightest supersymmetric particles like neutralinos, soft charginos that escape detection, neutrinos in extra dimensions, Dark Matter, Higgs decays to Majorons. It is evident from these examples that answers to todays most important physics questions, like the understanding of the mechanism of EWSB, existence of Dark Matter, matter-antimatter asymmetry and inclusion of gravity in SM can be manifested in this invisible decay channel of Higgs. So it is important to investigate this mode with high precision instruments [16].

The estimated CEPC capabilities are presented in a model-independent way, since the total cross-section measurement of the $e^+e^- \rightarrow ZH$ can be done at the CEPC, the total width is only constrained by the total cross-section, thus facilitating measurements of coupling scale factors unimpeded by theoretical preconceptions. The coupling strength g_{ZZH} is related to the cross-section in a way that g^2_{ZZH} is proportional to the cross-section $\sigma = \frac{N}{\epsilon L}$, where N is the number of ZH events, ϵ is the efficiency and L is the luminosity. In the SM, an invisible Higgs decay is $H \rightarrow ZZ^* \rightarrow 4\nu$ process and its BF is small 0.1%. If we found sizable invisible Higgs decays, it is clear new physics signal.

2.4 HIGGS-STRAHLUNG

In this dissertation we focus mainly on the Higgs-strahlung process which will be the main production mechanism of the future CEPC collider. The integrated cross section of the Higgs-strahlung is given by the formula,

$$\sigma(e^+e^- \to ZH) = \frac{G_F^2 M_Z^4}{96\pi s}(\nu_e^2 + a_e^2)\lambda^{1/2}\frac{\lambda + 12M_Z^2/s}{(1 - M_Z^2/s)^2} \tag{2.1}$$

where λ is the phase space function given by

$$\lambda = (1 - M_H^2/s - M_Z^2/s)^2 - 4M_H^2 M_Z^2/s^2 \tag{2.2}$$

$G_F = 1.16637 \times 10^{-5} GeV^{-2}$ is the fermi coupling constant, $a_e = -1$ and $\nu_e = -1 + 4s_W^2$ with $s_W^2 = 0.23149$ is the electroweak mixing angle [17, 18, 19]. The Figure 2.3 shows the cross section of Higgs-strahlung process, as a function of center of mass energy and as a function of Higgs mass. The production cross-sections have a sharp increase at the threshold center of mass energy $\sqrt{s} \sim M_Z + \sqrt{2}M_H$ after which it decreases as $\sim 1/s$. There is a decrease in

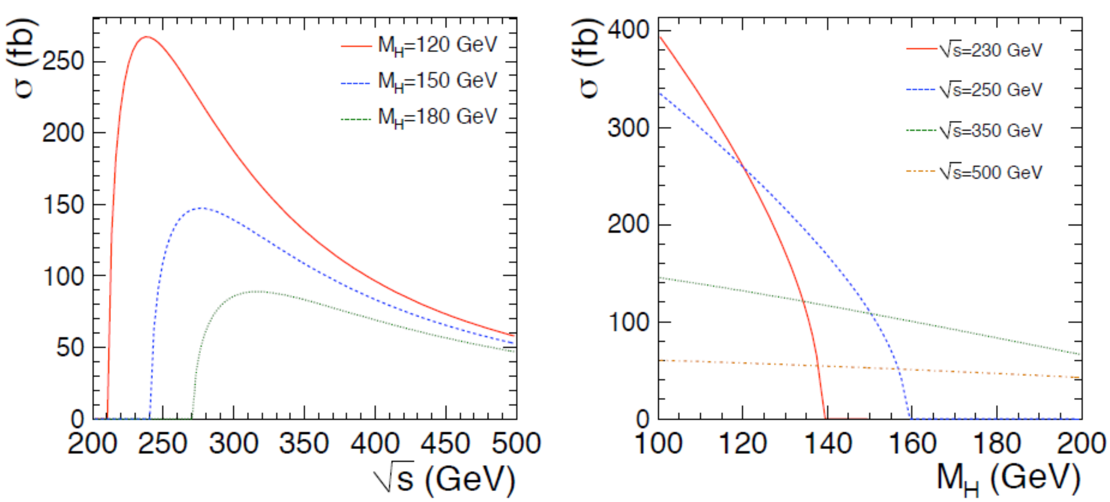

Figure 2.3. Cross section of Higgs-strahlung process, as a function of center of mass energy and as a function of Higgs mass [17].

cross section as the Higgs mass increases (left), and cross-section decreases with increasing center of mass energy for an average Higgs mass [17]. To achieve maximum cross section, the center of mass energy should be just above the threshold energy.

The angular distribution of the Higgs-strahlung process as a function of the scattering angle is shown in the Figure 2.4 after detector simulation. Z production angle is the angle between Z and the z-axis. Its distribution for the most part is central and this characteristics distinguishes it from other SM background angular distribution.

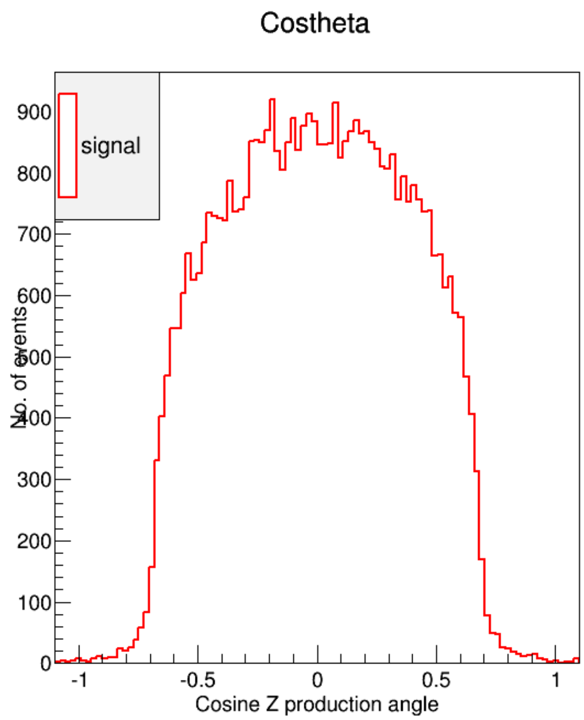

Figure 2.4. Cosine of Z polar angle for Higgs-strahlung process.

2.5 STUDY OF THE HIGGS AT THE CEPC AND LHC IN A NUTSHELL

In an electron positron collider, the final state depicts precisely the physics interactions involved. Figure shows the $pp \to HX$, $H \to b\bar{b}$ at the LHC and the the Higgs-strahlung in $Z \to \mu^+\mu^-$ channel at the e^+e^- collider, emphasizing the clean experimental condition at electron positron collider [20, 21].

At the LHC, the physics involves the scattering process of proton constituents or the partons (quarks and gluons), these are strongly interacting particles and the energy is upto several TeV. There are enormous amounts of QCD backgrounds and the signal to background ratio is small. The main Higgs production mechanism is the gluon gluon fusion. At the CEPC, the scattering process of e^+e^- provides an unblurred experimental environment, clear cut initial state, tunable energy, beam polarization and relatively small backgrounds. Figure 2.5 shows the $pp \to HX$, $H \to b\bar{b}$ at LHC and the Higgs-strahlung in $Z \to \mu^+\mu^-$ channel at the e^+e^- collider [22]. The main Higgs production is through the Higgs-strahlung process at 250 GeV. The LHC can trigger only one event in 10^7 events, while the CEPC will have untriggered operation and can find signals of unexpected new physics that is apparent in events that may not be selected by the LHC trigger scheme [21]. Figure 2.6 shows the comparison between the resolution of CEPC to that of the LHC [21].

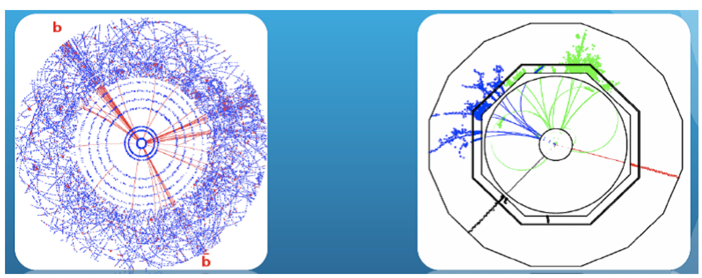

Figure 2.5. The $pp \to HX$, $H \to b\bar{b}$ at LHC and the Higgs-strahlung in $Z \to \mu^+\mu^-$ channel at the e^+e^- collider [22].

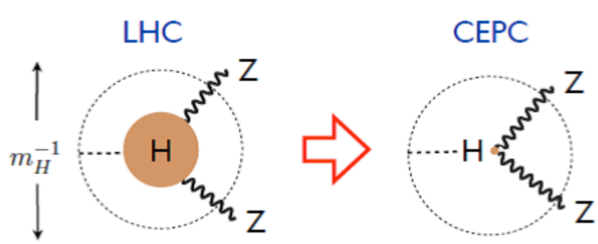

Figure 2.6. The CEPC will probe whether the Higgs is truly elementary with a resolution up to a hundred times more powerful than the LHC [21].

The direct production at CEPC along with its high sensitivity to new physics by means of precision measurements will contribute to LHC findings by improving and verifying each others analysis. This can be achieved by thorough and exhaustive information on measurements of wide variety of observables in different scenarios made by CEPC and LHC along with close alliance of experts consisting of theorists and experimentalists working meticulously [22].

2.6 EXPERIMENT RESULTS ON HIGGS TO INVISIBLE STUDY AT LHC

Searches for Higgs to invisible decays have been done at the ATLAS and CMS experiments. The study is done by means of the $q\bar{q} \rightarrow ZH$ process using missing transverse energy, E_t^{miss}, against leptonic Z decays. Since the initial momenta of the partons cannot be precisely determined, they cannot reconstruct missing Higgs mass, using the recoil mass method. This method is model dependent since the cross section of ZH in pp collision is assumed as that in the SM [23, 24, 25, 26].

At the LHC, the measured quantity is the rate, which is the product of the production cross-section σ_i and the branching ratio of the decay channel BR_j:

$$Rate_{ij} = \sigma_i \times BR_j = \sigma_i \times \frac{\Gamma_j}{\Gamma_{tot}}, \tag{2.3}$$

Γ_j is the decay coupling, Γ_{tot} is sum of all the Higgs couplings.

CHAPTER 3

THE CIRCULAR ELECTRON POSITRON COLLIDER

3.1 INTRODUCTION

This chapter describes the experiment for my analysis. I describe the different components of the detector which are used to identify the final state particles.

3.2 THE CEPC PROJECT

With the discovery of the low mass Higgs boson, and stimulated by ideas of a Circular e^+e^- Higgs factory in the world, CEPC-SppC (Circular Electron-Positron Collider+Super proton-proton Collider) configuration was proposed in Sep. 2012 in China [20]. The CEPC-SppC identifies itself as the essential collider project for particle physics in China. Rendering high luminosity at its center-of-mass energy, CEPC (240 - 250 GeV) it can be upgraded to a high energy (70 $-$100 TeV) SppC, which will complement with the CEPC and further extend the discovery reach. CEPC can operate at the Z pole at a center of mass energy of 91 GeV. CEPC is likely to be cost-effective and technologically expedient. The preCDR study examined these aspects. The CEPC preCDR study has gained betterment from the progress in the ILC (International Linear Collider) accelerator and detector designs, and the mechanism and proficiency achieved through the ILC projects and the LHC experiments [20]. The CEPC study team, along with the FCC (Future Circular Collider) and ILC community, will cater to the needs of future high energy colliders and experiments which will guarantee that the elementary particle physics remain a vital and dynamic field of fundamental investigation for many years to come. I will focus on CEPC as the Higgs factory, its timeline is shown in the Table 3.1. The reference for this chapter is CEPC preCDR. Compared to ILC, the CEPC does not require push-pull system and its energy range is at 250 GeV as opposed to a maximum of 1 TeV at the ILC. From ILD to CEPC there is, changed granularity (no power

Table 3.1. Goal and timeline for the CEPC

Goal	**CEPC Timeline**
Pre study	2013-15
Pre-CDR	By 2014
Funding request R&D	2016-2020
Engineering Design	2015-2020
Construction	2021-2027
Data taking	2028-2038

pulsing), changed luminosity, changed VTX inner radius and TPC outer radius, changed detector half Z, changed yoke/muon thickness, changed sub detector design among others. All changes need to be implemented into simulation, iterated with physics analysis and cost estimation. Required performance for the CEPC sub-detectors for measuring Higgs decays is enumerated in the Table 3.2. A CEPC ring of 100 km circumference is recently proposed, Figure 3.1.

Table 3.2. Required performance for the CEPC sub-detectors for measuring Higgs decays [21].

Physics Process	Measured Quantity	Critical Detector	Required Performance
$ZH \to \ell^+\ell^- X$	Higgs mass, cross section	Tracker	$\Delta(1/p_{\mathrm{T}}) \sim 2 \times 10^{-5}$
$H \to \mu^+\mu^-$	$\mathrm{BR}(H \to \mu^+\mu^-)$		$\oplus 1 \times 10^{-3}/(p_{\mathrm{T}} \sin\theta)$
$H \to b\bar{b},\ c\bar{c},\ gg$	$\mathrm{BR}(H \to b\bar{b},\ c\bar{c},\ gg)$	Vertex	$\sigma_{r\phi} \sim 5 \oplus 10/(p \sin^{3/2}\theta)\ \mu\mathrm{m}$
$H \to q\bar{q},\ VV$	$\mathrm{BR}(H \to q\bar{q},\ VV)$	ECAL, HCAL	$\sigma_E^{\mathrm{jet}}/E \sim 3-4\%$
$H \to \gamma\gamma$	$\mathrm{BR}(H \to \gamma\gamma)$	ECAL	$\sigma_E \sim 16\%/\sqrt{E} \oplus 1\%\ (\mathrm{GeV})$

By applying a radio frequency voltage to separated sections of the tube, charged particles like electrons and positrons can be accelerated through a tube because the charged particles experience an accelerating electric field when they pass the gap [20]. The charged particles attain double the energy they would have gained from just the application of the maximum

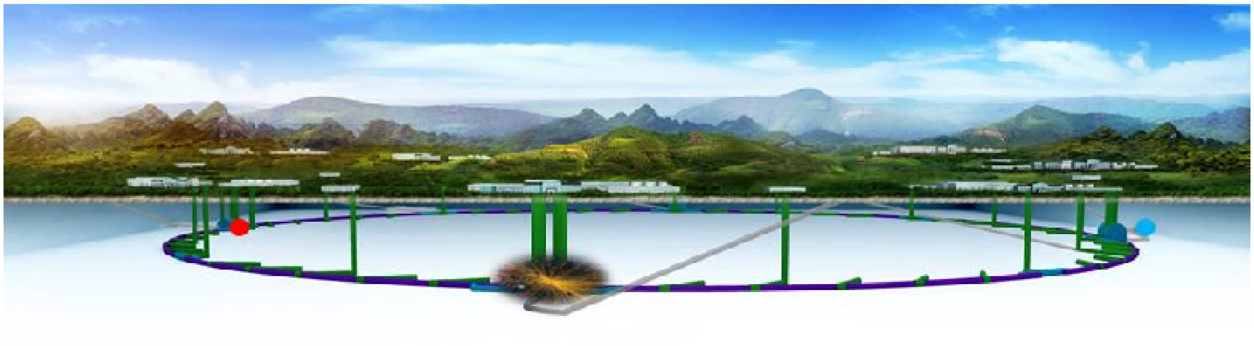

Figure 3.1. The CEPC ring with 100 km circumference recently proposed.

field of the RF when they arrive at the next gap at the right phase of the RF voltage and thus they are accelerated again.

Synchrotron radiation SR is a radiation which occurs when charged particles are accelerated in a curved path or orbit. The Booster is a circular accelerator that accelerates beam particle energy from low to high before injection. It uses magnets to bend the beam of charged particles in a circular path.

- In a circular collider there is energy loss due to SR, and it is proportional to the fourth power of the beam energy and is inversely proportional to the square of the radius of the path, so a low beam energy of 120 GeV to reduce energy loss due to SR as well as keeping it close to the Higgs cross-section energy of 125 GeV.

- RF system provides power to accelerator beams to the desired energy and compensates the energy loss due SR around the ring. Keeping RF power of 50 MW and achieve high luminosity we need to store more beam current in the ring. This is realized by a bigger ring, so a 50 km circumference tunnel is proposed. It will also encase proton-proton beam in future.

- As a Higgs factory the peak luminosity of $2 \times 10^{34}\ cm^2 s^{-1}$ is required to meet the physics goals.

- A linac will be the main injector of the CEPC. The electron and positron will be accelerated to 6 to 10 GeV.

- A booster is considered to be in the same tunnel of the main ring to save budget, and connect with transport lines to the ring and the linac. A pretzel orbit scheme is adopted for pre-CDR.

- There are eight bent and eight straight sections. RF cavities are distributed in all the straight sections to overcome the loss due to synchrotron radiation. IP1 and IP3 are for CEPC, the other two are for future SppC as shown in the Figure 3.2.

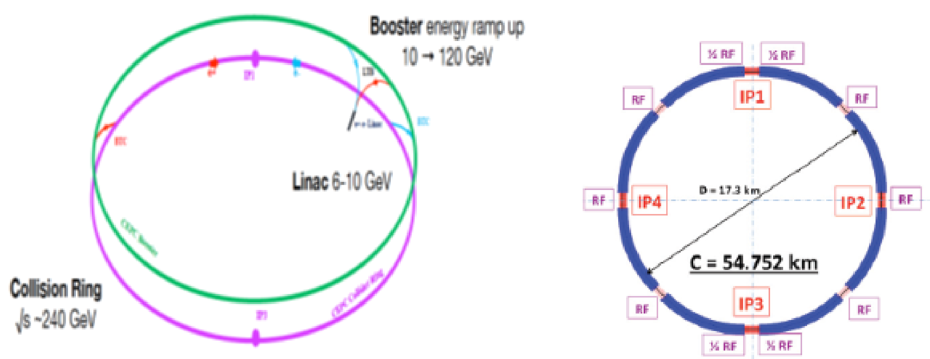

Figure 3.2. Accelerator chain (left) and CEPC lattice and RF section around the ring (right) [21].

The Beamstrahlung is a process of energy loss by the incoming electrons deflected by the electromagnetic field of the electron (positron) bunch moving in opposite directions. The beam energy spread is the energy dispersion of the incoming beams. They are determined by the beam parameters at the interaction point (IP), which are listed in Table 3.3. The Higgs-strahlung process and the Higgs recoil mass precision measurement is sensitive to these two beam factors.

3.3 DETECTOR OVERVIEW

Table 3.3. CEPC parameters as a Higgs factory.

Parameter	**Value**	**Unit**
Center of mass energy	250	GeV
Peak Instantaneous Luminosity	2×10^{34}	$cm^2 s^{-1}$
Integrated Luminosity over 10 years	5	ab^{-1}
Tunnel Circumference	54.752	km
Number of bunches per beam	50	
Number of particles in each bunch per injection	3.7	10^{11}
Beam size σ_x/σ_y	73.3/0.16	μm
Beam size σ_z	2260	μm
Beam current	16.6	mA
SR power/beam	51.7	MW
SR loss/turn	3.11	GeV
Number of Interaction points IP	2	
Bunch spacing	3.5	μsec
Number of Higgs events over 10 years period	1	Million

CEPC will be the outcome of creative design by physicists and engineers, supported by a strong frame of past and continuing process of detector research and development [21]. Figure 3.3 shows the geometry of the conceptual CEPC detector as implemented by Mokka and Geant 4. While each component has received advancements from ongoing development, like ILD and FCC, the CEPC design has merged these components into a consolidated system for optimized measurements of jet energies, as well as of charged leptons, photons and missing energy, based on the Particle Flow Algorithm (PFA) approach. CEPC was formulated as a fully integrated, amalgamated design with the fundamental features of compactness, pixel based vertex detecting, silicon-based tracking, a time projection chamber, fine-grained calorimetry and a high central magnetic field provided by a solenoid. On the outside of the coil, the iron return yoke is instrumented as a muon system and as a tail catcher calorimeter. This design has been developed for experiments at a future electron positron collider, assem-

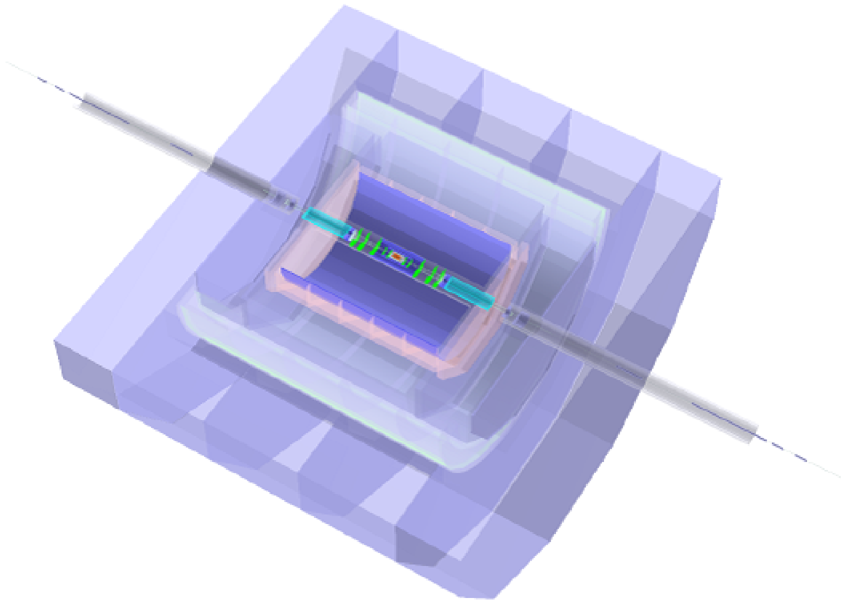

Figure 3.3. Geometry of the conceptual CEPC detector as implemented by Mokka and Geant 4 [21].

bled on substantial acquaintance with previous detectors, and harnessing major advances in sensors, materials, and electronics.

CEPC uses a right-handed coordinate system with its origin at the nominal interaction point. The +z axis is along the beam pipe in the direction of the electron, the +x axis points away from the center of the CEPC ring and the +y axis points vertically upward. Cylindrical coordinates (r, ϕ) are used in the transverse plane, ϕ being the azimuthal angle around the beam pipe. The pseudorapidity η is defined as $\eta = -\ln\tan(\theta/2)]$ where θ is the polar angle. Figure 3.4 shows the cross-sectional view of the CEPC detector.

3.4 VERTEX DETECTOR

The CEPC vertex system consists of a multi-layer pixel-vertex detector (VTX) having a pure barrel geometry, which has three super-layer of two layers each as shown in Figure 3.5.

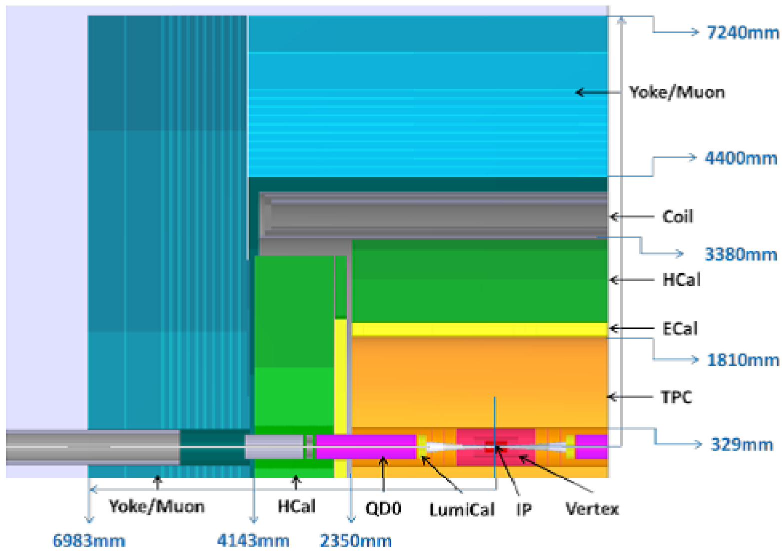

Figure 3.4. Cross-sectional view of the CEPC detector [21].

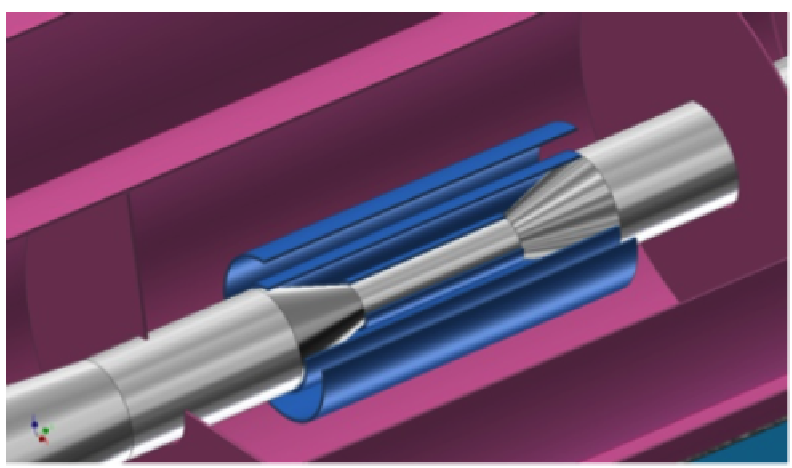

Figure 3.5. The vertex detector [21].

The first super-layer is only half as long as the outer to reduce the background hits, optimized for point resolution and minimum material thickness. An assemblage of silicon strip and pixel detector encompass the VTX detector. In the barrel, to bridge the gap between the VTX and the TPC two layers of silicon strip detectors (SIT) are laid out. To provide low angle tracking coverage in the forward region, a system of two silicon-pixel disks and five silicon-strip disks (FTD) are used. CMOS Pixel Sensors (CPS), Fine Pixel CCD (FPCCD) sensors, and Depleted Field Effect Transistor (DEPFET) sensors are currently the three sensor technology options that are actively developed for the CEPC vertex detector. They exhibit to possess the potential of meeting or coming close to the detector requirements. The main performance goals of the vertex detector are:

- Spatial resolution near IP to be better than 3 micrometer,
- Material budget below 0.15% radiation length X_0 per layer,
- First layer located as close as 16mm to the IP,
- Detector occupancy not to exceed 1%,
- Power consumption should be kept below $50mW/cm^2$,
- Readout time should be shorter than 20 microsecond, to minimize event accumulation from consecutive bunch.

3.5 SILICON TRACKER

The silicon part of the CEPC tracking system comprises of four components: two barrel components, the Silicon Inner Tracker (SIT) and the Silicon External Tracker (SET), one end cap component End-cap Tracking Disk (ETD) behind the endplate of the TPC, and the Forward Tracking Disk (FTD). They form the Silicon Envelope. The overall layout of the system is shown in Figure 3.6.

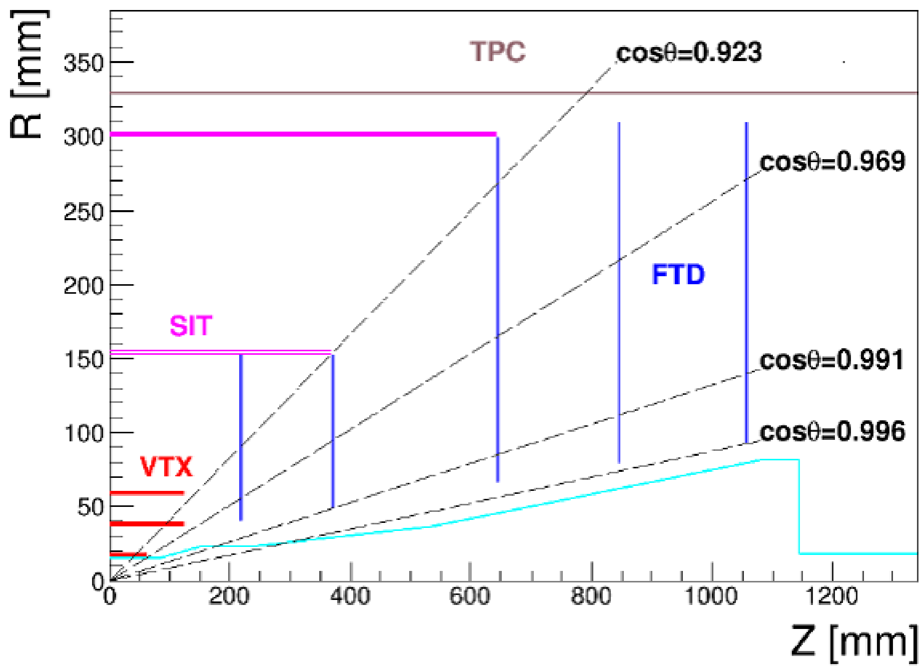

Figure 3.6. Preliminary layout of the CEPC silicon tracker. The red lines indicate the positions of the vertex detector layers and the blue lines are the SIT and FTD for the silicon tracker. The SET and ETD, which outside the TPC are not shown [21].

The overall momentum resolution is improved by the barrel silicon parts SIT and SET which provide precise space points before and after the TPC and links the VTX detector with the TPC. Figure 3.7 shows the resolution of the transverse impact parameter as a function of single muon track momentum estimated for the CEPC baseline design for polar angles of θ°and 80°, and compared to analytical results obtained from the equation $\sigma(r\phi) = a \oplus \frac{b}{p(GeV)\sin^{3/2}\theta}\mu m$, where, a=5 and b=10.

It also helps in extrapolating from the TPC to the calorimeter. The ETD completes the coverage of the TPC with silicon tracking, located within the gap separating the TPC and the end-cap calorimeter. Collectively, these systems serve in calibrating the overall tracking system, especially the TPC. The time-stamping of the tracks and assignment of them to a given bunch within an CEPC bunch train is enabled by good timing resolution of the silicon detectors relative to the time between bunches in the CEPC together with the high spatial

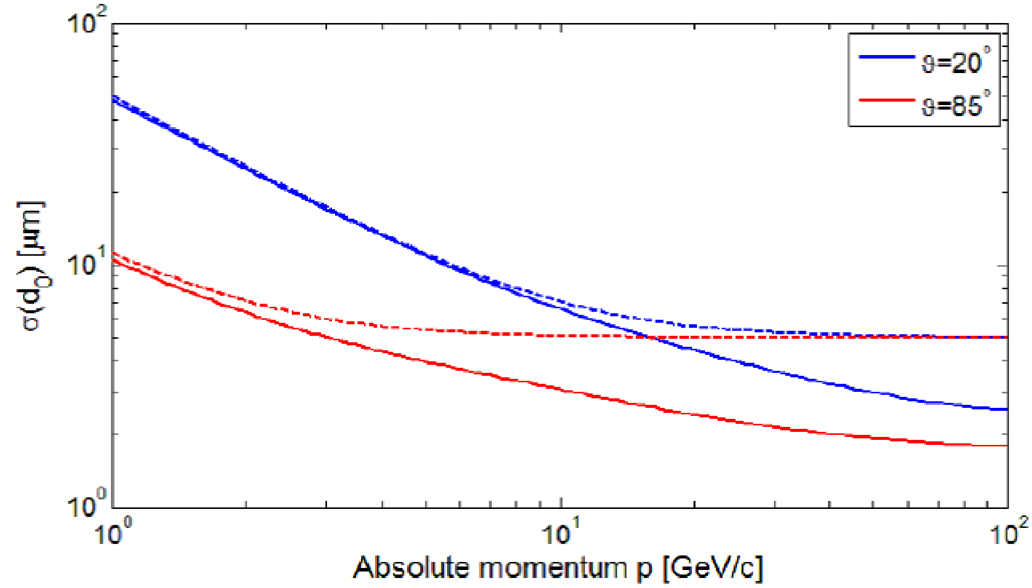

Figure 3.7. Resolution of the transverse impact parameter as a function of single muon track momentum estimated for the CEPC baseline design for polar angles of θ°and 80°, and compared to analytical results obtained from the equation $\sigma(r\phi) = a \oplus \frac{b}{p(GeV)\sin^{3/2}\theta}\mu m$, where, a=5 and b=10 [21].

precision. Efficient and precise tracking down to very small angles in the very forward region, where the TPC does not provide any coverage is provided by a system of seven silicon disks (pixel and strips).

3.6 THE MAIN TRACKING DETECTOR TPC

A large volume Time Projection Chamber (TPC) with up to 224 points per track is a unique characteristic of CEPC. Figure 3.8 shows the TPC structure.

TPC is modified to achieve three-dimensional point resolution and minimum material in the field cage and in the end-plate. It also provides dE/dx based particle identification.

The TPC comprises of two chambers filled with gas, with a high voltage applied across the length of the TPC. The motion of charged particles ionizes gas molecules which is carried

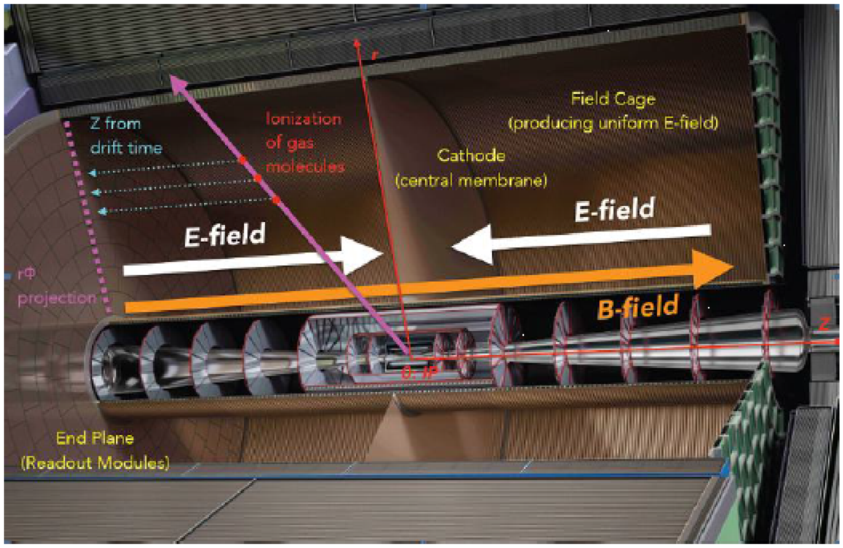

Figure 3.8. Structure of the TPC [21].

by the electric field toward the end plate caps, where they are absorbed and detected. The drift time is used to calculate the position of the ionization.

Despite the fact that the TPC is less accurate than the VTX, it has the supremacy of being able to track a large continuous volume inside the detector. A large volume of space relatively can be easily covered by the TPC.

The mechanical constitution of the TPC comprises of an endplate, where the readout of the amplified signals occurs using custom-designed electronics, and a field cage, made from advanced composite materials. Two options for the gas amplification systems are Micromegas (Micro-MEsh Gaseous Structure) and Gas Electron Multipliers (GEM). Currently, either option would use pad size of $6 \times 10\ mm^2$, leading to about 10^6 pads per endplate.

The drift velocity and the diffusion constant are determined by the properties of the gas. To preserve an intrinsically excellent resolution, the parameters are chosen to minimize the diffusion in the transverse and longitudinal directions. T2K gas mixture (Ar-CF4(3%)-isobutane (2%)) is a promising candidate for a drift length of more than 2 m and a high field of 3.5 T.

3.7 CALORIMETRY SYSTEM

The Electromagnetic Calorimeter (ECAL) measures photons and charged particles, by virtue of the fact that it will leave a shower of secondary particles as they interact with tungsten. These secondary particles are then detected by the position sensors. The analysis of the shapes of the shower give the identification of the original particle type. Electrons and photons generate broad showers with large energy depositions. Muons are minimum ionizing particles and tend to pass easily through the calorimeter. Pions and kaons vary in reaction, sometimes passing easily through the calorimeter, other times suffering a nuclear collision followed by a hadronic shower. The ECAL is made up of interleaved layers of absorbing

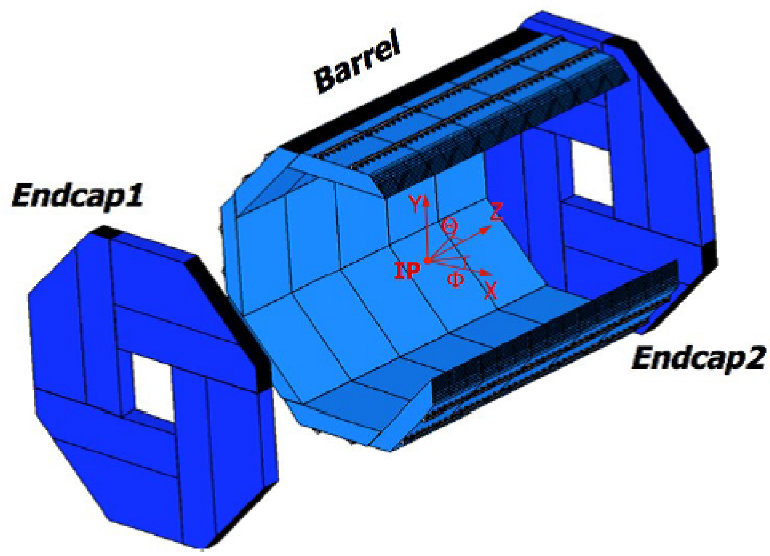

Figure 3.9. View of the SiW ECAL geometry. The barrel is segmented in 8 staves of 5 modules. Each barrel module incorporates 3 towers of 11 alveoli in which detector slabs are lodged. The end caps are segmented in quadrants of 2 modules (with 2 and 3 towers) [21].

material (tungsten) and position sensors. The two options for the position sensors are silicon pixel or pad sensors and the other is to use scintillator plastic strips. Tungsten (radiation length X_0 = 3.5 mm, Moliere Radius RM = 9 mm and interaction length = 99 mm) as absorber material fulfills the requirements on granularity, compactness and particle separation. Compared to e.g. lead, a better separation of electromagnetic showers generated by near-by particles is achieved along with a compact design with a depth of roughly 24 X_0 within 20 cm. The ECAL is longitudinally segmented into 30 layers, possibly with varying tungsten thicknesses to attain an adequate energy resolution. In order to optimize the pattern recognition performance, the active layers (either silicon diodes or scintillator) are segmented into cells with a lateral size of 5 mm. The Figure 3.9 shows the ECAL geometry.

The main function of the HCAL is to differentiate the deposits of charged and neutral hadrons and to do the accurate measurement of the energy of the neutrals. They contribute around 10% on average to the jet energy, which fluctuates over a wide range from event to event. The dominant contribution is the accurate measurement of the particle flow resolution for jet energies up to about 100 GeV. At higher energies, the performance is dominated by confusion. A better topological pattern recognition and energy information are important for correct track cluster assignment. The HCAL is formulated as a sampling calorimeter made up of steel absorber and scintillator tiles (analogue HCAL) or gaseous devices (semi-digital HCAL) as active medium. The rigidity of stainless steel, allow for a self-supporting structure without auxiliary supports (dead regions). Compared to other heavier materials, iron has a moderate ratio of hadronic interaction length (λ_f= 17 cm) to electromagnetic radiation length (X_0 = 1.8 cm) which enables a fine longitudinal sampling in terms of X_0. The detector volume and readout channel count within admissible level is achieved by reasonable number of layers in a given total hadronic absorption length. Required for particle separation and weighting, this fine sampling is favorable both for the measurement of the substantial electromagnetic energy part in hadronic showers and for the topological resolution of shower substructure. The scintillator-tile based AHCAL and the Glass Resistive Plate Chamber (GRPC) based SDHCAL are the two baseline technology options that have been developed.

3.8 MUON SYSTEM

The muon system will reside in the outermost part of the whole detector. Figure 3.10 shows the muon system layout for the CEPC detector. It is divided into barrel and end-caps. Both the barrel and end-caps are further segmented into modules. For CEPC muon system, dodecagon segmentation is selected for the baseline design. The number of sensitive layers and the thickness of the iron (or tungsten) in the absorbers are two critical parameters. The total thickness of the iron absorber should not exceed 13 times the nuclear interaction length (λ) of iron, for the center of mass energy 240 GeV. 8λ distributed in 8 layers will provide efficient muon tracking. 4 cm gaps between neighboring iron layers give adequate space for the RPC and scintillator strips sensors. Figure 3.11 (left) shows that muon detection efficiency is high for muon energy as low as 4 GeV and it is 95% even after penetrating 8 layers. Figure 3.11 (right) shows the detection efficiencies for 10, 30 and 50 GeV muon energies, respectively.

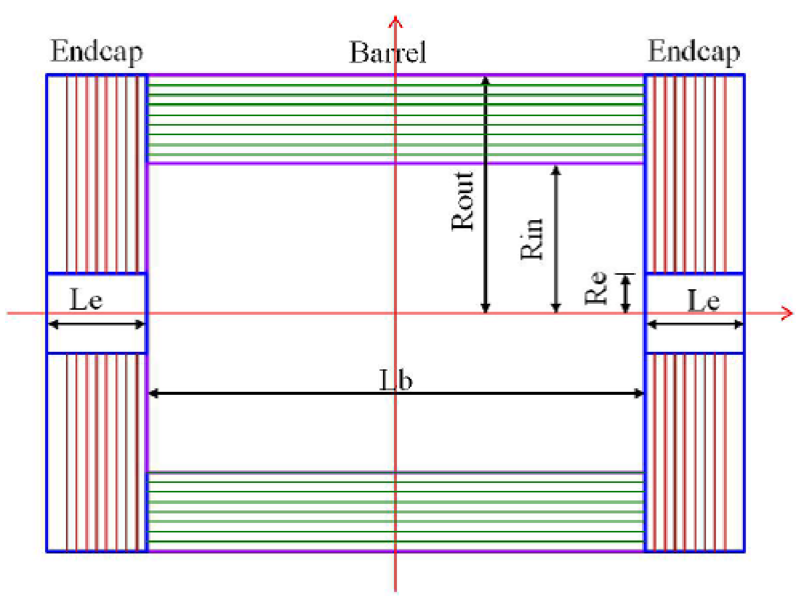

Figure 3.10. The muon system layout for the CEPC detector [21].

It is inferred from the graph that pion detection efficiency is independent of energy and decreases drastically with increasing number of layers and vanishes after 8 layers which is the chose number for CEPC baseline design. The CEPC muon system solid angle coverage in accordance with TPC should be $0.98 \times \pi$. The position resolution of $\sigma_{r\phi} = 2.0$ cm and $\sigma_z = 1.5$ cm are required. Maintaining 95% efficiency for the module over 5-10 years of running with gas detector option will be a challenge. For the dimension and segmentation required by the baseline design, the total sensitive area of the muon system add up to 8600 m^2. With strip width of 3 cm and 1-D readout (2 ends for barrel and one end for endcap) the total number of electronic channels amount to 5.5×10^4 . RPC with glass and Bakelite options are being studied as they provide following advantages like cost-effective, sturdy, easy construction of large, large signal, simple front-end electronics, good time and spatial resolution. Scintillator strips are another attractive technology for compact and rigid modules with 1-D and 2D readout strip arrays. The required spatial resolution of 3 cm can be achieved with 1 cm thick, 3 cm wide and 2-5 m long scintillator strips.

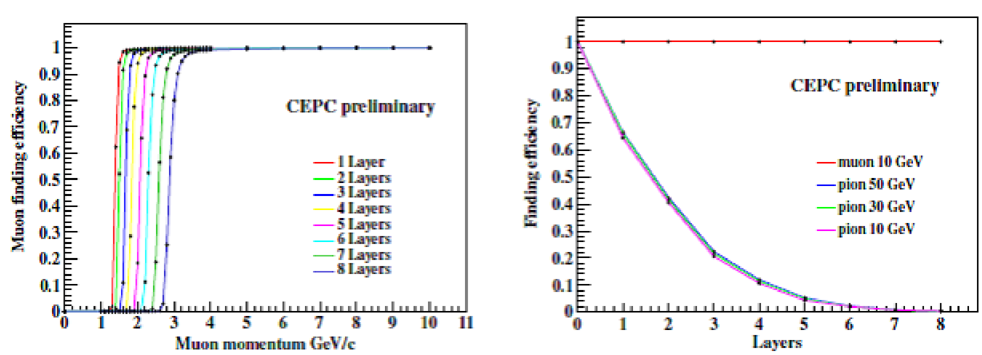

Figure 3.11. The muon detection efficiency as a function of momentum for different numbers of layers of muon detector (left), and the pion detection efficiency as a function of number of layers for different momenta (right) [21].

3.9 DETECTOR MAGNET SYSTEM

The CEPC detector magnet system consists of a solenoidal coil and an iron flux yoke, Figure 3.12, designed to provide and axial magnetic field of about 3.5 T, homogeneous over the tracking volume. The superconducting solenoid has a warm bore of 6.8 m [21] in diameter and 8.05 m in length. The iron yoke is made up of barrel and end-cap components. It provides magnetic flux return, accommodates the installation space for the muon detector and serves as the main support structure for the CEPC detector.

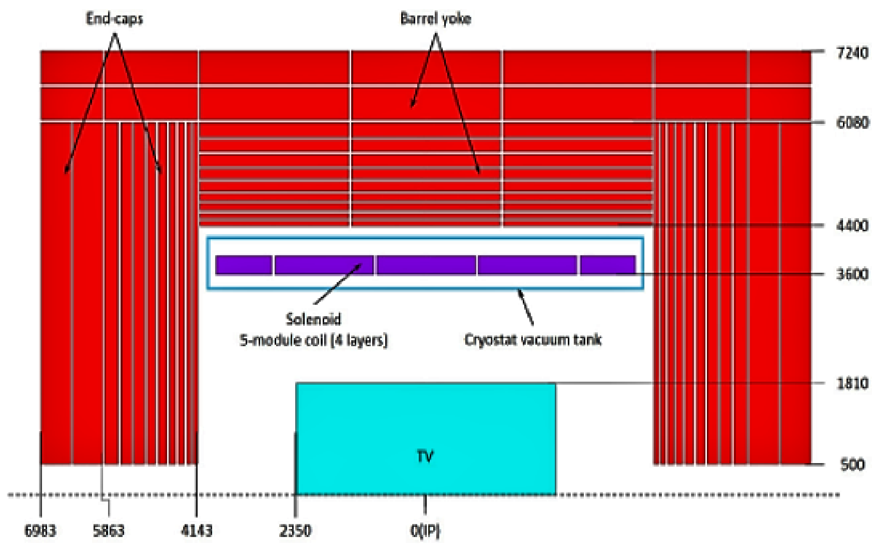

Figure 3.12. The CEPC detector magnet system [21].

For the baseline design five modules with three long sectors each 1.8 m long in the middle and other two short sectors each of length 1 m on either end, are used. The modules are mechanically and electrically connected. They have thermal shields and are supported by tie-rods inside the vacuum tank.

CHAPTER 4

MONTE CARLO SIMULATION

4.1 INTRODUCTION

In this chapter, the sequence for the data analysis using Monte-Carlo (MC) method is described. The details about the signal and background data samples for our study are given. A small section at the end is dedicated to describe how muons are identified at the CEPC.

4.2 DATA ANALYSIS

From the standpoint of data analysis, an event is represented by a set of physics objects, arising from physics interactions, organized in data structures containing information we rely on to analyze and identify the physics [27]. An event is essentially a sequence of numbers, related to the responses of the detector cells. The real data events are acquired by the Data Acquisition System (DAQ). It is however, very useful to have samples of simulated MC events. The sample of events are stored in a data storage system. The reconstruction program transforms these information in higher level quantities, like energies, momenta, multiplicities and so on. For our analysis we are interested in studying specific reactions, so that we want to select only events corresponding to the final state of those reactions [27]. We have to define a procedure, called selection that loops on all events and decides whether to accept or to discard each of them. At the end of the selection what is left is a sample of candidates. In particular, we need two categories of simulated events: the signal events (namely the complete simulation of the final states corresponding to the reaction we want to study) and the background events (namely all those categories of events that are not due to the reaction we want to study but that have similar characteristics of those we are looking for) [27]. Figure 4.1 shows the CEPC simulation, reconstruction software and data analysis chain.

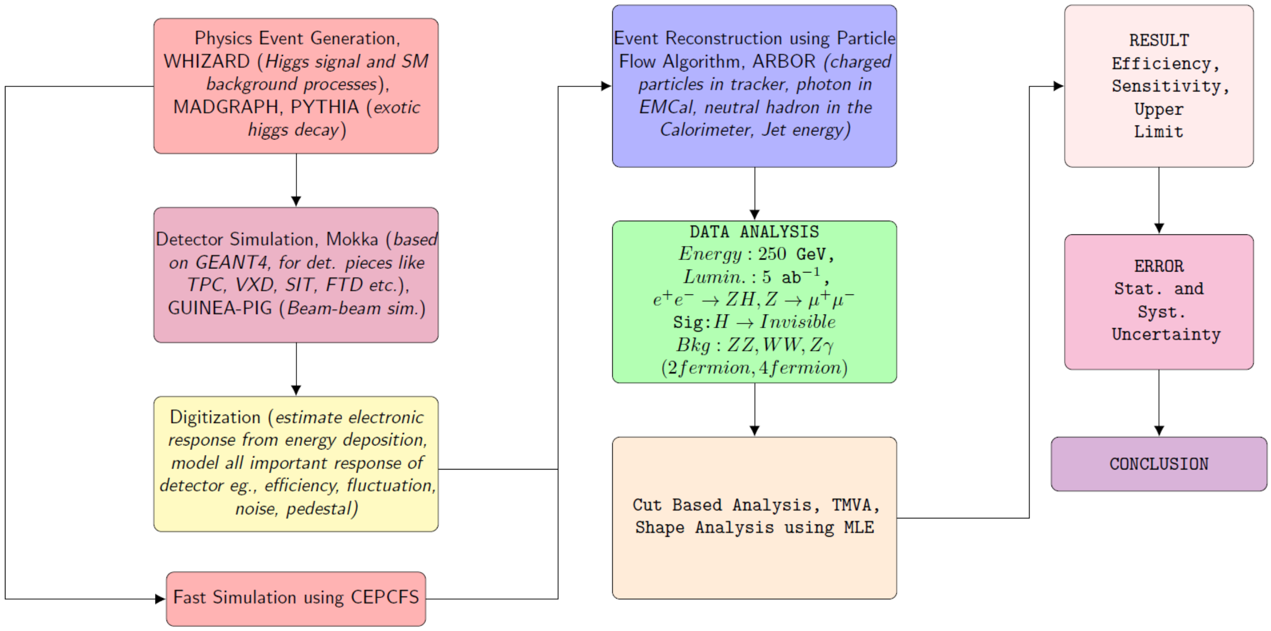

Figure 4.1. CEPC simulation, reconstruction software and data analysis chain.

4.3 DETECTOR SIMULATION AND SOFTWARE CHAIN

The simulation of the CEPC detector makes use of the ILC software chain. CEPC uses iLCSoft [28], the standard software chain for the linear collider studies, as the software framework for its simulation studies. iLCSoft provides a uniform data format, common data management services and rich reconstruction/analysis functionalities. Dedicated software tools have also been developed, including the CEPC fast simulation tool and a general physics analysis framework. In addition, GuineaPig [29] is used to generate the beam background and beam energy spectrum. The CEPC detector simulation studies follow three major steps: generation of physics events, simulation of detector response and reconstruction of physics objects. Higgs signal and SM background processes are simulated with a dedicated event generator, WHIZARD [30, 31, 32]. In addition, MADGRAPH [33, 34] and PYTHIA [35, 36] have been used to generate samples for Higgs exotic decay studies. The event generators are interfaced to Mokka [37] /GEANT4 for detector simulation. Geant4 (for GEometry ANd Tracking) is a platform for “the simulation of the passage of particles through matter” using the MC methods. Reconstruction of conceptual detector geometry has been fully implemented and validated.

4.4 PHYSICS EVENT GENERATION

WHIZARD is the universal MC event generator program that automatically computes complete tree-level matrix elements, integrates them over phase space, evaluates distributions of observables, and produces (a set or sequence of items) by performing specified mathematical or logical operations on an initial set unweighted event samples which are ready to be used directly in detector simulation [30, 31]. Using current hardware, the program has successfully been applied to hard scattering processes with up to eight particles in the final state, it is not limited by any process complexity. The spin and color correlations are retained as the matrix elements are computed as helicity amplitudes. Along with the SM, the MSSM, and many alternative models such as Little Higgs have been put in effect [30]. Anomalous couplings, or effects of extra dimensions or noncommutative SM extensions have been applied. WHIZARD produces complete physical events and covers physics at hadron, lepton, and photon colliders, using standard interfaces to PDF, beamstrahlung, parton shower and hadronization programs.

4.5 DETECTOR SIMULATION

Mokka is a full simulation package using Geant4 for a realistic description of a detector for the future collider which was first developed for TESLA project in Europe [37]. The Mokka current release is able to simulate several detector pieces like TPC, VXD, SIT, FTD, etc.. It can simulate the electromagnetic calorimeter by simulating energy deposition in sensitive volume.

4.6 DIGITIZATION

Digitization is a simulation of the electronics response to the incident particles. It is an essential part of the full simulation. Digitization should simulate all the important response of detector, namely efficiency, dead time/dead zones, fluctuation, noise, pedestal, etc.[21]. It should have a very good understanding of the physics and mechanism of detection. The current CEPC studies use the default digitisation modules in iLCSoft. More realistic digitization should be pursued in future studies. The digitized hits are then reconstructed into physics objects.

4.7 EVENT RECONSTRUCTION

The granularity of calorimeter has been refined for future collider experiments such that the sub structure of showers especially hadronic showers can be recorded to a high precision [38]. Following the idea that shower follows the topology of the tree, the Arbor program was developed, as a Particle Flow Algorithm framework. The idea under this clustering algorithm is based on the topological development of hadronic showers in high granularity sampling calorimeters. The objective of this algorithm is to use the energy deposits in calorimeters as vertexes to connect and thus create an oriented tree-topology. Tested on both simulated data and test beam data, it can successfully separate nearby showers. The objective jet energy resolution at the e^+e^- machines is usually referred to as 3% of relative accuracy, roughly improved by a factor of two than that achieved at ALEPH and CMS [39, 40]. Such accuracy is needed to distinguish the Z boson from W boson in their hadronic decay mode, while it also provides a much better separation between the Z boson and Higgs boson [38].

4.8 FULL AND FAST SIMULATION

Large MC data sets for the the modeling of background processes, estimation of systematic effects, and the study of rare processes with small cross sections are required for physics analysis. This MC production to the finest simulation detail is usually a very CPU-intensive task [41]. The high demand for MC samples rises further as the recorded luminosity at the CEPC, and hence the amount of detector data to be analyzed, increases over time. So, full and fast detector simulation techniques have been developed to achieve the goal of large-scale MC production within the computing limits of the experiment. The geometry of the detector is complicated, the use of Geant4 simulation slows the many physics studies, so a faster simulation method is required [41]. To achieve this, several fast simulation techniques have been developed to complement the full Geant4 simulation. To simulate the progression of particle showers traversing the calorimetry, largely produced by the electromagnetic particles such as electrons and photons, which cause large secondary particle cascades in the complex electromagnetic calorimeter take almost 80% of the full simulation time with Geant4. The fast simulation software speeds up this slowest part of the full simulation by replacing low energy electromagnetic particles in the calorimeter with frozen showers which are pre-simulated and stored in memory as libraries [41]. All Higgs signal and part of the leading SM background samples have been processed with full simulation and reconstruction [43]. The rest of SM backgrounds is simulated with a dedicated fast simulation tool, CEPCFS [21], where the detector acceptance, efficiency, intrinsic resolution for different physics objects and identification efficiency are taken into account. To cross-check samples that were simulated for ILC studies are used as a cross-check [42].

4.9 MONTE CARLO PRODUCTION

The MC samples used for analysis are generated by CEPC simulation group (Dr. Mo and Dr. Li) using the version 1.95 of the event generator WHIZARD [42]. The reference for this chapter for the most part is, "Physics cross sections and event generation of electron-positron annihilations at the CEPC" by X. Mo et al. [42]. Figure 4.2 shows the cross sections of major SM processes.

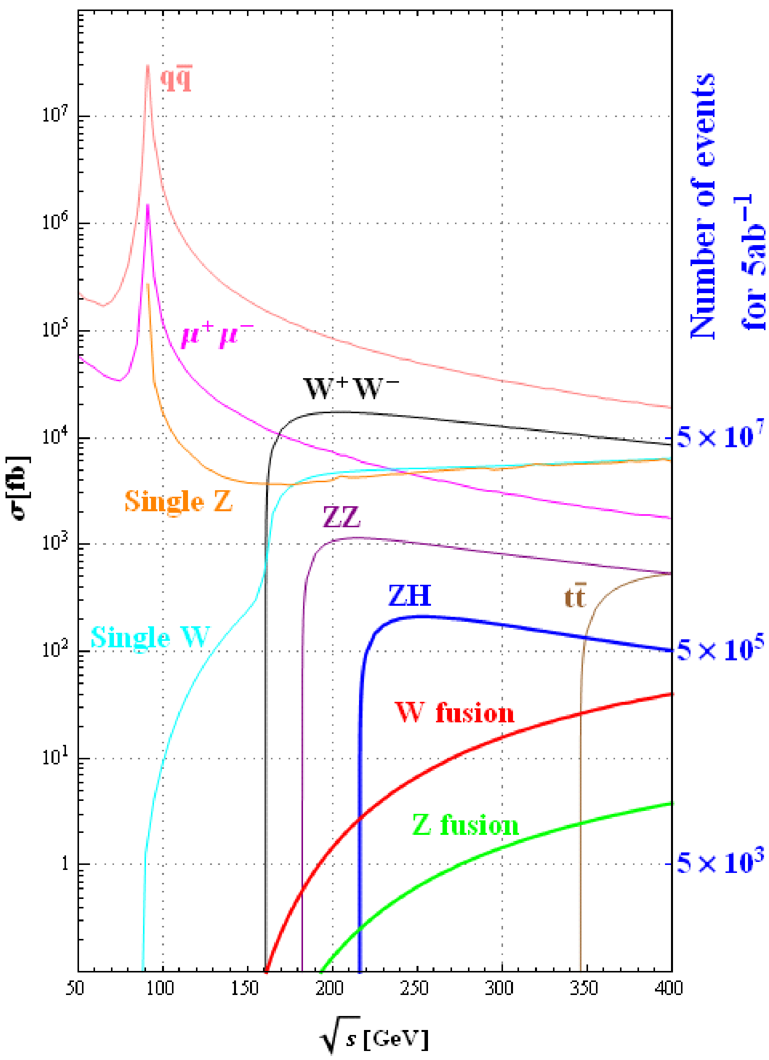

Figure 4.2. The cross sections of major processes of SM [42].

The signal sample was fully simulated with Mokka package, based on the GEANT4 framework, and reconstructed with Arbor in MARLIN framework. The Initial-State Radiation (ISR) effect is included in the simulation. The beamstrahlung effect is studied in both present and absent scenarios. The unified luminosity is 5 ab^{-1}. The cross-sections of the signal and background at 250 GeV are shown in the Table 4.1. The background samples are reconstructed using fast simulation [42]. The samples are stored at the IHEP linux machine (lxslc6.ihep.ac.cn) in the path /cefs/data/stdhep/.

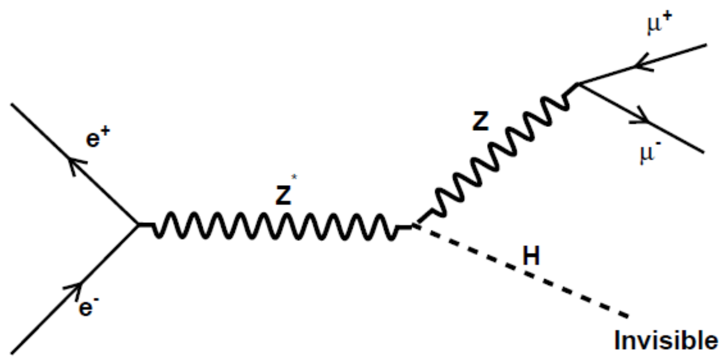

Figure 4.3. Feynman diagram contributing to the signal event.

4.10 SIGNAL EVENT TOPOLOGY

In a signal event, an electron and positron collide, annihilate and produce a Z boson with a Higgs boson, H, recoiling against it. The Z further decays leptonically to two oppositely charged muons and H decays invisibly. Figure 4.3 shows the Feynman diagram.

4.11 SIGNAL SAMPLES

The signal sample consists of Higgs which decays to invisible via and Z decays into oppositely charged muons. The samples generated with WHIZARD undergo full detector simulation.

Table 4.1. The information of the signal sample.

Mode	Cross-section [fb]	Event Expected	Event Generated	Ratio
ZH $Z \to \mu^+\mu^-$	7.10	35849	100000	2.79

4.12 BACKGROUND

The processes that are source of di-muon other than the Higgs-strahlung process, comprise the background. For our analysis we consider two fermion and four fermions processes which are further classified as described below. More than four fermions is not considered, as the cross-section of having more particles at this energy (250 GeV) of CEPC is small. Background samples are prepared using fast simulation.

4.12.1 TWO FERMIONS

The direct di-muon conversion process, the di-tau and the di-quark processes which decay into muons, make the two fermion backgrounds for my analysis. Table 4.2 lists the cross-sections, number of event expected, number of event generated and the "ratio" for the two fermion background processes. Figure 4.4 shows the Feynman diagram contributing to such processes.

$$\text{Ratio} = \frac{\text{Event Generated}}{\text{Event Expected}} \tag{4.1}$$

4.12.2 FOUR FERMIONS

The source of the four fermion processes are the combinations of the intermediate Z and W bosons. They are classified into the following categories. The cross-sections, number of

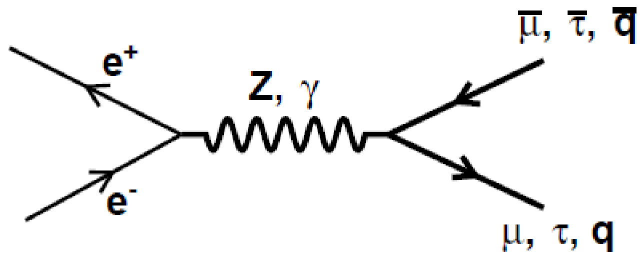

Figure 4.4. Feynman diagram contributing to two fermion backgrounds.

Table 4.2. The cross-sections, number of event expected, number of event generated and the ratio for the two fermion background processes [42].

Mode	Cross-section [fb]	Event Expected	Event Generated	Ratio
qq	49561.3	2.5E+08	2.5E+08	1
$\mu\mu$	4967.58	25086253	25086255	1
$\tau\tau$	4374.94	22093447	22093445	1

event expected, number of event generated and the ratio for the four fermion background processes are listed in Table 4.3. Figure 4.5 shows the Feynman diagram contributing to the background events.

- ZZ- The particles in the final states of "ZZ" samples are combinations of particles with same flavor in principle, as the Z boson can be considered as a particle composed of fermion and anti-fermion with the same flavor for example. They are further classified into hadronic, leptonic and semi-leptonic reactions depending on their decay modes. The leptons in this case are the muons and the tauons as the electrons are considered separately in the single Z process. Its cross-section is listed in Table 4.3. Figure 4.5a show the Feynman diagram contributing to ZZ process.

- WW-These are W-pair production via a Z, s-channel, through triple gauge coupling or t-channel via neutrino. The outgoing W bosons decay to lepton and their accompanying

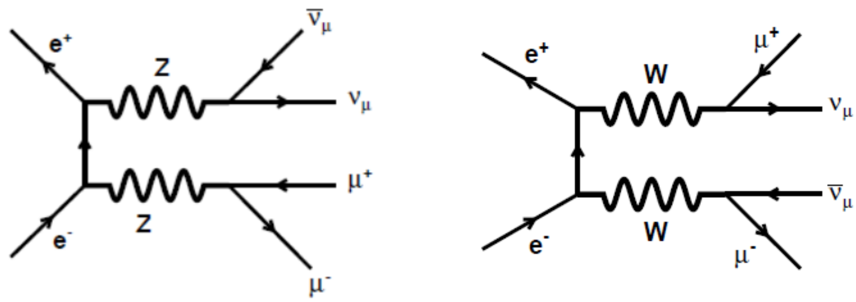

(a) Feynman diagram of the ZZ process.

(b) Feynman diagram of the WW process.

Figure 4.5. Feynman diagram of backgrounds.

neutrino or the flavor changing quarks for various processes. Unlike the Z boson, W boson can be thought to be composed of two quarks with different flavors, therefore the "WW" samples contain the flavor changing processes, for example. Its cross-section is listed in Table 4.3. Figure 4.5b show the Feynman diagram contributing to WW process.

- Single Z -Meanwhile, if there are an electron-positron, or electron neutrino pair, and a Z boson in the final state, this case is named as "Single Z". Its cross-section is listed in Table 4.3.

- Single W- If there are electron-positron together with its neutrino and a W boson in the final state, this type is named as "Single W" process. Its cross-section is listed in Table 4.3.

- Mixed - are processes in which the final particles can come from either ZZ or WW process, these are referred as "ZZorWW" process. Its cross-section is given in Table 4.3.

Table 4.3. The cross-sections, number of event expected, number of event generated and the ratio for the four fermion background processes [42].

Mode	Cross-section [fb]	Event Expected	Event Generated	Ratio
ZZ	1095.84	5533990	5711445	1.032066
WW	8836.41	44623914	44794678	1.003827
SingleZ	1561.79	7887056	7913405	1.003341
SingleW	3437.93	17361537	17361538	1.00
ZZorWW	3559.99	17977937	27333536	1.520393

4.13 MUON IDENTIFICATION

Muons are identified by their ability to penetrate through all the detector components, from tracker to calorimeters, where they ionize and lose small portion of its energy mainly through ionization and then being able to reach the muon detector [43]. The stepper (the algorithm that accounts for the effects of the loss of energy by charged particles due to ionization and the effect of magnetic field inside the detector) initiates with a particle at the interaction point, IP, and it calculates in stages the particle trajectory throughout the detector. There is uniform axial magnetic field B up to the coil. Due to the q ($v \times B$) term the momentum components px and py undergo changes, whereas due to the energy loss dE/dx in material, all the components of particle momentum reduced. Muons may be produced within jets, an efficient algorithm to deal with the identification and separation of particles within jets is important for many of the physics processes of interest.

A large amount of hadron-induced showers produce charged particles that reach the muon detectors and are wrongfully classified as muons by the muon identification algorithm. By utilizing the patterns of hadron showers in HCal compared to the minimum ionizing signals left by muons, these false muon identification can be reduced.

Single muons can be easily identified due to the following two main characteristics: 1) In all sub-detectors, the muon leaves a repetitive pattern (1 to 2 hits per cell) . 2) The muon travels without any strong interations through the sub-detectors. The hadrons do not show these properties typically. Hadrons characteristically interact in the innermost layers of the hadron calorimeter, due to which, they dont reach the end of the hadron calorimeter. An interacting hadron exhibits a set of hits that usually ends in a splash followed by no hits [43].

These factors are implemented into the algorithm in terms of hits per layer in HCal and muon detector and maximum muon identification efficiency is achieved.

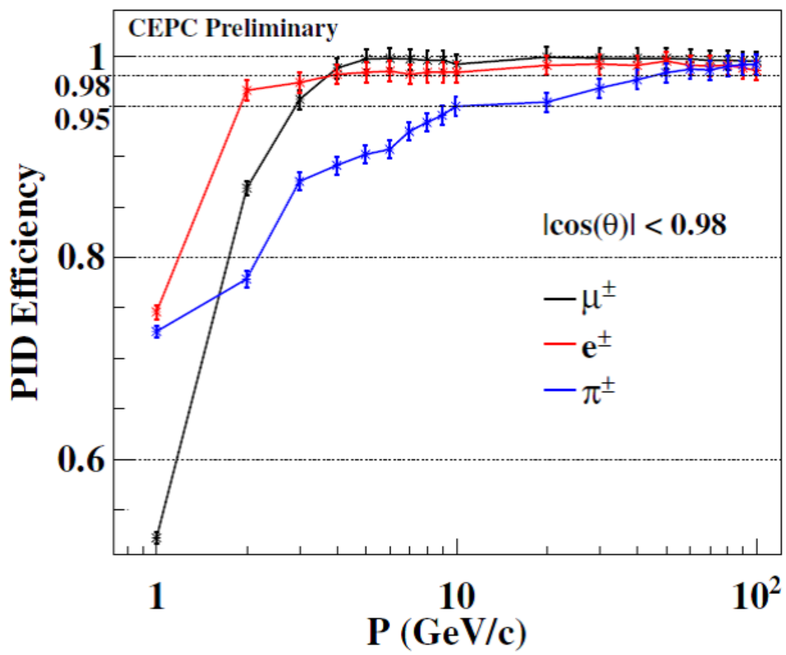

Figure 4.6. Particle Identification performance at the CEPC [21].

CEPC achieves a muon identification efficiency of 97% for muons with momentum greater than 7 GeV/c and pion mis-identification is less than 0.25% (decays in flight) [43]. Figure 4.6 shows the particle identification performance at the CEPC.

CHAPTER 5

ANALYSIS OF SIMULATED DATA

5.1 INTRODUCTION

In this chapter the event kinematics of the recoil mass method is described. The details about the variables we have used for our analysis are given.

5.2 EVENT KINEMATICS

We search for the invisible decays of the Higgs using a recoil mass technique in a model independent way. At the CEPC, we will know the initial momenta of the e^+e^- system, and the four momentum of the Z is measured from the di-muon, from which we can reconstruct the Higgs mass: the invariant mass is calculated using the energy and momentum of the decay products of a single particle and is equal to the mass of the particle that decayed, from the conservation of energy and momentum. Thus the mass of a mother particle can be calculated. The Z is reconstructed using invariant mass measurement of its $\mu^+\mu^-$ pair. The Higgs mass is then reconstructed as the recoil against fully reconstructed Z mass. To accomplish this, muons coming from the signal process need to be identified, this is done through cut-based analysis or a TMVA based selection, and well measured. Some beneficial kinematics associated to the Higgs-strahlung process are the energy and momentum of the Higgs boson and the Z boson [44]. Using the center of mass energy $\sqrt{s}$ =250 GeV, M_Z=91.2 GeV, M_H=125 GeV they can be calculated easily in the laboratory frame and are given by treating the problem as a two body decay.

$$E_H = \frac{s - M_Z^2 + M_H^2}{2\sqrt{s}} \tag{5.1}$$

$$E_Z = \frac{s - M_H^2 + M_Z^2}{2\sqrt{s}} \tag{5.2}$$

$$|P_H| = |P_Z| = \frac{\sqrt{[s - (M_H + M_Z)^2] \cdot [s - (M_H - M_Z)^2]}}{2\sqrt{s}} \tag{5.3}$$

$E_H \approxeq 140$ GeV

$|P_H| \approxeq |P_Z| \approxeq 62$ GeV

Invariant masses of the Higgs and Z bosons, $M_H$and M_Z respectively can be expressed by,

$$M_Z^2 = E_Z^2 - P_Z^2 \tag{5.4}$$

$$M_H^2 = M_{recoil}^2 = s + M_Z^2 - 2E_Z\sqrt{s} \tag{5.5}$$

Where E_Z and P_Z are measured from $Z \to \mu^+\mu^-$. Most importantly the M_H in equation 5.5 gives the so-called Higgs mass, and the M_Z is the Z invariant mass [44]. The possible minimum and maximum momenta of the muons decayed from the Z, $P_{1,2}^{min}$ and $P_{1,2}^{max}$ respectively, can be calculated likewise.

$$P_{1,2}^{min} = \frac{M_Z}{2}\sqrt{\frac{E_Z - |P_Z|}{E_Z + |P_Z}} \approxeq 24GeV \tag{5.6}$$

$$P_{1,2}^{max} = \frac{M_Z}{2}\sqrt{\frac{E_Z + |P_Z|}{E_Z - |P_Z}} \approxeq 86GeV \tag{5.7}$$

5.3 BACKGROUND REJECTION

To distinguish the μ leptons coming from the background, we perform what is called the background rejection procedure [44]. We identify kinematic variables that distinguish signal from the background due to the underlying physics. We then apply cuts on them to suppress background.

Table 5.1. The Variables reconstructed at CEPC.

Name	Comments
Run	index of each run, is the number of files contained by one xml file
Event	index of each event, is how many events each sample file contains
Weight	weight of each event
ntrks	number of tracks
nclus	number of clusters
nPFOs	number of PFOs
Pmax	maximum magnitude of 3-momentum in event
Emax	maximum energy in event
nmuons	number of muons, forced to be 2
nElec	number of electrons passing electron selection
nMuon	number of muons passing muon selection
nGamma	number of photons passing photon selection
VisEn	visible energy in event
VisPx	visible momentum in x direction in event
VisPy	visible momentum in y direction in event
VisPz	visible momentum in z direction in event
RawAllMass	visible mass in event2
MissingMass2	square of missing mass
TotalP	magnitude of 4-momentum of two muons, which is equivalent to the invariant mass
TotalEnergy	total energy of two muons
TotalPx	total momentum in x direction of two muons
TotalPy	total momentum in y direction of two muons
TotalPz	total momentum in z direction of two muons
TotalPt	total momentum in transverse direction of two muons
Rreco1	Recoil mass against muon1
Rcos1	Cosine of muon1 polar angle
Rreco2	Recoil mass against muon2
Rcos2	Cosine of muon2 polar angle
RMass12	Invariant mass of di-muons
Rreco12	Recoil mass against di-muons
Rcos12	Cosine of the di-muon opening angle
Rcosphi12	The angle between the projected 3-vector of two muons in x-y plane

5.4 VARIABLES USED IN THE ANALYSIS

Variables used in the analysis are shown in Table 5.1.

5.5 VARIABLES FOR THE SELECTION CRITERIA

First we recognize and describe the variables that can be used to differentiate signal from the background sufficiently.

Number of Muons, nMuon: The number of muons in the signal process is two. So events that have more than or equal to three muons, allowing the detector to make one mistake, is used to eliminate background. Figure 5.1 shows the distributions of number of muons for the signal and background.

Number of Track, ntrk: The number of tracks also should not be greater than two given that the Higgs decays into invisible final state. However we allow one extra track to avoid simulation error, the number of tracks is taken to be less than or equal to three. Figure 5.2 shows the distributions of number of tracks for the signal and background.

Number of Photons, nGamma: The number of photons should be zero, but allowing one photon and requiring one or less than one photon is a very strong cut and eliminates a significant amount of backgrounds. Figure 5.3 shows the distributions of number of photons for the signal and background.

Transverse Momentum of the di-muon system, P_{Tdm}: Higgs-strahlung result in a two body decay in the final state, where both bosons gain equal transverse momentum which is conserved by their decay products. In order to suppress background, a cut $|P_{Tdm}| > 20$ GeV of the di-muon system is applied for the following reasons. Figure 5.4 shows the distributions of $\mu^+\mu^-$ total transverse momentum for the signal and background.

- Direct muon pair production are back to back and have no transverse momentum.

- For the decay from pair of $\tau^+\tau^-$ or quarks, since the mass of tau and quarks are much less than its momentum, the decay product will be in its direction. So the transverse momentum of the di-muon decaying from the tau or quark pair production are softer, so their cross-sections are maximized at $cos\theta = \pm 1$.

- However in the case of WW conversion the transverse momentum variable is not very efficient in distinguishing it from the signal, as muons are coming from different Ws and the W mass is heavy, so the muons are isotropic.

- The ZZ intermediate process distribution is also maximized at $cos\theta = \pm 1$ and have small P_{Tdm} .

Invariant Mass and Recoil Mass, M_{inv} and M_{recoil}: The di-muon invariant Mass is very close to be the Z mass, and the recoiling mass is close to the Higgs mass. These are very important variables because it is very unlikely that combinations of background processes fulfill both conditions simultaneously. These are also useful in suppression of background events of type $e^+e^- \rightarrow \mu^+\mu^-$ which are undergoing Final State Radiation. Figures 5.5 and 5.6 show the distributions of $\mu^+\mu^-$ invariant mass and recoil mass for the signal and backgrounds.

Cosine of the Z production angle, $cos\theta$: The Higgs-strahlung process is an annihilation or s channel process, and its cross section has no angular dependency. Background processes that are exchange or t channel process for example, $e^+e^- \rightarrow ZZ$, diverges at $\theta \rightarrow 0$ which is the very forward region of the detector. Also, the $cos\theta$ and P_{Tdm} are correlated by the formula, $cos\theta = \sqrt{1 - \frac{P_{Tdm}^2}{|TotalP|^2}}$, so processes which have softer P_{Tdm} diverge at $\theta \rightarrow 0$, and processes for which P_{Tdm} is uniform, $cos\theta$ is uniform as well. Figure 5.7 shows the distributions of $\mu^+\mu^-$ polar angle for the signal and backgrounds.

Muon momentum P_{μ^+,μ^-} : Not very correlated to the Z recoil mass, correlation coefficient = -0.1719. However, for the signal process the minimum and maximum muon momentum are 24 GeV and 86 GeV, respectively. We will not apply any cut tighter than this. Selection between 24 and 86 GeV. Figure 5.8 shows the distributions of muon momentum for the signal and backgrounds.

Visible Energy, E_{vis}: With an invisible Higgs in the signal events, the visible energy and visible mass are close to the Z mass. The SM two fermion and four fermion background processes carry large visible energy conversely. Figure 5.9 shows the distributions of visible energy for the signal and backgrounds.

Cosine of muon decay helicity angle, $cos\theta_{hel}$: This variable is useful for the suppression backgrounds from ZZ leptonic decays only. In the reaction, $e^+e^- \rightarrow ZH \rightarrow (\mu^+\mu^-)(H \rightarrow Inv)$ the helicity angle is the angle between the daughter, μ^+ and grandparent, e^+e^- in the parent Z's rest frame. Since the Z has spin one, the distribution of $cos\theta_{hel}$ is quadratic. Figure 5.10 shows the distributions of cosine of muon helicity angle for the signal and backgrounds.

Figure 5.11 shows the kinematic distributions of the $e^+e^- \rightarrow ZH \rightarrow (Z \rightarrow \mu^+\mu^-)(H \rightarrow Visible)$ background process. In the last three graphs 5.12, 5.13 and 5.14 correlation between the $\mu^+\mu^-$ momentum and their recoil mass, correlation between the μ momentum and the $\mu^+\mu^-$ recoil mass and correlation between the $\mu^+\mu^-$ polar and the helicity angle are shown, respectively.

5.6 FIT OF THE Z PEAK

Z mass peak follows a Breit-Wigner shape at the generator level. When detector resolutions introduce additional uncertainties, that is modelled with a "Gaussian". Thus a Breit-Wigner (for the inherent shape) convoluted with a gaussian (to describe the detector effects), is an option for fit function. The fit result is shown in the figure 5.15.

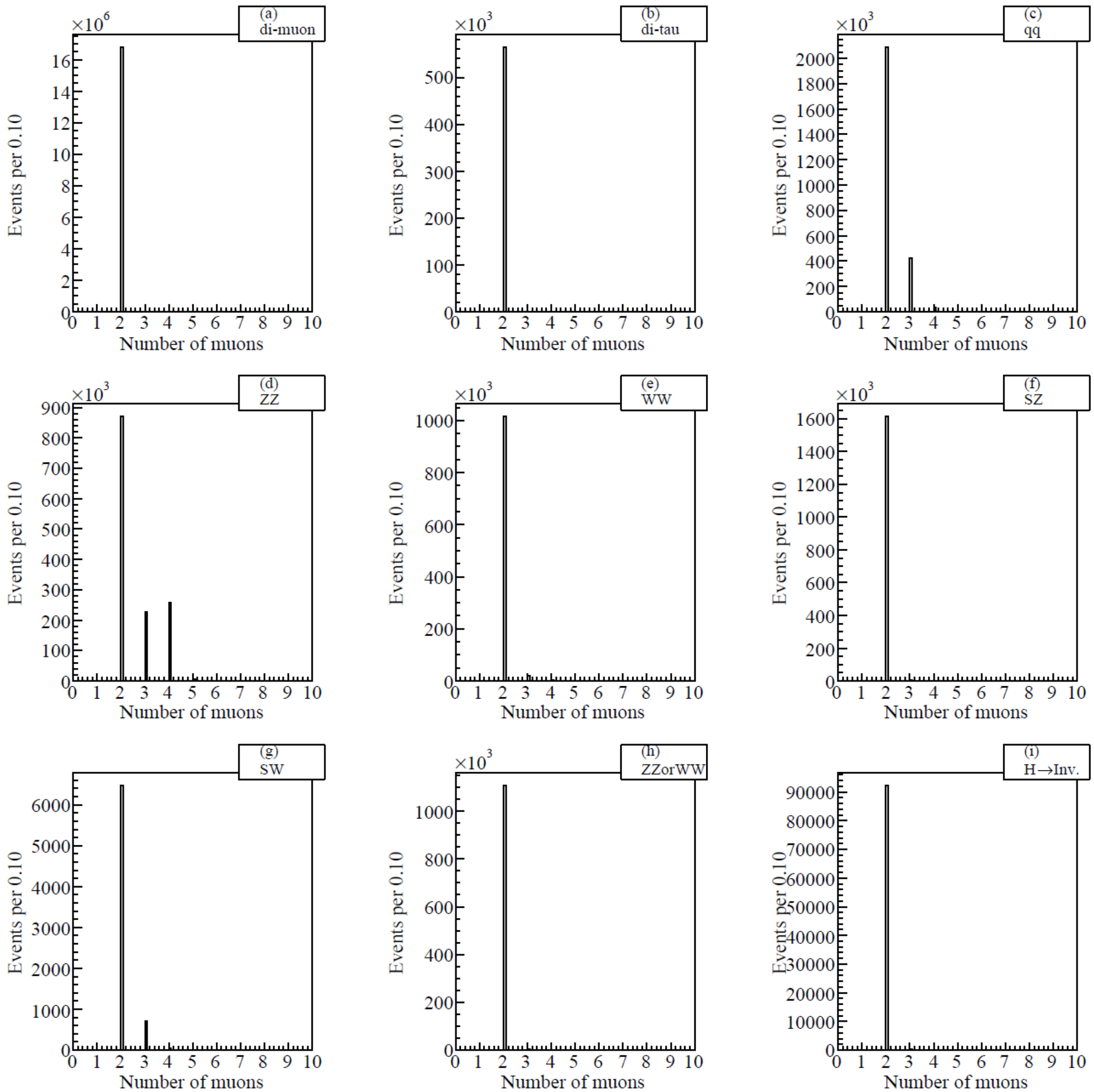

Figure 5.1. Number of muons for the backgrounds, figures (a)-(h) and the signal $e^+e^- \to ZH \to (Z \to \mu^+\mu^-)(H \to Inv)$, fig. (i).

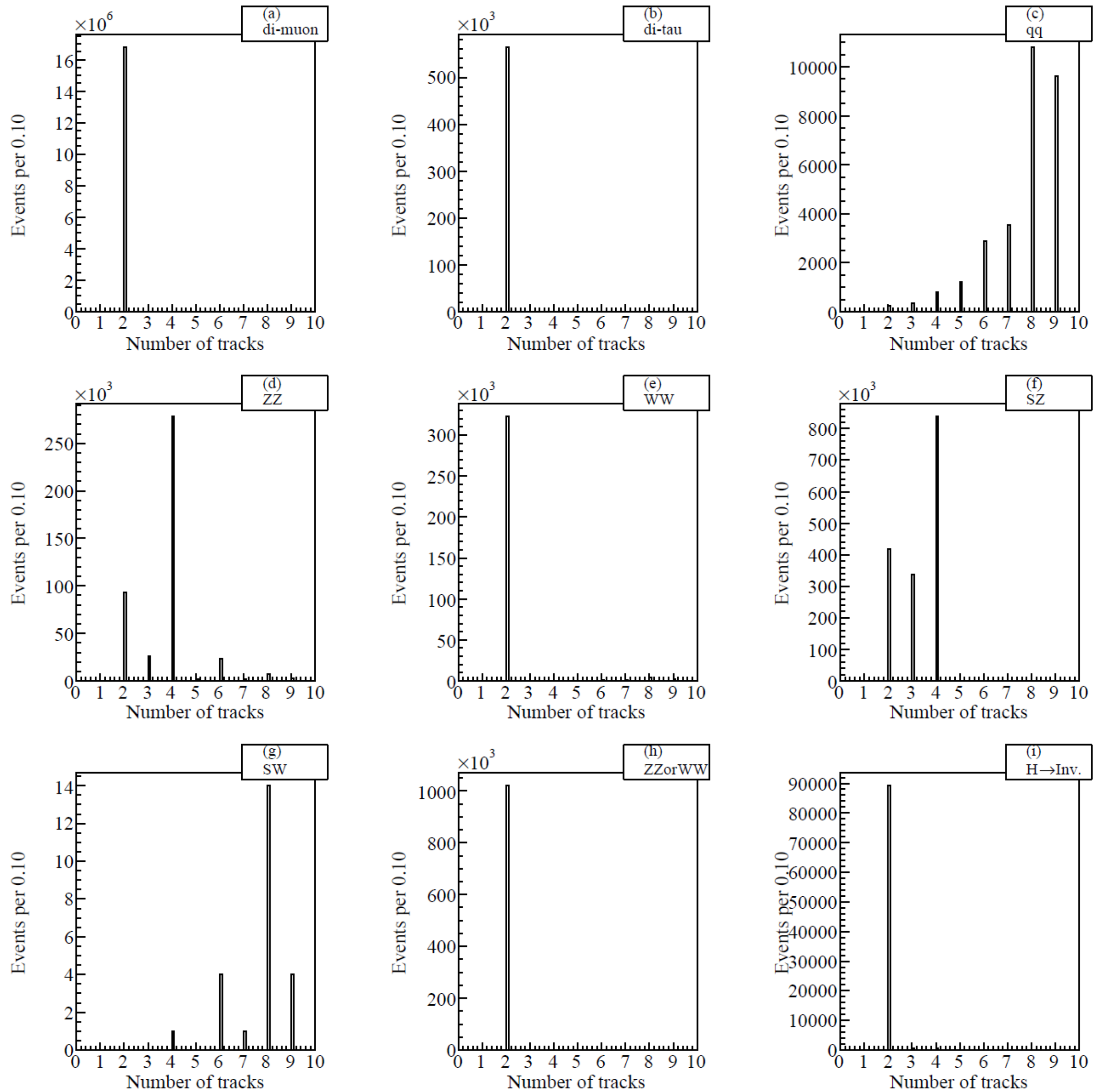

Figure 5.2. Number of tracks for the backgrounds, figures (a)-(h) and the signal $e^+e^- \to ZH \to (Z \to \mu^+\mu^-)(H \to Inv)$, fig. (i).

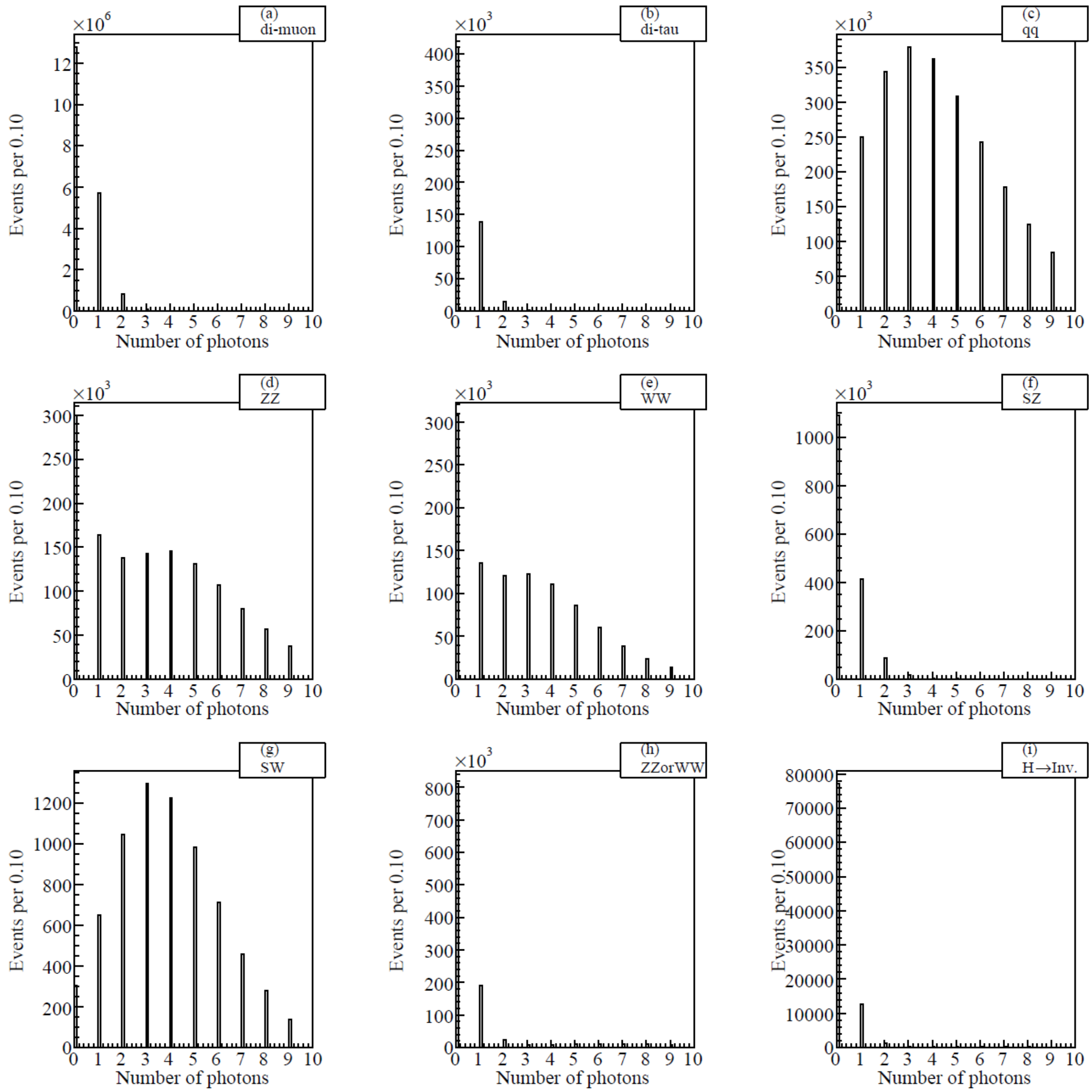

Figure 5.3. Number of photons for the backgrounds, figures (a)-(h) and the signal $e^+e^- \rightarrow ZH \rightarrow (Z \rightarrow \mu^+\mu^-)(H \rightarrow Inv)$, fig. (i).

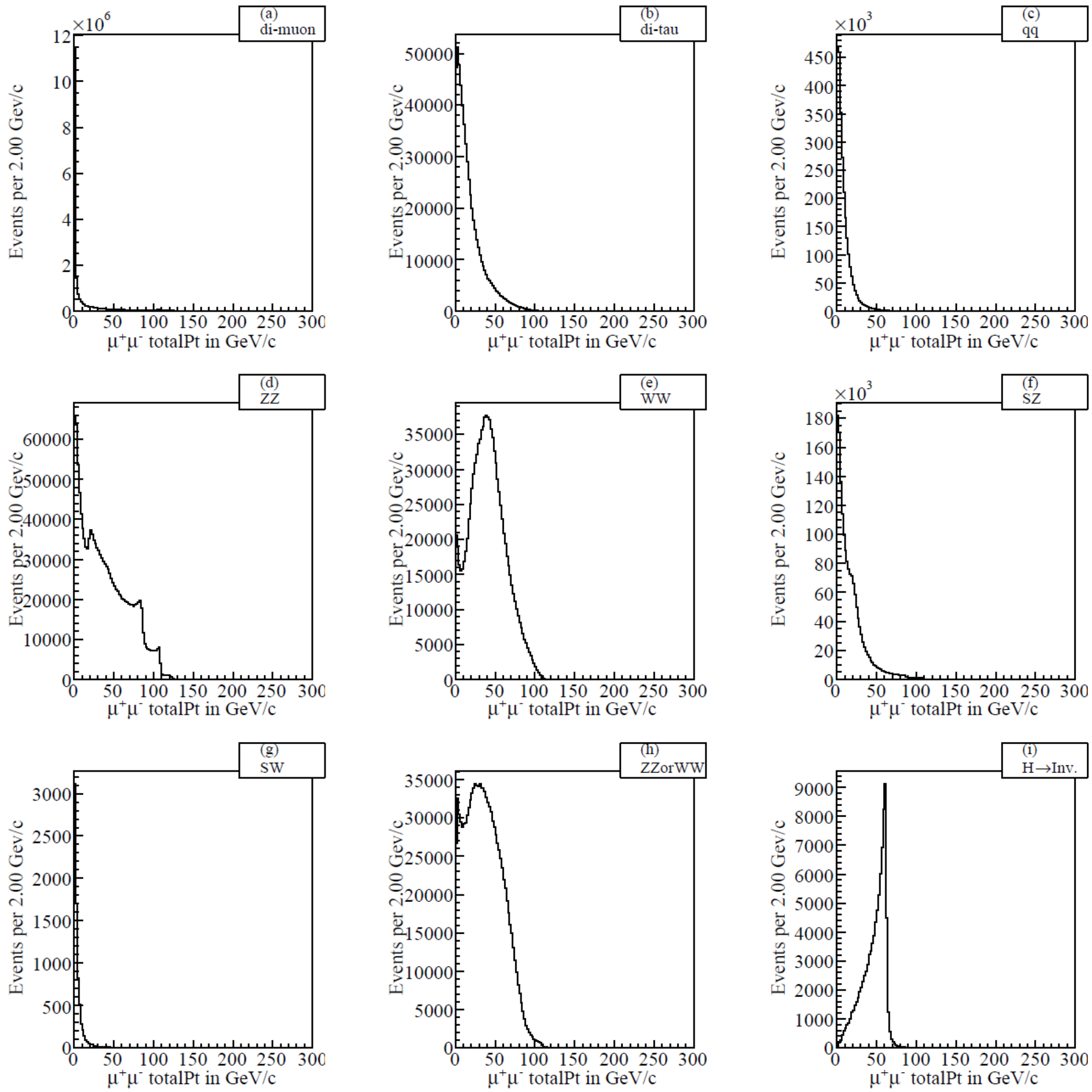

Figure 5.4. Total Transverse Momentum of the $\mu^+\mu^-$ for the backgrounds, figures (a)-(h) and the signal $e^+e^- \to ZH \to (Z \to \mu^+\mu^-)(H \to Inv)$, fig. (i).

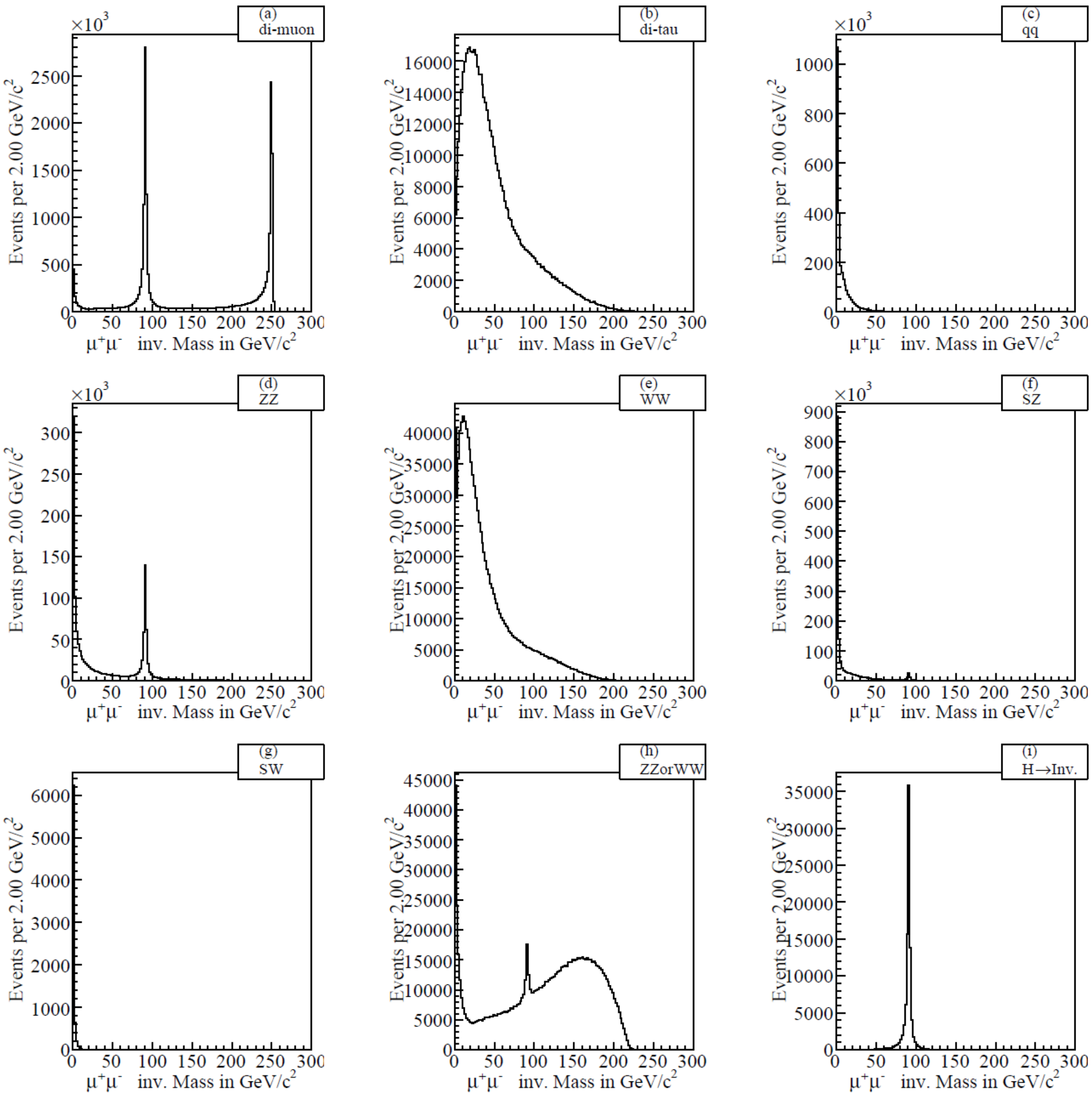

Figure 5.5. $\mu^+\mu^-$ invariant mass for the backgrounds, figures (a)-(h) and the signal $e^+e^- \to ZH \to (Z \to \mu^+\mu^-)(H \to Inv)$, fig. (i).

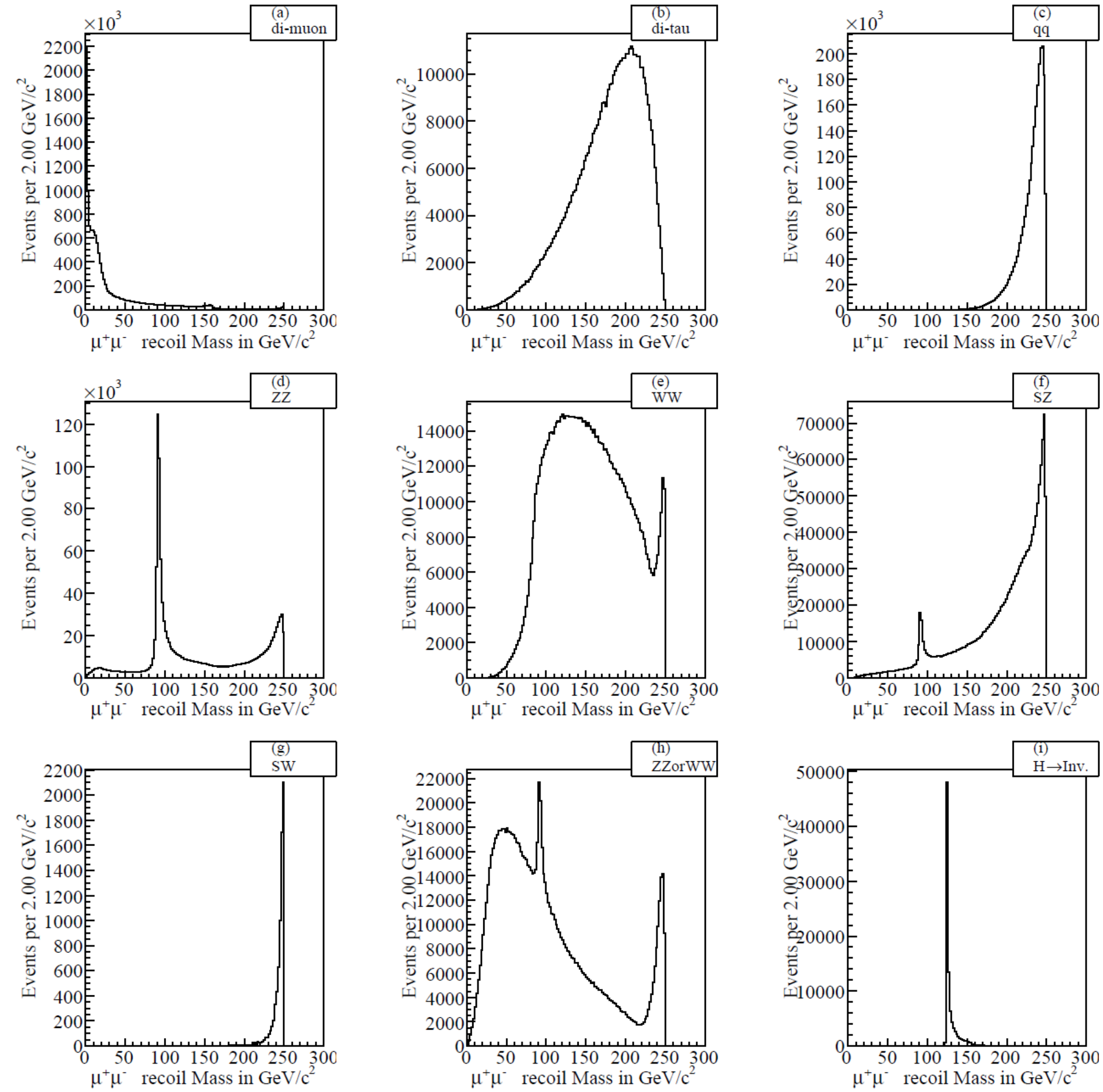

Figure 5.6. $\mu^+\mu^-$ recoil mass for the backgrounds, figures (a)-(h) and the signal $e^+e^- \rightarrow ZH \rightarrow (Z \rightarrow \mu^+\mu^-)(H \rightarrow Inv)$, fig. (i).

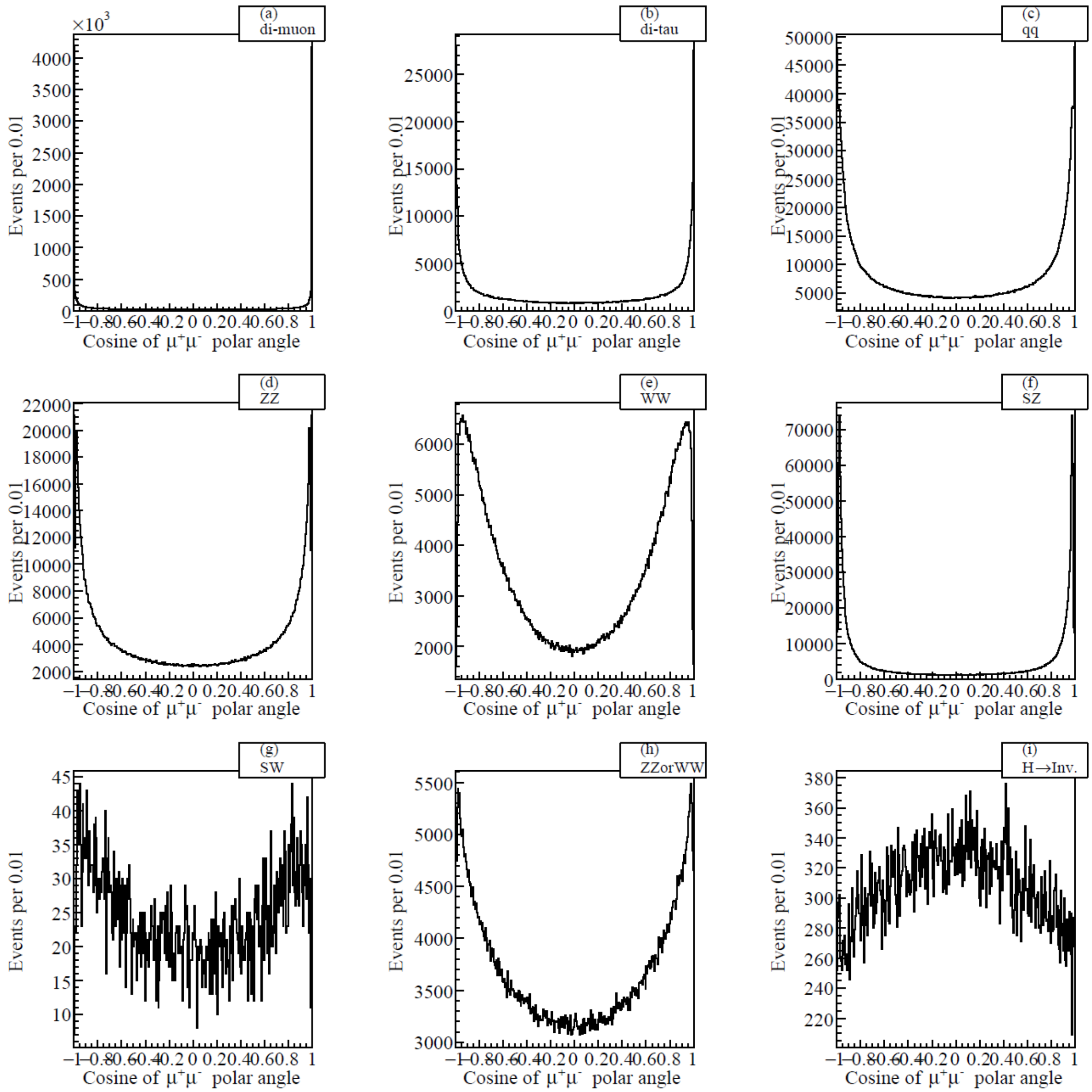

Figure 5.7. $\mu^+\mu^-$ polar angle for the backgrounds, figures (a)-(h) and the signal $e^+e^- \to ZH \to (Z \to \mu^+\mu^-)(H \to Inv)$, fig. (i).

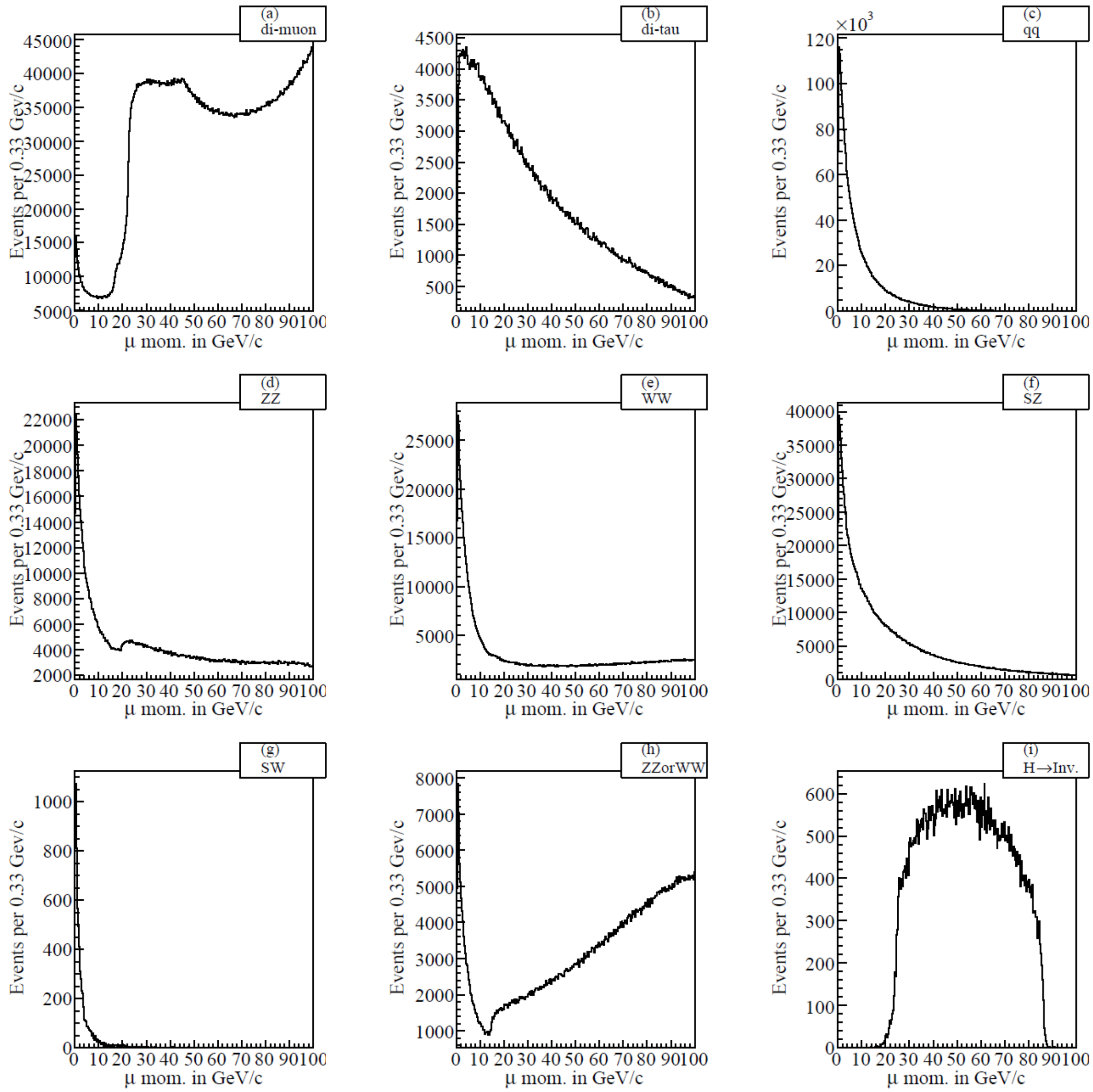

Figure 5.8. Muon momentum for the backgrounds, figures (a)-(h) and the signal $e^+e^- \to ZH \to (Z \to \mu^+\mu^-)(H \to Inv)$, fig. (i).

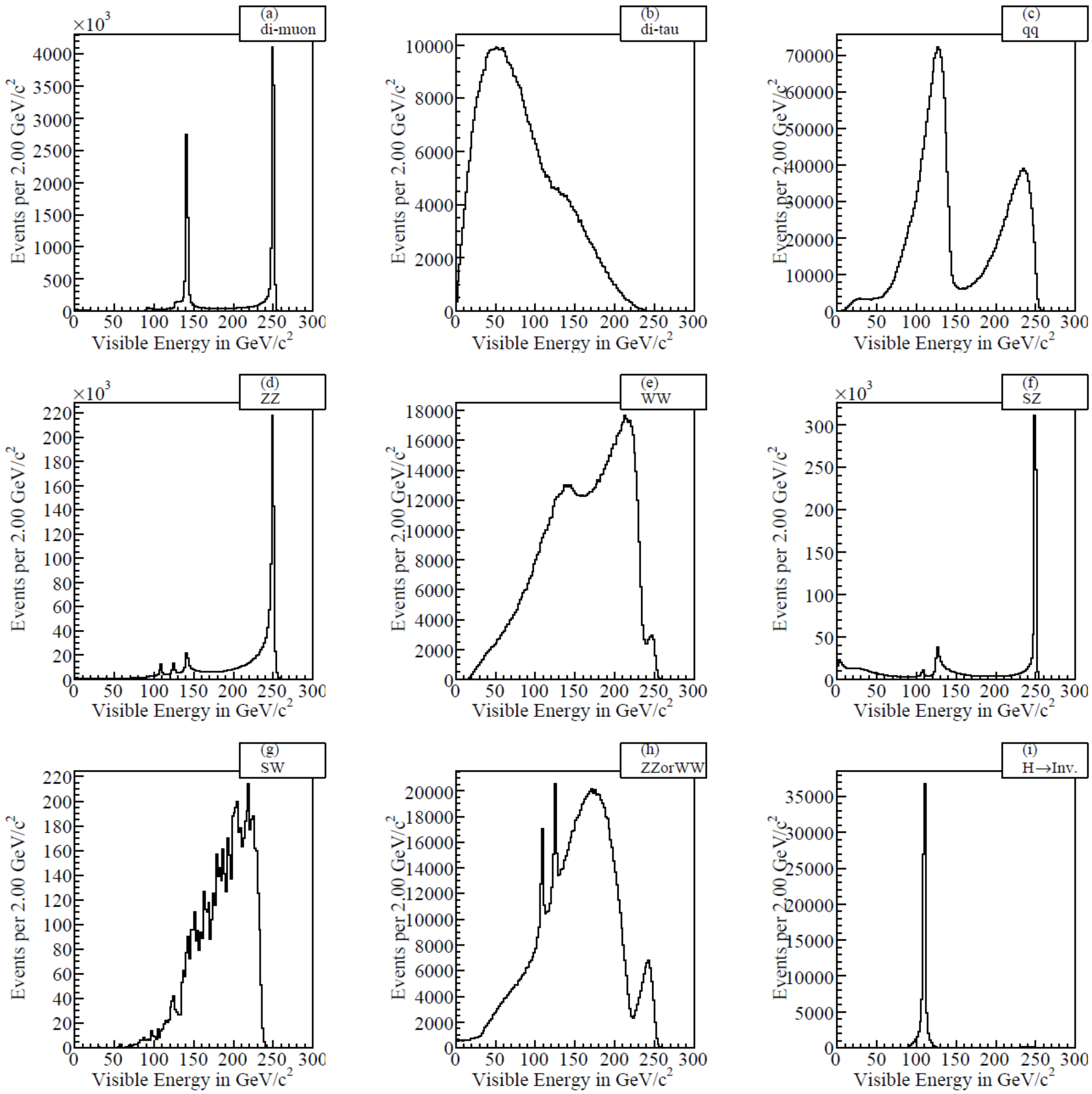

Figure 5.9. Visible energy for the backgrounds, figures (a)-(h) and the signal $e^+e^- \to ZH \to (Z \to \mu^+\mu^-)(H \to Inv)$, fig. (i).

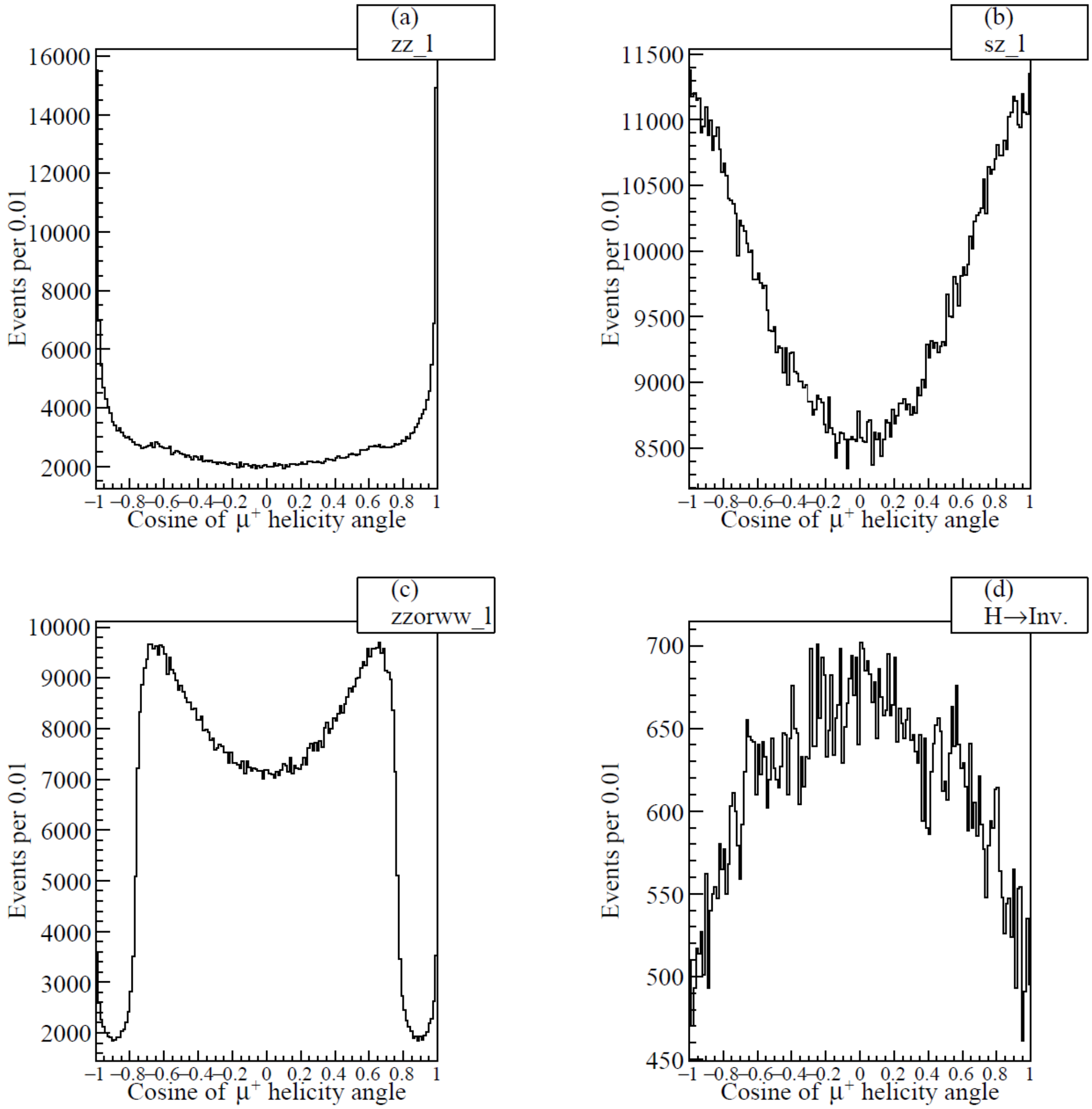

Figure 5.10. Cosine helicity angle for the backgrounds, figures (a)-(c) and the signal $e^+e^- \to ZH \to (Z \to \mu^+\mu^-)(H \to Inv)$, fig. (d).

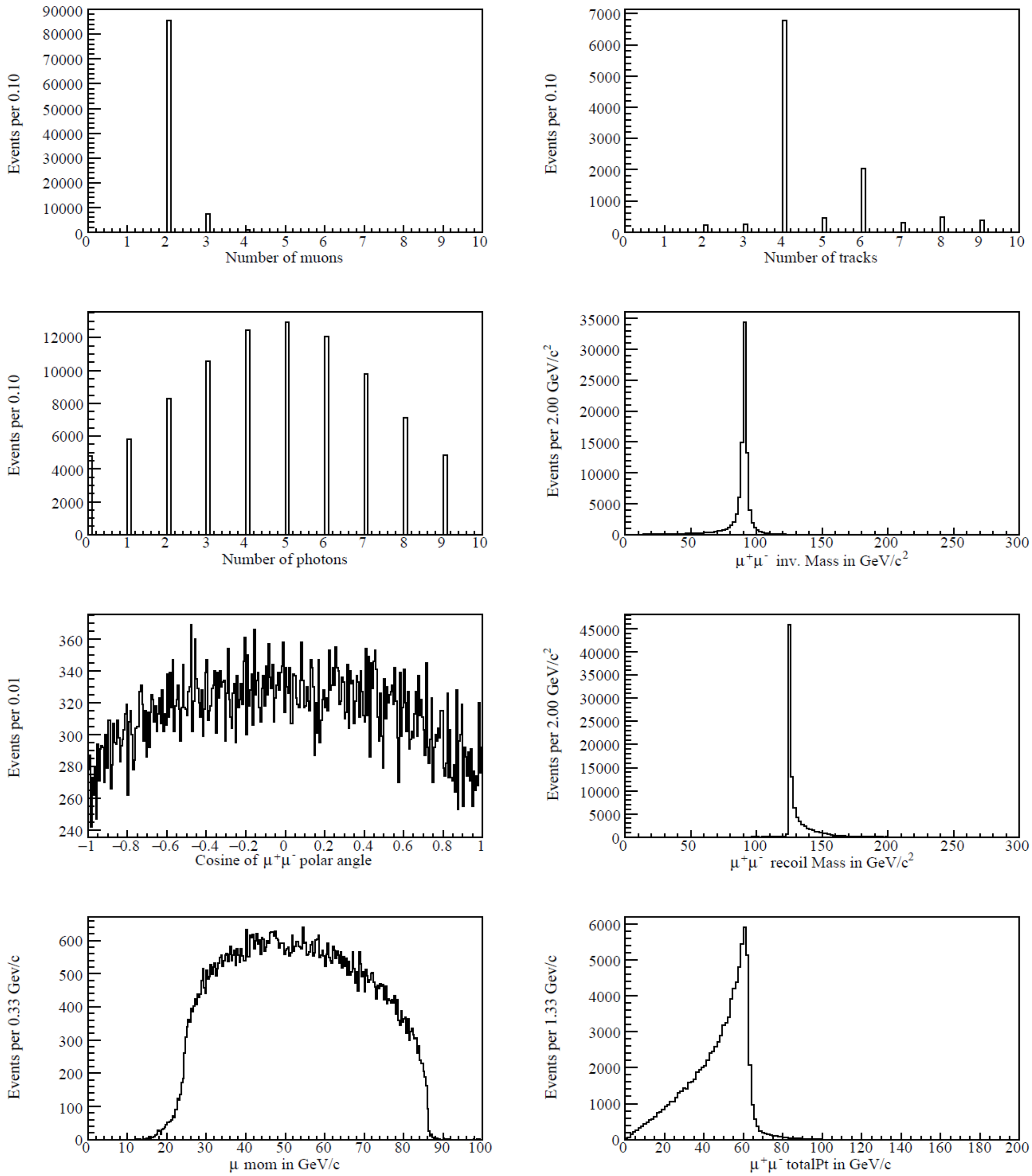

Figure 5.11. Kinematic distributions of the $e^+e^- \to ZH \to (Z \to \mu^+\mu^-)(H \to Visible)$.

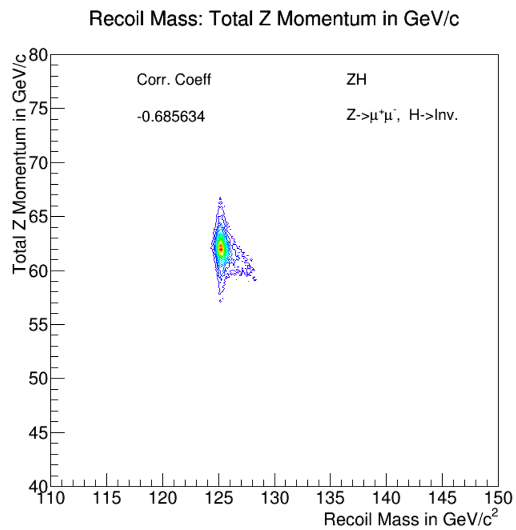

Figure 5.12. Correlation between $\mu^+\mu^-$ momentum and recoil mass for the signal $e^+e^- \rightarrow ZH \rightarrow (Z \rightarrow \mu^+\mu^-)(H \rightarrow Inv)$.

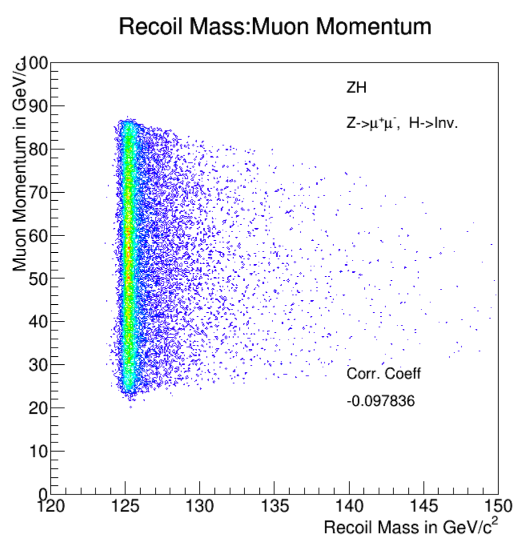

Figure 5.13. Correlation between μ momentum and $\mu^+\mu^-$ recoil mass for the signal $e^+e^- \rightarrow ZH \rightarrow (Z \rightarrow \mu^+\mu^-)(H \rightarrow Inv)$.

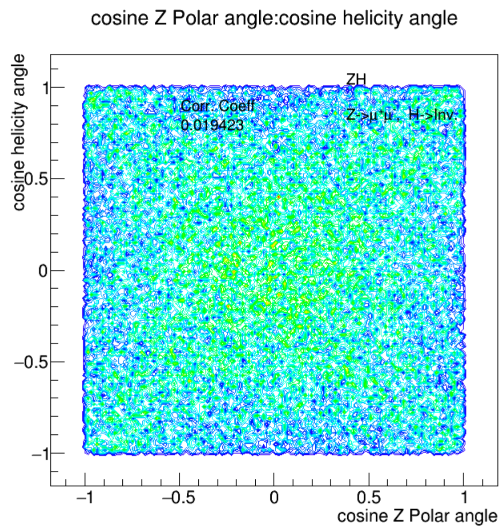

Figure 5.14. Correlation between $\mu^+\mu^-$ polar and helicity angle for the signal $e^+e^- \to ZH \to (Z \to \mu^+\mu^-)(H \to Inv)$.

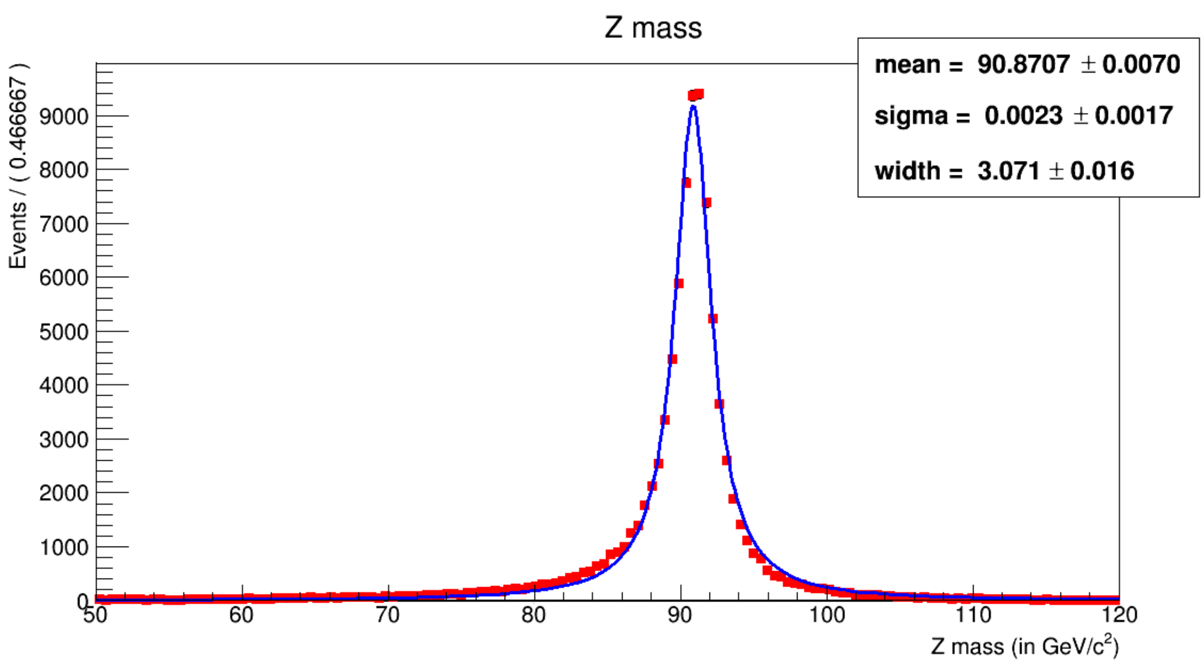

Figure 5.15. Showing the Gaussian convulated with Breit Wigner fit for the Z mass.

CHAPTER 6

CUT BASED ANALYSIS

6.1 INTRODUCTION

In this chapter we describe the cut based analysis. We describe the detection efficiency for $H \to \textit{invisible}$ signal, significance and statistical uncertainty on the Higgs signal and how they are calculated.

6.2 CUT BASED REJECTION AND OPTIMIZATION

We apply cuts, numerical limits on the kinematic and geometric variables and detector response. The selection consists of a set of cuts, and is presented by tables and plots that are referred to as “Cut-Flows” in this dissertation.

We apply cuts on these variables. The selection procedure is laid out as a sequence of cuts [27]. In order to have the largest possible signal event content in the $H \to$ invisible sample while keeping a low background level a score function is defined. If N is the number of events selected, that is the sum of S and B, the number of signal and background events respectively, so that our best estimate of S is,

$$S = N - B \tag{6.1}$$

The uncertainty in the signal is given by,

$$\sigma^2(S) = \sigma^2(N) + \sigma^2(B) \tag{6.2}$$

Considering Poisson fluctuation for N, $\sigma^2(N) = N$ and uncertainty in average estimation of B negligible for large Monte Carlo sample,

$$\sigma^2(S) \cong N; \tag{6.3}$$

We introduce a score function,

$$\frac{S}{\sigma(S)} = \frac{S}{\sqrt{N}} = \frac{S}{\sqrt{S+B}} \tag{6.4}$$

This quantity in equation 6.4 gives us the number of standard deviations away from 0 of the signal, a quantity that should be as large as possible, so that it is a good score function for our purpose, a function that we will maximize [27].

6.3 DETECTION EFFICIENCY

The fraction of produced signal (Higgs) events passing a set of cuts is defined as the efficiency (ϵ) of the cuts [27]. The efficiency is used in the calculation of the branching fraction and in the calculation of the upper limit, of the Higgs signal. Efficiency is calculated through the Monte Carlo study. From the total number of Monte Carlo events generated, the percentage of events selected by the cuts gives the efficiency. We have made the following selections for the above described variables:

- number of muons,$(nMuon) <= 3$,
- number of tracks, $(ntrks) <= 3$,
- number of photons,$(nGamma) <= 1$,
- di-muon invariant mass, $(RMass12)$, lies between 85 GeV and 95 GeV,
- total transverse momentum of the di-muon, $(TotalPt)$ is between 40 GeV and 65 GeV,
- cosine of di-muon polar angle, $(Costheta)$ is between (-0.8, +0.8) and
- visible energy, $(VisEn)$ is between 100 GeV and 120 GeV.

6.4 SENSITIVITY

The sensitivity which is the uncertainty on the signal cross section [46, 47, 48, 49, 50, 51].

$$\delta\sigma = \frac{\sqrt{N_S + N_B}}{N_S} = BR(H \to inv.)\frac{\sigma_{BSM}}{\sigma_{SM}} \tag{6.5}$$

where σ_{BSM} stands for the Beyond the Standard Model cross-section and σ_{SM} stands for the Standard Model cross-section in the e^+e^- collider in the best possible way. In the case for which the Higgs boson decays entirely to the invisible mode, sensitivity is the ratio between the non-Standard Model cross-section and the Standard Model cross-section. The goal is to find this ratio with 5 ab^{-1} of CEPC fully simulated MC data with Higgs mass of 125 GeV. The limit on the sensitivity for the invisibly decaying Higgs will also be calculated. The statistical uncertainty is given by $\sqrt{N_S + N_B}$ [46, 47]. $\frac{\sqrt{N_S+N_B}}{N_S}$ is the uncertainty on the signal cross-section.

Tables 6.1 and 6.2 list the cuts used; the events passing the cuts; the efficiency for the signal and survival rates for the background. The $H \to Invisible$ efficiency is $(56 \pm 0.22)\%$. The background survival rate is estimated to be $(0.01 \pm 0.0002)\%$ for the combined SM backgrounds used in this work. If the initial number of events is N_0 and the final number after the selection is N_f the statistical uncertainty is given by,

$$Stat.Unc. = \frac{\sqrt{N_f}}{N_0} \tag{6.6}$$

A fit is performed for the signal (Crystal Ball function) and background (Polynomial). The selected events are shown in the Figures 6.2. A simple Crystal Ball function does not adequately describe the Higgs signal in terms of the recoil mass against the Z boson. So for the signal and background, a Piece-Wise function that match the histogram of the Higgs signal in Z recoil mass distribution, referred to as HistPdf is used. From the fit the number of signal and background events are obtained. Figures 6.3, 6.4, 6.5 show the fit results. The

Table 6.1. Cut Flow showing the background events and the signal events after each subsequent cut has been applied. The background corresponds to $1 \times 5ab^{-1}$ and the $H \rightarrow Visible$ (no-invi) and $H \rightarrow Invisible$ correspond to $2.79 \times 5ab^{-1}$ of the data.

Process	di-muon	di-tau	diquark	ZZ	WW	SZ	SW	ZZorWW	no-invi	h-invi
Number of entries	1.94E+07	564151	2.88E+06	1.36E+06	1.04E+06	1.62E+06	7221	1.11E+06	94241	92433
$nMuon <= 3$	1.94E+07	564151	2.84E+06	1.10E+06	1.04E+06	1.62E+06	7186	1.11E+06	93242	92421
$ntrks <= 3$	1.94E+07	564135	676	118854	322691	756403	0	1.02E+06	471	89919
$nGamma <= 1$	1.85E+07	548278	606	114778	317772	734576	0	999471	152	88865
$-0.8 < Cos\theta < 0.8$	5.68E+06	257408	74	44674	219584	252897	0	742271	121	72889
$85 < M_{inv} < 95$	549645	13284	0	13475	16601	17616	0	39878	88	60335
$40 < TotalPt < 65$	34475	3027	0	4873	8583	6802	0	15381	79	53513
$100 < E_{vis} < 112$	0	1730	0	648	4284	1768	0	4951	3	51580

Table 6.2. Cut Flow showing inverse background rejection and the signal efficiency after each subsequent cut has been applied.

Process	di-muon	di-tau	diquark	ZZ	WW	SZ	SW	ZZorWW	no-invi	h-invi
$nMuon <= 3$	1	1	0.98625	0.80627	0.99824	0.99985	0.99515	0.99967	0.9894	0.99987
$ntrks <= 3$	1	0.99997	0.00024	0.08732	0.31101	0.46751	0	0.91879	0.005	0.9728
$nGamma <= 1$	0.95326	0.97186	0.00021	0.08432	0.30627	0.45402	0	0.89999	0.00161	0.9614
$-0.8 < Cos\theta < 0.8$	0.29275	0.45628	0.00003	0.03282	0.21163	0.15631	0	0.66839	0.00128	0.78856
$85 < M_{inv} < 95$	0.02835	0.02355	0	0.0099	0.016	0.01089	0	0.03591	0.00093	0.65274
$40 < TotalPt < 65$	0.00178	0.00537	0	0.00358	0.00827	0.0042	0	0.01385	0.00084	0.57894
$100 < E_{vis} < 112$	0	0.00307	0	0.00048	0.00413	0.00109	0	0.00446	0.00003	0.55803

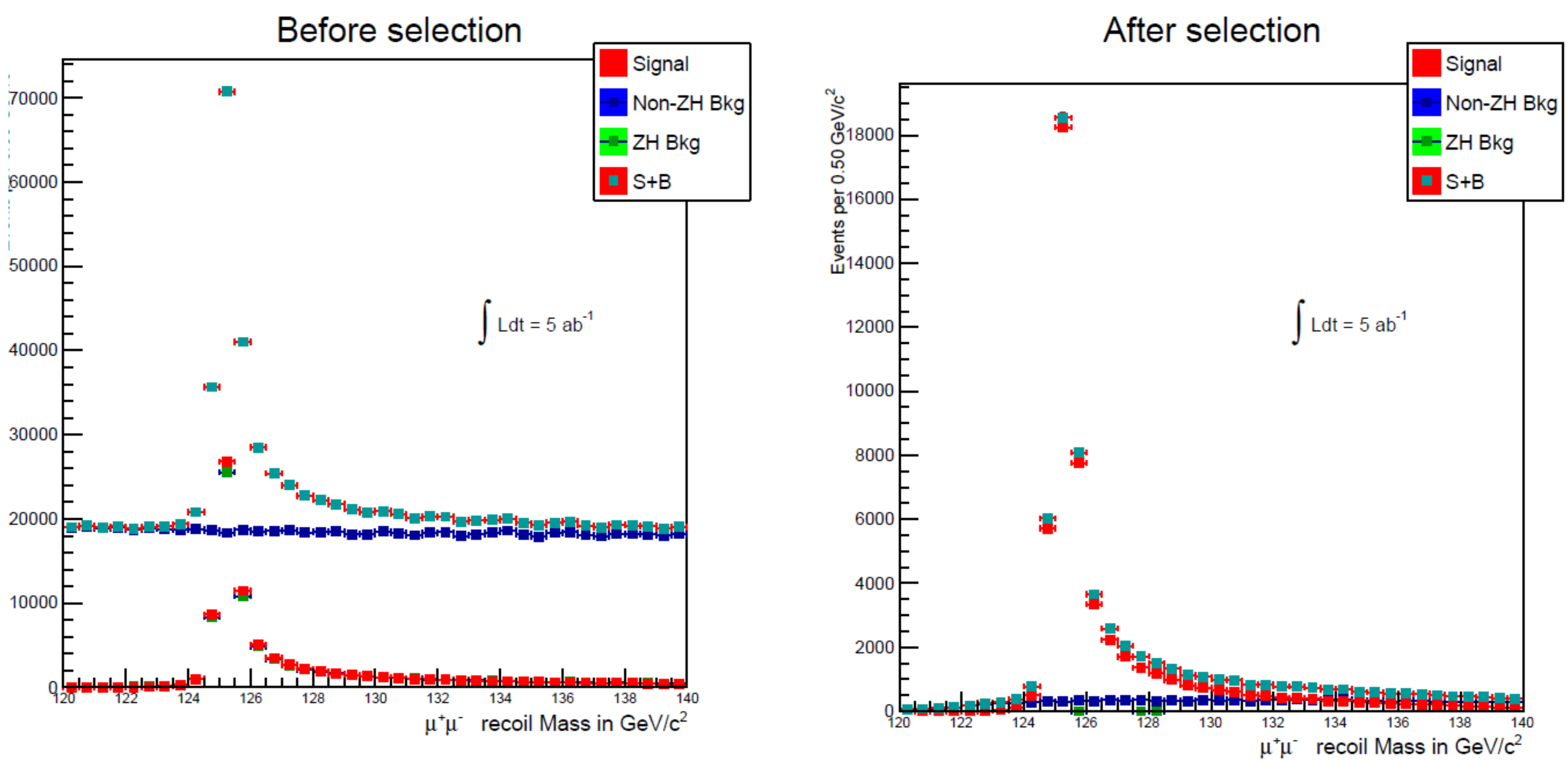

Figure 6.1. Recoil mass spectrum before and after the cut based selection.

Table 6.3. Uncertainty on the branching ratio for $BR(H \to Invisible)$=0%, 0.1%, 1%, 5% and 10%.

Input BR (%)	Nsig (without fit)	Nbkg (without fit)	Nsig (with fit)	Nbkg (with fit)	$BR(H \to$Inv.) $\pm\delta_{BR}$(%)
0	0	13239	0^{+44}_{-0}	13238 ± 123	$0.00^{+0.23}_{-0.00}$
0.1	18	13239	16^{+45}_{-16}	13242 ± 124	$0.08^{+0.23}_{-0.08}$
1	184	13239	191 ± 48	13234 ± 124	1.00 ± 0.25
5	924	13239	879 ± 60	13286 ± 127	4.62 ± 0.32
10	1848	13239	1764 ± 71	13324 ± 129	9.26 ± 0.37

Table 6.3 shows the number of signal and background event with and without the fit. The BR and its uncertainty are obtained using the formula given by,

$$BR = \frac{N_{fit}}{N_{ZH} \times BR(Z \to \mu^+\mu^-) \times \varepsilon_{sig}}, \tag{6.7}$$

where N_{fit} is the number of signal events obtained from the fit, N_{ZH} is the total number of ZH events obtained with the integrated luminosity of 5 ab^{-1} and is equal to 10^6. $BR(Z \to \mu^+\mu^-)$ the Z to dimuon branching ratio is (3.4±0.007)%, and ε_{sig} is the signal efficiency (56±0.22)%.

$$\delta_{BR} = \frac{\Delta N_{fit}}{N_{ZH} \times BR(Z \to \mu^+\mu^-) \times \varepsilon_{sig}}, \tag{6.8}$$

where ΔN_{fit} is the error on the number of signal events obtained from the fit.

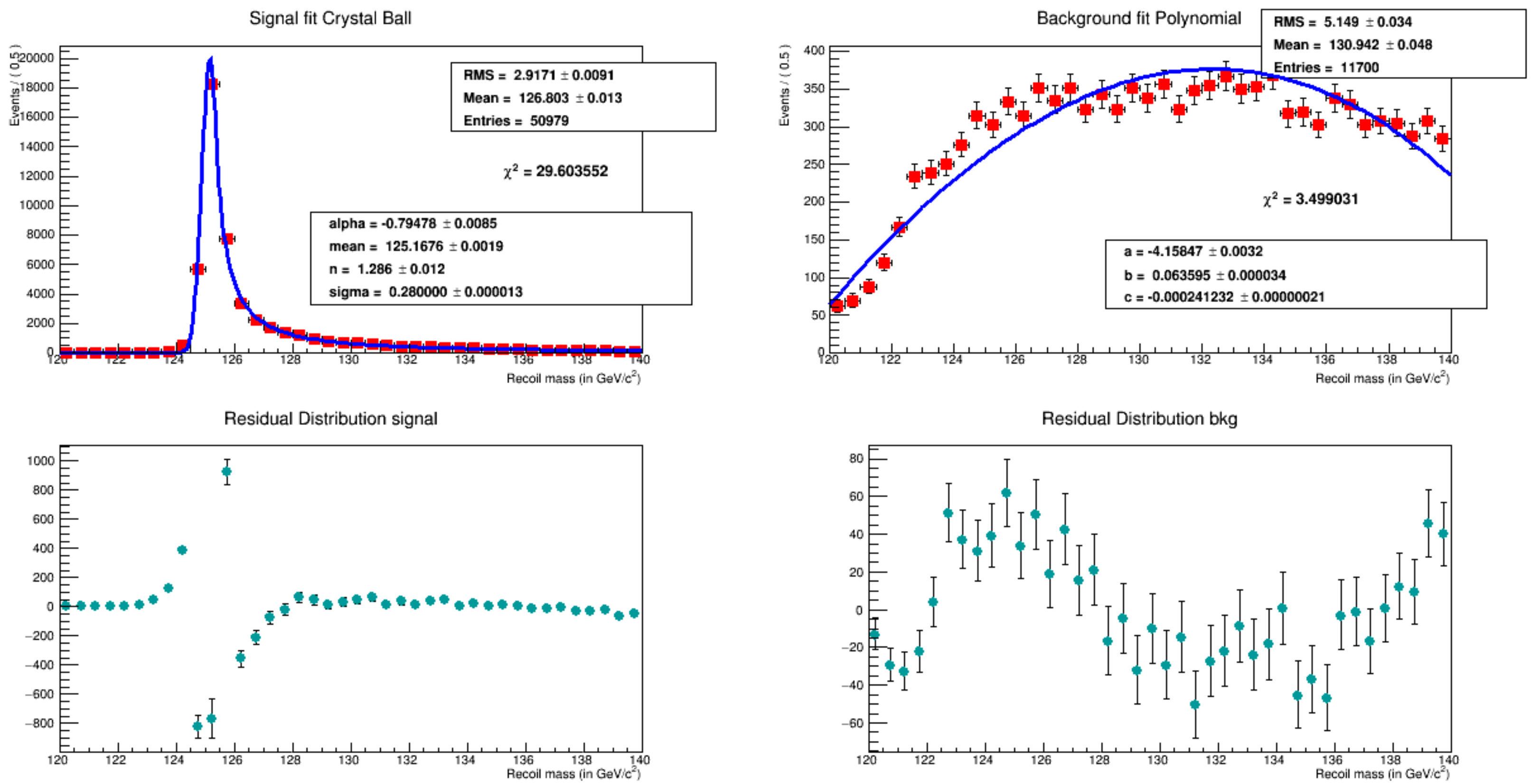

Figure 6.2. Fit to the recoil mass spectrum for signal and composite background.

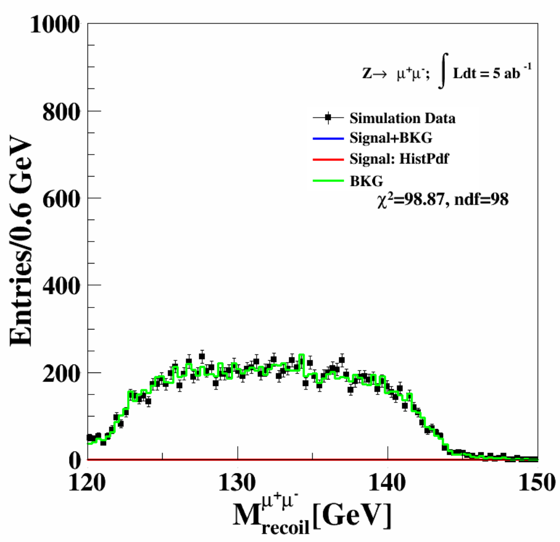

(a) BR($H \to$ invisible)=0%.

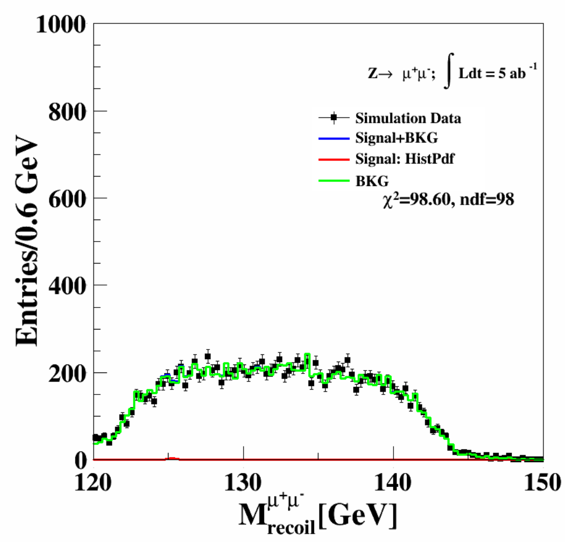

(b) BR($H \to$ invisible)=0.1%.

Figure 6.3. Fit result for BR($H \to$ invisible)=0% and 0.1%.

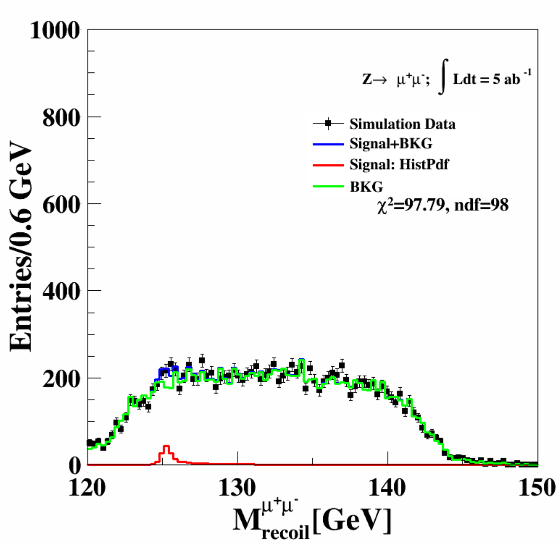

(a) BR($H \to$ invisible)=1%.

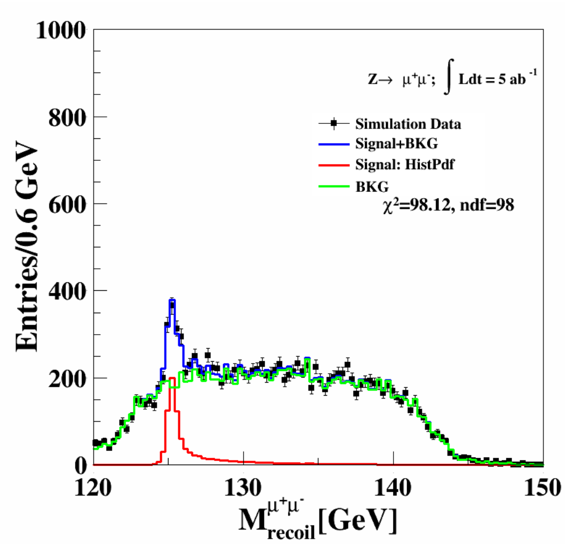

(b) BR($H \to$ invisible)=5%.

Figure 6.4. Fit result for BR($H \to$ invisible)=1% and 5%.

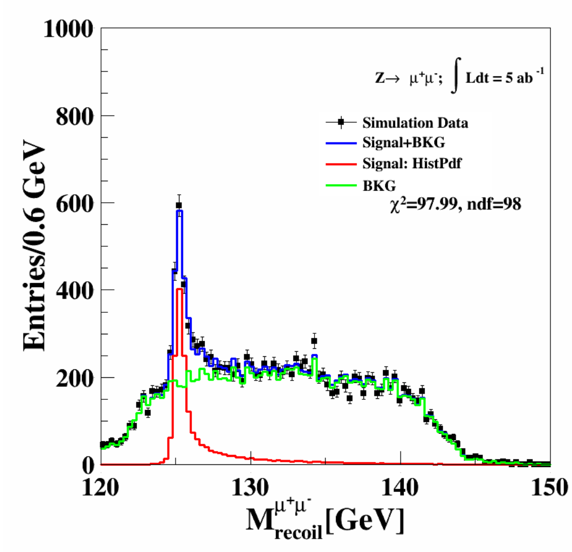

(a) BR($H \rightarrow$ invisible)=10%.

Figure 6.5. Fit result for BR($H \rightarrow$ invisible)=10%.

CHAPTER 7

MULTIVARIATE ANALYSIS WITH TMVA

7.1 INTRODUCTION

This chapter describes the details of the TMVA (Toolkit for Multivriate Analysis).

7.2 TMVA

TMVA serves to the demands of the high energy physics applications by providing a ROOT integrated machine learning platform for the processing and parallel evaluation of multivariate classification and regression techniques [52]. Classification is categorization and is used in the separation of signal from background processes. Regression finds the value of the parameters of a function, in terms of input variables which is later used for the prediction of the response.

7.3 EVENT CLASSIFICATION AND MULTIVARIATE ANALYSIS

We restrict to just two types or classes of data in our sample the signal and the background. Let $x_1, x_2, ..., x_D$ be a set of discriminating variables, we find the decision boundary to select events of the type signal. The boundaries may be rectangular cut or linear, in which case they are low variance, high bias or non-linear which is high variance and small bias class boundary [52].

Multivariate analysis is finding a mapping of D dimensional feature space to a one dimensional output $y(x)$, where x represents the set of input variables $x_1, x_2, ...x_D$. The variable $y(x)$ is called the discriminating function. The normalized distribution of $y(x)$ give the probability density function, PDF, for the signal and background. If f_s and f_b are the fraction of signal and background events in the sample then $\frac{f_s PDF_s}{f_s PDF_s + f_B PDF_B}$, is the probability of an event being a signal type.

7.4 EMPLOYING TMVA FOR MULTIVARIATE ANALYSIS

The TMVA involves three stages of analysis. I) Pre-analysis, II) the training and III) the application. The pre-analysis stage consists of preparing the ROOT files containing a true signal sample for event classification. A set of baseline selection cuts are made on these files to reduce the background to a manageable level. Decision needs to be made on the analysis type which can be either classification or regression type. In our case, it is classification. Discriminating variables have to be determined and a minimum of two input variables is required. The TMVA method used for the analysis is required to be selected from all the options provided by the toolkit [52]. The training can be done inclusively with the sum of all the backgrounds as a combined background and a signal sample, or exclusively with just one background type at a time and a signal. The TMVA method is decided, in our case it is the Boosted Decision Tree Gradient (BDTG) technique [52]. Well motivated input variables with small correlation should be used. Training with many variables is time consuming and highly correlated or non-discriminating variables lead to failure in the achievement of a good result by the method. Some methods give a ranking of the variables which depend on the method used. They may not be optimal. The optimal selection on the MVA output is the selection for which the significance, $\frac{S}{\sqrt{S+B}}$ is maximum. S and B are the number of signal and background events, respectively.

7.5 BOOSTED DECISION TREE

Decision Trees: We discuss the BDT, which is one of the methods implemented in TMVA. To choose and determine the events out of the sample as either signal or background successive decision nodes are used. Each node uses only a single discriminating variable to judge if the event is signal-like or background-like. A structure that looks like a tree is formed with "containers" at the end (leave nodes).

In Boosted Decision Trees, a set of decision trees (ensemble) are derived from the same sample. Figure 7.1 illustrates a decision tree.

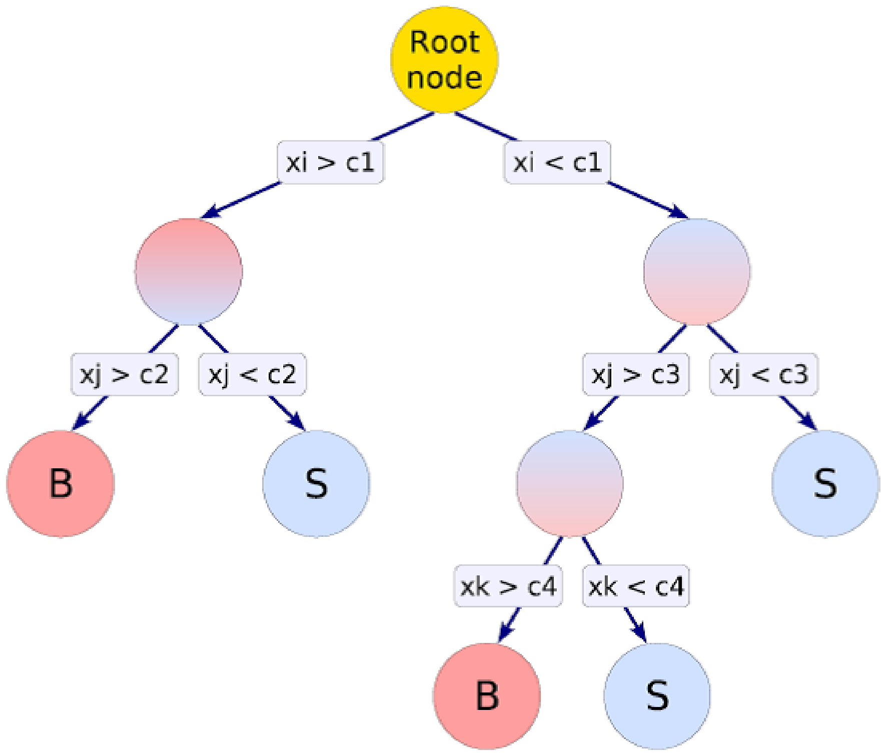

Figure 7.1. Illustrating the decision tree.

Training is the process that defines the "cut criteria" for each node of a decision tree. The training starts with the root node. Once a certain node reaches either a minimum number of events, or a minimum or maximum signal purity the division concludes. Based on how many signal or background events from the training sample the leave nodes contain they are called "signal" or "background", respectively. Weights tell us which events are important to get rightly classified in the next iteration. The signal events from the training sample, that are wrongly classified i.e., they end up in a background node (contrariwise) are given a higher weight than events that are in the correct leave node. The outcome of which is a re-weighed training event sample, from which a new tree emerges. The boosting can be applied several times (typically 100-800 times), in my study it is 300, this generated a group of decision trees, the forest of trees [52].

A test event is fed through an individual decision tree that results in a classification of the event as either signal or background. This process is called **Testing**. A "likelihood" estimator is obtained based on how often an event is classified as signal or background when it is fed to the whole set of decision trees consecutively. This estimator value is then used to select the events from an event sample, and the value of the cut on this estimator defines the purity and efficiency of the selection.

7.5.1 SPLITTING CRITERION: ENTROPY AND INFORMATION, GINI INDEX

Entropy is a measure of disorder or unpredictability of an event sample and depends on the probability of the outcomes of the events in the sample.
The entropy $H_{ent}(x)$ is given by

$$H_{ent}(x) = \Sigma p(x) \log(1/p(x)), \tag{7.1}$$

where x is one of the outcomes and p(x) is the probability of that outcome. The sum is over all the outcomes. There can be two outcomes, the signal or background. The more desirable the decision stump or selection criterion the higher the information gain. Similar to entropy is the gini index and is given by

$$H_{ent}(x) = \Sigma p(x)(1 - p(x)) \tag{7.2}$$

It measures how frequently a randomly selected element from the set would be wrongly classified if in the subset, it was randomly labeled according to the distribution of labels. By adding the probability $p(x)$ of an item with label x being chosen times the probability $1 - p(x)$ of a mistake in categorizing that item, gini impurity can be computed. When all cases in the node fall into a single target category, gini index is zero. Thus it measures the purity of the events in a particular node of a classification and regression tree (CART).

7.5.2 ADA BOOST AND GRADIENT BOOSTING

In a classication problem, misclassied events are multiplied by a common boost weight α. From the misclassication rate, error, of the previous tree, $\alpha = \frac{1-error}{error}$ the boost weight is derived.

Renormalization of the weights of the entire event sample makes the sum of weights remain constant. We define the result of an individual classier as $h(x)$, with (x being the tuple of input variables) encoded for signal and background as $h(x) = +1$ and 1, respectively. The boosted event classication $y_{boost}(x)$ is then given by,

$$y_{boost}(x) = \frac{1}{N_{ensemble}} \sum_{k}^{N_{ensemble}} \ln \alpha_k \cdot h_k(x) \tag{7.3}$$

where the sum is over all classiers in the ensemble. Background-like (signal-like) event is indicated by small (large) values for $y_{boost}(x)$. Equation represents the standard boosting algorithm.

AdaBoost [52] based on exponential loss, $L = e^{F(x)\cdot y}$, where $F(x)$ is the model response and y is the true value, is the most popular boosting method. In the presence of outliers or mislabelled data points, however, exponential loss lacks robustness. For this reason, in noisy settings, the performance of AdaBoost is expected to degrade.

The GradientBoost algorithm attempts to solve this problem by using a binomial log-likelihood loss $L(F, y) = \ln(1 + e^{-2F(x)\cdot y})$, which is more robust and does not give up on the good out-of-the-box performance of AdaBoost.

7.6 MULTIVARIATE ANALYSIS WITH BDT

The BDT method is used for the multivariate analysis of Higgs to invisible decays in this dissertation. The BDT are first trained with the MC samples. Higgs to four neutrino (invisible to CEPC detector) sample is used for the signal training and the total SM backgroud is used for background training. The event selection before the training has an influence on the training. This is studied first. A baseline event selection is used to which the BDT cut is added for different Higgs to invisible branching ratio scenarios which are 0%, 0.1%, 1%, 5% and 10%.

7.6.1 PRESELECTION OF EVENTS

The event selection influences the shape of the distribution of variables. After the event selection the background is enriched with signal-like events, and the background shape becomes more signal-like. Thus the seperation of signal from background becomes onerous. Therefore training is done with loose event selection inspired only by the triggers that have to be used. This is verified by the background rejection versus the signal efficiency graph called the "ROC" (Receiver Operating Curve) obtained after the training using two pre-selections, selection 1 and selection 2. The ROC is the best plot to estimate the discrimination power [52]. Figure 7.2 shows the background rejection versus the signal efficiency for the two sets of selections. Higher the area of the curve, better the discrimination power. The area of ROC for selection 1 is 99.27 while that of selection 2 is 79.11. Selection 1, loose cut are,

- number of muons,$(nMuon) <= 3$,
- number of tracks, $(ntrks) <= 3$,
- number of photons,$(nGamma) <= 1$,
- di-muon invariant mass, $(RMass12)$, lies between 80 GeV and 100 GeV,
- total transverse momentum of the di-muon, $(TotalPt)$ is between 30 GeV and 75 GeV.

Selection 2, tight cut are all the selection from cut-based analysis.

- Number of muons,$(nMuon) <= 3$,

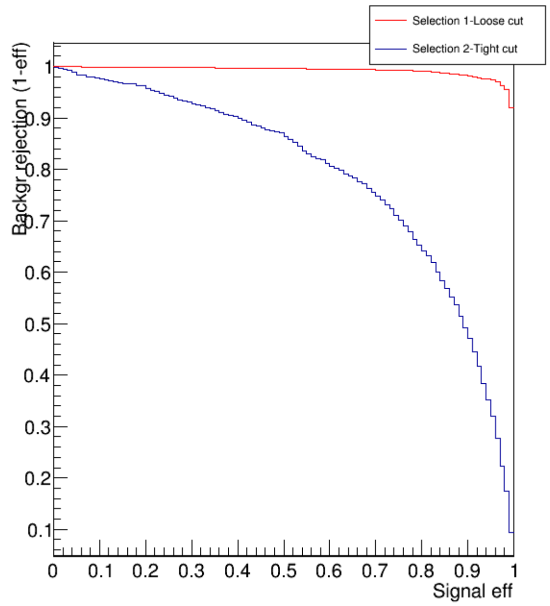

Figure 7.2. Figure showing the background rejection versus the signal efficiency for the two sets of selections.

- number of tracks, $(ntrks) <= 3$,
- number of photons,$(nGamma) <= 1$,
- di-muon invariant mass, $(RMass12)$, lies between 85 GeV and 95 GeV,
- total transverse momentum of the di-muon, $(TotalPt)$ is between 40 GeV and 65 GeV,
- cosine di-muon polar angle, $(Costheta)$ is between (-0.8, +0.8) and
- visible energy, $(VisEn)$ is between 100 GeV and 120 GeV.

7.6.2 TRAINING AND TESTING OF BDT

The BDT was trained with five discriminating variables. The variable distributions are shown in the Figure 7.3.

The Figure 7.4 shows the BDTG response for the training sample. The background events have smaller BDTG value. The selection efficiencies and the optimal cut value are

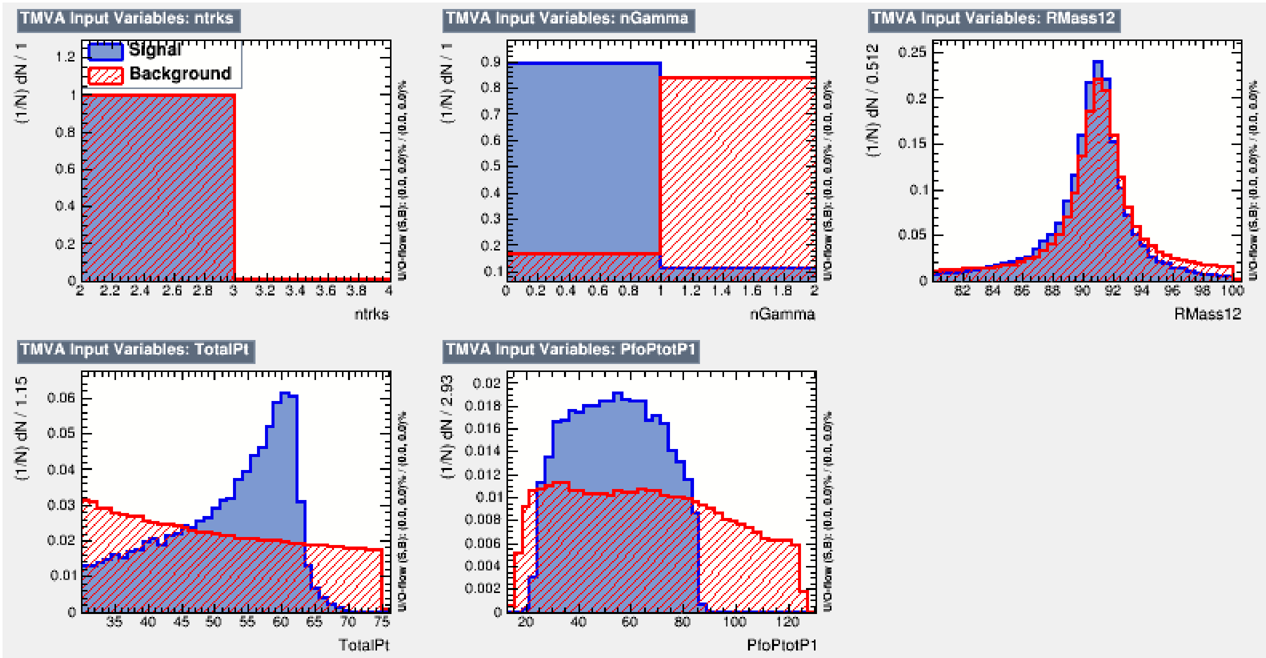

Figure 7.3. Variable distributions after preselection.

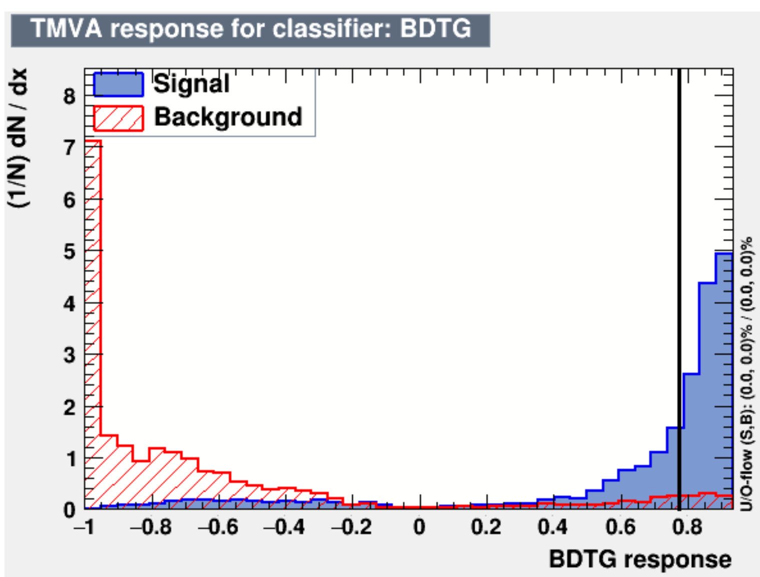

Figure 7.4. BDTG response of signal and background.

shown in the Figure 7.5. The BDTG cut value greater than 0.7815 is required which is obtained from the significance curve shown in the Figure 7.5. For 0%, 0.1%, 1%, 5% and 10% Higgs to invisible branching ratios, the BDTG cut value is stable and does not change. The logarithm of significance versus BDTG cut graphs for the 0.1% and 100% are shown in the Figures 7.6 and 7.7.

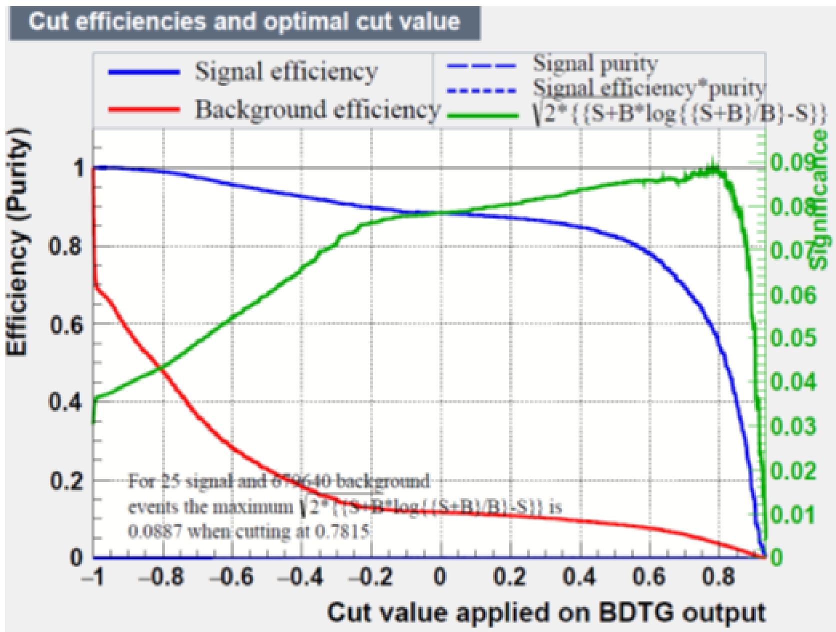

Figure 7.5. Selection efficiencies and optimal cut value for the BDT.

7.6.3 APPLICATION OF BDT RESPONSE

After aquiring the trained classifier from the training and testing phase it is applied to an unknown data sample for classification as signal and background. A signal and background sample thus obtained is further used for analysis. A fit is performed on the recoil mass spectrum. It is noted that the background shape changes after the BDT cut as shown in the Figure 7.8. For the signal, a Piece-Wise function that match the histogram of the Higgs signal in Z recoil mass distribution, referred to as HistPdf is used and the background is modelled by a Chebyshev polynomial. From the fit the number of signal and background

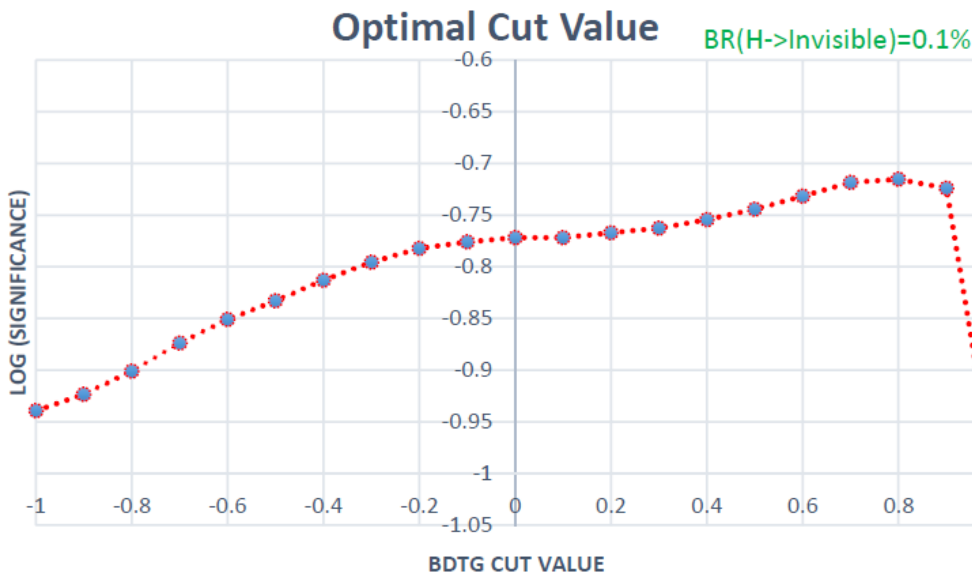

Figure 7.6. Optimal cut value for $BR(H \rightarrow Invisible)$= 0.1%.

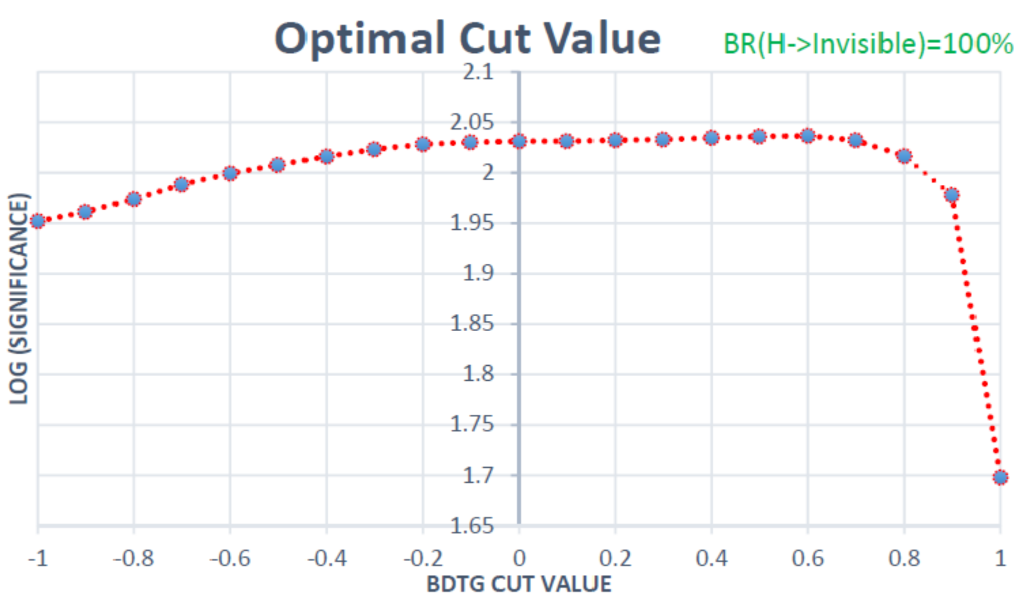

Figure 7.7. Optimal cut value for $BR(H \rightarrow Invisible)$= 100%.

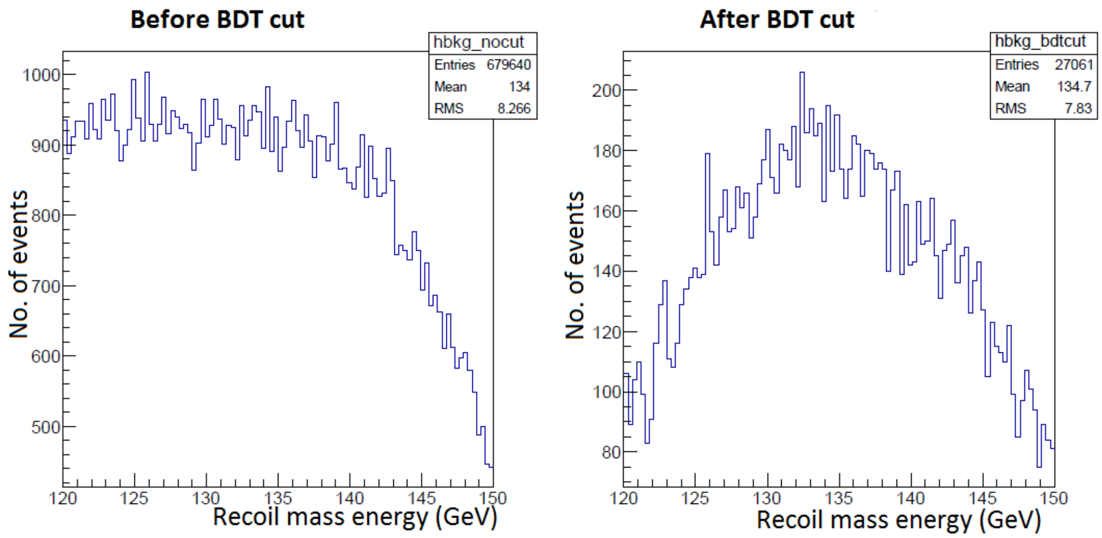

Figure 7.8. Background shape before and after BDT cut.

events are obtained. Figures 7.9, 7.10, 7.11 show the fit results. The Table 7.1 shows the number of signal and background event with and without the fit. The BR and its uncertainty are obtained using the formula given by,

$$BR = \frac{N_{fit}}{N_{ZH} \times BR(Z \to \mu^+\mu^-) \times \varepsilon_{sig}}, \tag{7.4}$$

where N_{fit} is the number of signal events obtained from the fit, N_{ZH} is the total number of ZH events obtained with the integrated luminosity of 5 ab^{-1} and is equal to 10^6. $BR(Z \to \mu^+\mu^-)$ the Z to dimuon branching ratio is $(3.4 \pm 0.007)\%$, ε_{sig} is the signal efficiency $(44 \pm 0.22)\%$. The fraction of background surviving the selection is $(0.05 \pm 0.0004)\%$.

$$\delta_{BR} = \frac{\Delta N_{fit}}{N_{ZH} \times BR(Z \to \mu^+\mu^-) \times \varepsilon_{sig}}, \tag{7.5}$$

where ΔN_{fit} is the error on the number of signal events obtained from the fit.

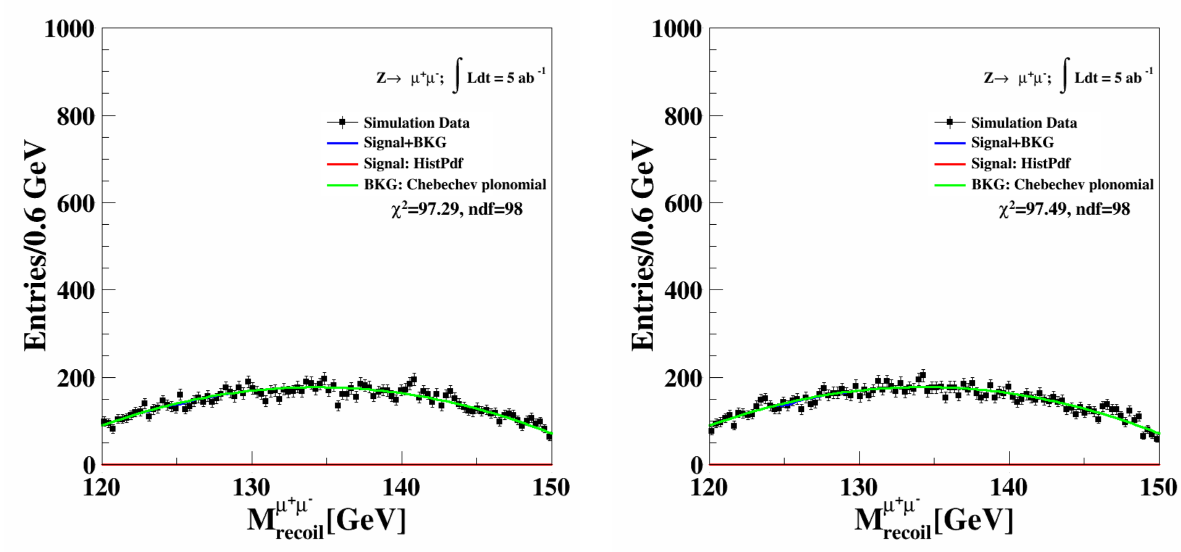

(a) BR($H \rightarrow$ invisible)=0%.

(b) BR($H \rightarrow$ invisible)=0.1%.

Figure 7.9. Fit result for BR($H \rightarrow$ invisible)=0% and 0.1%.

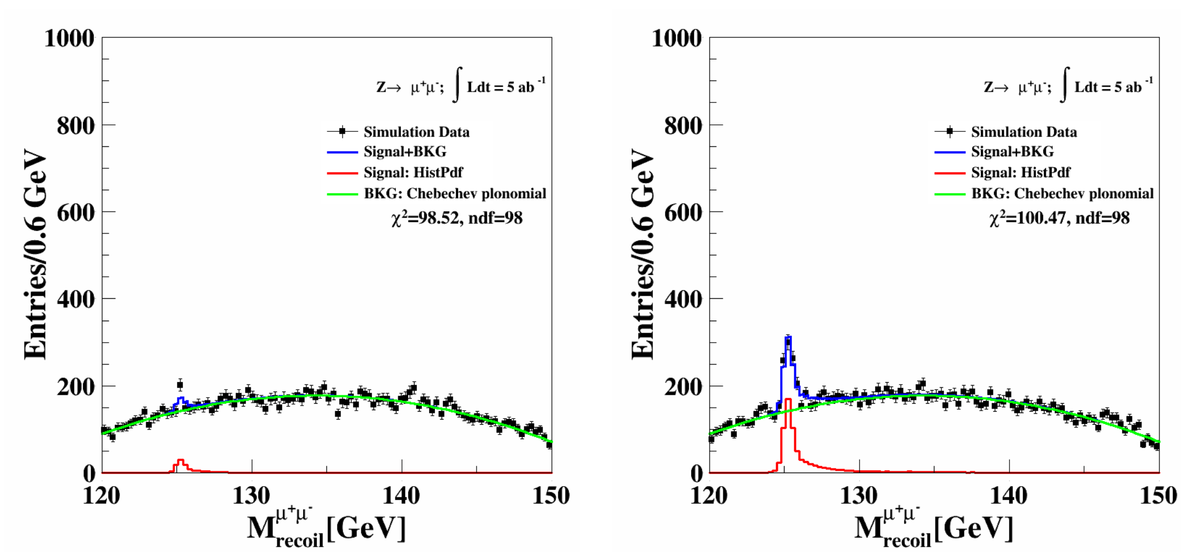

(a) BR($H \rightarrow$ invisible)=1%.

(b) BR($H \rightarrow$ invisible)=5%.

Figure 7.10. Fit result for BR($H \rightarrow$ invisible)=1% and 5%.

Table 7.1. Uncertainty on the branching ratio for $BR(H \rightarrow Invisible)$=0%, 0.1%, 1%, 5%, 10%.

Input BR (%)	Nsig (without fit)	Nbkg (without fit)	Nsig (with fit)	Nbkg (with fit)	$BR(H \rightarrow$Inv.) $\pm\delta_{BR}(\%)$
0	0	14486	0^{+38}_{-0}	14500 ± 126	$0.00^{+0.25}_{-0.0}$
0.1	15	14486	15^{+30}_{-15}	14498 ± 126	$0.09^{+0.25}_{-0.09}$
1	147	14486	129 ± 40	14506 ± 127	0.86 ± 0.27
5	734	14486	715 ± 51	14506 ± 128	4.75 ± 0.34
10	1467	14486	1447 ± 62	14508 ± 130	9.61 ± 0.41

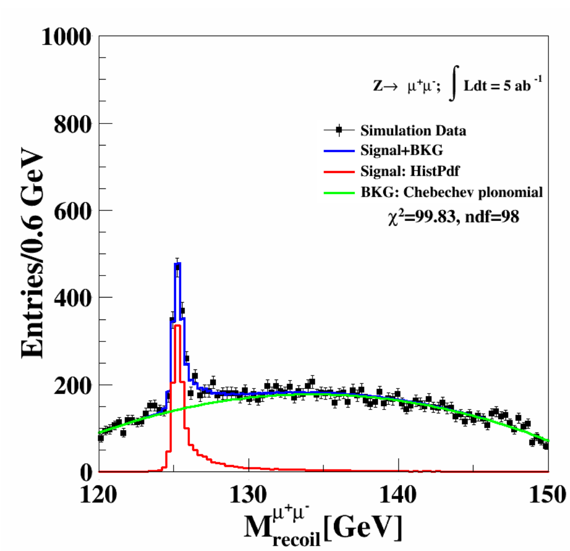

(a) BR($H \rightarrow$ invisible)=10%.

Figure 7.11. Fit result for BR($H \rightarrow$ invisible)=10%.

CHAPTER 8

RESULTS

8.1 RESULTS

The efficiency for the Higgs to invisible decay selection has been determined using the cut based analysis. The final selection has an efficiency of $(56 \pm 0.22)\%$. The fraction of background surviving the selections is $(0.01 \pm 0.0002)\%$.

Using the TMVA approach, the final selection has signal efficiency of $(44 \pm 0.22)\%$, the fraction of background surviving the selections is $(0.05 \pm 0.0004)\%$.

We determine the branching ratios corresponding to input sample values of 0%, 0.1%, 1%, 5% and 10%.

Systematic error due to the uncertainty on the $BR(Z \rightarrow \mu^+\mu^-)$ and the signal efficiency obtained from TMVA is calculated. For the input sample values of 0%, 0.1%, 1%, 5% and 10% the $(BR \pm \delta_{BR}(stat.) \pm \delta_{BR}(sys.))$ are, $(0.000 \pm 0.250 \pm 0.0000)\%$, $(0.090 \pm 0.250 \pm 0.0005)\%$, $(0.860 \pm 0.270 \pm 0.0043)\%$, $(4.75 \pm 0.340 \pm 0.0238)\%$ and $(9.61 \pm 0.410 \pm 0.0482)\%$, respectively.

The upper limit on the branching ratio is 0.55% for 0.1% BR (SM case), at a confidence level of 95%.

The two methods of data analysis presented in this dissertation, the cut-based and the TMVA approaches, result in comparable precisions, and are recommended to be the dual baselines for further study of the Higgs boson with the CEPC. Table 8.1 shows the comparison.

The possible bias due to the fit procedure and the efficiency evaluation can be estimated using statistically independent samples of the signal and the background, and will be performed in future studies.

Table 8.1. Comparison of Cut-Based analysis and Multi-Variate analysis results.

Input BR (%)	Cut-Based $BR(H \rightarrow \text{Inv.}) \pm\delta_{BR}(\%)$	TMVA $BR(H \rightarrow \text{Inv.}) \pm\delta_{BR}(\%)$
0	$0.00^{+0.23}_{-0.00}$	$0.00^{+0.25}_{-0.00}$
0.1	$0.08^{+0.23}_{-0.08}$	$0.09^{+0.25}_{-0.09}$
1	1.00 ± 0.25	0.86 ± 0.27
5	4.62 ± 0.32	4.75 ± 0.34
10	9.26 ± 0.37	9.61 ± 0.41

CHAPTER 9

FUTURE STUDIES

9.1 FUTURE STUDIES

Study of $H \rightarrow Invisible$ can be further improved by future studies.

- Larger and fully simulated SM backgrounds will predict better background shape and errors,
- better theoretical calculation,
- detector may be optimized for measuring $H \rightarrow Invisible$ study,
- other decay channels of the Z boson such as e^+e^-, $q\bar{q}$ can be added in the study of $H \rightarrow Invisible$ to enhance the sensitivity,
- sources of systematic uncertainties will be further studied, reduced and accounted for in future analysis.

REFERENCES

[1] D. Griffiths, (2010). *Introduction to Particle Physics-David Griffiths* (2nd edition). pp. 7. Wiley-vch.

[2] A. Djouadi, (2005, March). *The Anatomy of ElectroWeak Symmetry Breaking.* http://arxiv.org/pdf/hep-ph/0503172.pdf

[3] F. Englert and R. Brout, (1964). *Broken Symmetry and the Mass of Gauge Vector Mesons.* http://journals.aps.org/prl/abstract/10.1103/PhysRevLett.13.321

[4] P. Higgs, (1964). *Broken Symmetries and the Masses of Gauge Bosons.* http://journals.aps.org/prl/abstract/10.1103/PhysRevLett.13.508

[5] G. Guralnik, C. R. Hagen and T. W. B. Kibble, (1964). *Global Conservation Laws and Massless Particles.* http://journals.aps.org/prl/abstract/10.1103/PhysRevLett.13.585

[6] Official website of the Nobel Prize. http://www.nobelprize.org/

[7] R. Boughezal, (2009). *Theoretical Status of Higgs Production at Hadron Colliders in the Standard Model.* http://arxiv.org/abs/0908.3641

[8] U. Egede, (1997). *The search for a standard model Higgs at the LHC and electron identification using transition radiation in the ATLAS tracker.* http://www.hep.lu.se/atlas/thesis/egede/thesis-node1.html

[9] Higgs working group report, (2014, Jan). http://arxiv.org/pdf/1310.8361v2.pdf

[10] G. C. Branco, P. M. Ferreira, L. Lavoura, M. N. Rebelo, Marc Sher and Joao P. Silva, (2011). *Theory and phenomenology of two-Higgs-doublet models.* http://arxiv.org/abs/1106.0034

[11] C. Csaki, (1996). *The Minimal Supersymmetric Standard Model (MSSM).* http://arxiv.org/abs/hep-ph/9606414

[12] S. Dimopoulos, S. A. Raby and F. Wilczek, (1991). *Unification of couplings.* http://frankwilczek.com/Wilczek_Easy_Pieces/172_Unification_of_Couplings.pdf

[13] CERN (European Organization for Nuclear Research), (2001). http://edu.pyhajoki.fi/.

[14] H. E. Haber and G. L. Kane, (1985). *The search for supersymmetry: Probing physics beyond the standard model.* https://deepblue.lib.umich.edu/handle/2027.42/25825

[15] ATLAS Collaboration *Search for invisible decays of a Higgs boson using vector-boson fusion in pp collisions at s=8 TeV with the ATLAS detector* https://arxiv.org/abs/1508.07869

[16] S. P. Martin (Northern Illinois U.& Fermilab), J. D. Wells (CERN), (1999). *Motivation and detectability of an invisibly decaying Higgs boson at the Fermilab Tevatron.* http://inspirehep.net/record/496244?ln=en

[17] M. J. Dugan, H. Georgi and D. B.Kaplan, (1985). *Anatomy of a Composite Higgs Model.* http://inspirehep.net/record/205792/

[18] K. Agashe, R. Contino and A. Pomarol, (2005). *The Minimal composite Higgs model.* http://arxiv.org/abs/hep-ph/0412089

[19] Lectures on Supersymmetry TUTORIALS, NIKHEF Topical Lectures Amsterdam, (2005, December 14 - 16). http://folk.uio.no/farido/exercise_3.pdf

[20] Circular Electron Positron Collider http://cepc.ihep.ac.cn/

[21] CEPC Pre-CDR http://cepc.ihep.ac.cn/preCDR/volume.html

[22] S. Aplin, (2008, November). *ILC Reconstruction: ILCSoft DESY.* http://www.desy.de/dvsem/WS0809/aplin_talk.pdf

[23] G. Weiglein, (2005, March). *The LHC and the ILC.* http://www.slac.stanford.edu/econf/C050318/talks/0011_TALK.PDF

[24] Y. Bai, P. Draper and J. Shelton, (2012). *Measuring the Invisible Higgs Width at the 7 and 8 TeV LHC.* http://arxiv.org/abs/1112.4496

[25] H. Okawa and G. C. Gomez, (2013, August 15). *Searches for HiggsInvisible Decays in ATLAS & CMS.* http://indico.cern.ch/event/266515/attachments/475728/658358/CERN_CrossTalk_ZHinv_20130815.pdf

[26] M. E. Peskin, (2013). *Comparison of LHC and ILC Capabilities for Higgs Boson Coupling Measurements.* http://arxiv.org/pdf/1207.2516.pdf

[27] C. Bini, (2013). *Data analysis in Experimental Elementary Particle Physics.* http://www.roma1.infn.it/people/bini/StatEPP.pdf

[28] ilcsoft home page, http://ilcsoft.desy.de/portal

[29] D. Schulte, (1999). *Beam-beam simulations with GUINEA-PIG.* https://cds.cern.ch/record/382453?ln=en

[30] J. Reuter, F. Bach, B. Chokoufe Nejad, W. Kilian, T. Ohl, M. Sekulla, C. Weiss, (2014). *Modern Particle Physics Event Generation with WHIZARD.* http://arxiv.org/abs/1410.4505

[31] W. Kilian, T. Ohl, and J. Reuter, (2011). *WHIZARD: Simulating Multi-Particle Processes at LHC and ILC.* https://inspirehep.net/record/759495?ln=en

[32] M. Ruan, (2015). *Physics and Status of CEPC.* http://cfhep.ihep.ac.cn/whizard2015/manqi%20ruan.pdf

[33] J. Alwall, R. Frederix, S. Frixione, V. Hirschi, F. Maltoni, O. Mattelaer, H.-S. Shao, T. Stelzer, P. Torrielli, M. Zaro, (2014, May). *The automated computation of tree-level and next-to-leading order differential cross sections, and their matching to parton shower simulations.* http://madgraph.hep.uiuc.edu/

[34] J. Alwall et al., (2011). *MadGraph 5 : Going Beyond.* https://inspirehep.net/record/912611?ln=en

[35] http://home.thep.lu.se/~torbjorn/Pythia.html

[36] T. Sjostrand, S. Mrenna, and P. Z. Skands, (2006). *PYTHIA 6.4 Physics and Manual.* http://arxiv.org/abs/hep-ph/0603175

[37] http://ilcsoft.desy.de/portal/software_packages/mokka/

[38] M. Ruan, (2014, March). *Arbor, a new approach of the Particle Flow Algorithm.* http://arxiv.org/abs/1403.4784

[39] D. Buskulic et al. [ALEPH Collaboration], (1995). *Performance of the ALEPH detector at LEP, Nucl. Instrum. Meth.* https://inspirehep.net/record/381617/

[40] CMS Collaboration,(2009) *Particle-Flow Event Reconstruction in CMS and Performance for Jets, Taus and MET* https://cds.cern.ch/record/1194487?ln=en

[41] L. Wolfgang (on behalf of the ATLAS Collaboration), (2012). *Fast Simulation for ATLAS: Atlfast-II and ISF.* http://iopscience.iop.org/article/10.1088/1742-6596/396/2/022031/pdf

[42] X. Mo, G. Li, M. Ruan, X. C. Lou, (2016). *Physics cross sections and event generation of e^+e^- annihilations at the CEPC.* http://arxiv.org/pdf/1505.01008v2.pdf

[43] Milstene et al, (2006). *Muon ID at the ILC.* http://arxiv.org/ftp/physics/papers/0609/0609018.pdf

[44] H. Li, (2009, November). *Higgs Recoil Mass and Cross-Section Analysis at ILC AND Calibration of theCALICE SiW ECAL Prototype.* https://tel.archives-ouvertes.fr/tel-00430432/document

[45] M. Eugeen and T. Dierckxsens, (2014, January). *Measurement of Triple Gauge-Boson Couplings in e^+e^- Collisions at LEP.* http://www.nikhef.nl/pub/services/biblio/theses_pdf/thesis_MET_Dierckxsens.pdf

[46] The ATLAS Collaboration (2014, Feb). *Search for invisible decays of a Higgs boson produced in association with a Z boson in ATLAS.* http://arxiv.org/abs/1402.3244

[47] The ATLAS Collaboration (2009, August). *Expected Performance of the ATLAS Experiment Detector, Trigger and Physics.* http://lanl.arxiv.org/ftp/arxiv/papers/0901/0901.0512.pdf

[48] T. Hana, Z. Liua and J. Sayrea, (2014, April). *Potential Precision on Higgs Couplings and Total Width at the ILC.* http://arxiv.org/pdf/1311.7155v3.pdf

[49] Asner et al, (2013, December). *ILC Higgs White Paper.* http://xxx.lanl.gov/pdf/1310.0763v3

[50] H. Ono and A. Miyamoto, (2012, July). *Evaluation of measurement accuracies of the Higgs boson branching fractions in the International Linear Collider.* http://arxiv.org/pdf/1207.0300.pdf

[51] X. X. Liu, X. R. Lyu and Y. S. Zhu, (2015, May). *Combined estimation for multi-measurements of branching ratio.* http://arxiv.org/ftp/arxiv/papers/1505/1505.01278.pdf

[52] A. Hoecker, P. Speckmayer, J. Stelzer, J. Therhaag, E. von Toerne, and H. Voss, (2007) *TMVA Toolkit for Multivariate Data Analysis with ROOT* http://tmva.sourceforge.net/

BIOGRAPHICAL SKETCH

Susmita Jyotishmati was born to Ranjita Prasad and Amrendra Prasad in Patna, Bihar, India in December 1977, their second and youngest daughter. She received her education from first grade to twelfth grade from St. Josephs Convent High School, Patna. She then went on to do B.Sc. (Bachelor of Science) in 1999 and M.Sc. (Master of Science) in 2002, with the major subject Physics, from Patna University. After this she taught undergraduate level physics at Patna Womens College, Patna University, for one year as an ad-hoc lecturer.

On June 11, 2004 Susmita married Himanshu Dutta and came to Dallas, Texas, USA in the following month. Mayank Dutta and Vedant Dutta are their two sons. Her learning continued and she earned another Master's degree in Physics from The University of Texas at Dallas (UTD) in 2008. In Fall 2012, Susmita enrolled as a full-time graduate student at UTD and became a qualified candidate for Ph.D..

CURRICULUM VITAE

Susmita Jyotishmati

April 15, 2017

Contact Information:

Department of Physics
The University of Texas at Dallas
800 W. Campbell Rd.
Richardson, TX 75080-3021, U.S.A.

Email: sxj051100@utdallas.edu

Educational History:

High School, St. Josephs Convent High School, Patna, India, 1994
B.Sc., Physics, Patna Science College, Patna University, India, 1999
M.Sc., Physics, Patna Science College, Patna University, India, 2003
M.S., Physics, University of Texas at Dallas, 2008
Ph.D.,Physics, University of Texas at Dallas, 2017

Simulation Study of Invisible Decay of the Higgs Boson with the Circular Electron Positron Collider
Ph.D. Dissertation
School of Natural Science and Mathematics, The University of Texas at Dallas
Advisor: Dr. XinChou Lou

The feasibility study of reconstructing a Y(4260)-like state with the ATLAS detector at the LHC
M.S. Thesis
School of Natural Science and Mathematics, The University of Texas at Dallas
Advisor: Dr. XinChou Lou

Employment History:

Teaching Assistant, The University of Texas at Dallas, September 2013 – present
Research Assistant, The University of Texas at Dallas, September 2012 – May 2013
Ad-hoc Lecturer, Patna Women's College, Patna University, March 2003 – March 2004

Professional Recognitions and Honors:

Nominated for President's Teaching Award for Teaching Assistants, University of Texas at Dallas, 2017